N° d'ordre :4772

THÈSE

PRÉSENTÉE A

L'UNIVERSITÉ BORDEAUX 1

ÉCOLE DOCTORALE DES SCIENCES CHIMIQUES

Par Qiang LIU

POUR OBTENIR LE GRADE DE

DOCTEUR

SPÉCIALITÉ : Physico-chimie de la matière condensée

Synthesis, characterization and investigation on the magnetic and electronic structure of strontium iron oxides

Directeurs de thèse : M. J.M. Bassat et M. O. Toulemonde

Soutenue le : 21 mars 2013

Après avis de :

Mme. S. HEBERT	Directeur de Recherche – CRISMAT Caen	Rapporteur
M. E. MORÁN-MIGUÉLEZ	Professeur–Universidad Complutense Madrid	Rapporteur

Devant la commission d'examen formée de :

M. J.-M. BASSAT	Directeur de Recherche – ICMCB, Bordeaux	Directeur de thèse
Mme. S. HEBERT	Directeur de Recherche – CRISMAT Caen	Rapporteur
M. M.MAGLIONE	Directeur de Recherche – ICMCB, Bordeaux	Président du Jury
M. E. MORÁN-MIGUÉLEZ	Professeur–Universidad Complutense Madrid	Rapporteur
M. E. PELLEGRIN	Scientifique – Synchrotron CELLS – ALBA	Examinateur
M. M. POUCHARD	Professeur Emérite à l'université de Bordeaux 1	
	Membre du collège de France	Examinateur
M. H. L. TJENG	Professeur –	
	MPI de Chimie-Physique des Solides, Dresden	Examinateur
M. O. TOULEMONDE	Maitre de Conférences – ICMCB, Bordeaux	Co-directeur de thèse

Université Bordeaux 1
Les Sciences et les Technologies au service de l'Homme et de l'environnement

THÈSE

PRÉSENTÉE A

L'UNIVERSITÉ BORDEAUX 1

ÉCOLE DOCTORALE DES SCIENCES CHIMIQUES

Par Qiang LIU

POUR OBTENIR LE GRADE DE

DOCTEUR

SPÉCIALITÉ : Physico-chimie de la matière condensée

Synthesis, characterization and investigation on the magnetic and electronic structure of strontium iron oxides

Directeurs de thèse : M. J.M. Bassat et M. O. Toulemonde

Soutenue le : 21 mars 2013

Après avis de :

Mme. S. HEBERT	Directeur de Recherche – CRISMAT Caen	Rapporteur
M. E. MORÁN-MIGUÉLEZ	Professeur–Universidad Complutense Madrid	Rapporteur

Devant la commission d'examen formée de :

M. J.-M. BASSAT	Directeur de Recherche – ICMCB, Bordeaux	Directeur de thèse
Mme. S. HEBERT	Directeur de Recherche – CRISMAT Caen	Rapporteur
M. M.MAGLIONE	Directeur de Recherche – ICMCB, Bordeaux	Président du Jury
M. E. MORÁN-MIGUÉLEZ	Professeur–Universidad Complutense Madrid	Rapporteur
M. E. PELLEGRIN	Scientifique – Synchrotron CELLS – ALBA	Examinateur
M. M. POUCHARD	Professeur Emérite à l'université de Bordeaux 1	
	Membre du collège de France	Examinateur
M. H. L. TJENG	Professeur –	
	MPI de Chimie-Physique des Solides, Dresden	Examinateur
M. O. TOULEMONDE	Maitre de Conférences – ICMCB, Bordeaux	Co-directeur de thèse

Université Bordeaux 1
Les Sciences et les Technologies au service de l'Homme et de l'environnement

Laboratoire : Institut de Chimie de la Matière Condensée de Bordeaux

Adresse : 87, Avenue du Docteur Albert Schweitzer, 33608 Pessac Cedex

Site internet : http://www.icmcb-bordeaux.cnrs.fr

Acknowledgement

This thesis could not have been finished without the help and input of many other people.

First of all, I would like to thank Olivier Toulemonde. Thank you for giving me the opportunity to work with you in the SOPRANO network and introduce me into this PhD topic. Your open attitude towards science and collaborations between different labs impressed me. Your introduction for the magnetism set up my basic understanding of it. You always encouraged me to attend different conferences and workshops, making me benefit a lot.

Second I would like to thank Hao Tjeng. Thank you very much for immediately taking care of my work and my thesis when I just arrived in Dresden. Your provided me very rich scientific environment and the strongest support. Your extremely responsibility towards everyone in the group and extraordinary serious towards science will definitely influence my whole life. I was so lucky to attend your lectures of practical quantum mechanics during my thesis writing. It opened a door for me towards the beauty of physics !

Jean-Marc Bassat, many many thanks for helping me at the end of my thesis and preparing for my defence.

Special thanks to Alexander Komarek. Without your great help for growing the single crystal of $Sr_4Fe_4O_{11}$ and analyzing the single crystal neutron data, this PhD work can't be fruitful. It was always great pleasure to work together with you. Your hard working habit and serious attitude towards science made every piece of our work efficient and valuable!

Zhiwei Hu, big thanks to you! Your great responsibility, your hard working, your explanation for all the spectra that had been taken for the whole thesis made this PhD work completed ! It was always inspiring for me to discuss with you and you really taught me a lot about the physics and XAS during my PhD !

I would also like to specially thank Peter Adler. I was so lucky to meet you at the end of my PhD. Your great knowledge about the Mössbauer spectroscopy and your profound understanding on the strontium iron oxides intensively helped me to clarify my understanding of this system. Your great patient and dedication to my thesis make the Mössbauer and magnetization part scientifically rigorous.

Nils Hollmann, many many thanks to you for all the time explaining me about the spectroscopy, the calculation and many other questions , especially your dedicated help during my thesis writing ! Without your calculation, the $Sr_2Fe_2O_5$ part can't be completed. Your extremely patience and all the time providing help during the lectures of practical quantum mechanics greatly enhanced my understanding. You are not only a great colleague but also a good friend !

Alain Wattiaux, thanks a lot for taking all the Mössbauer spectra for this whole thesis and giving beautiful fitting and explanation for all the spectra !

Intitulé : "Synthesis, characterization and investigation on the magnetic and electronic structure of strontium iron oxides"

Soutenue à l'Université de Bordeaux I : le 21 mars 2013

Laboratoire : Institut de Chimie de la Matière Condensée de Bordeaux

La structure ABO_3 dite « perovskite » est une structure cristalline modèle puisqu'elle est adoptée par un très grand nombre de compositions chimiques. Les cations A appartiennent à la famille des terres rares, des alcalins, des alcalino-terreux et/ou des métaux des colonnes 13, 14 et 15, et les cations B sont des métaux de transitions des séries 3d, 4d et/ou 5d. Cette structure ouvre ainsi un très vaste champ d'investigations pour les chimistes du solide dont le cœur de métier concerne l'établissement de relations structures-propriétés physiques.

Parmi les phases très étudiées dérivant de la structure perovskite, les oxydes de fer et de strontium sont des phases cristallines dites modèles puisqu'elles présentent des sur-structures cristallines associées à une mise en ordre des lacunes d'oxygènes. Les structures cristallines et les propriétés physiques des phases $SrFeO_{3-x}$ ont ainsi été largement étudiées et débattues au cours de ces dernières années mais la problématique des corrélations entre l'ordre des spins, celui des lacunes d'oxygène et un phénomène d'ordre de charges entre les cations Fe^{3+} et Fe^{4+} est toujours d'actualité dans la thématique des oxydes « fortement corrélés ».

Le travail de thèse porte donc d'abord sur la maitrise de la synthèse des phases $Sr_nFe_nO_{3n-1}$ (n = 2 et n=4), $Sr_{n+1}Fe_nO_{3n}$ (n=3) et $SrFeO_2$. Les caractérisations réalisées ont été multiples et les buts ont été (i) de confirmer l'obtention de poudres et de cristaux dont on

connaisse parfaitement la stœchiométrie en oxygène (en s'appuyant sur la spectroscopie Mössbauer, la titration redox (méthode du Sel de Mohr), la diffraction des rayons X de laboratoire), (ii) de caractériser la structure cristalline (diffractions de neutrons et de rayons X synchrotron en température), (iii) de caractériser les propriétés physiques (mesures de susceptibilité magnétique, de transport, du coefficient thermoélectrique, spectroscopie de Muon) et (iv) de caractériser les structures électroniques (Spectroscopie d'absorption de rayons X et photoémission de rayons X).

Le manuscrit de thèse est découpé en neuf chapitres, soit une introduction générale (Chapitre 1), une présentation des techniques expérimentales (Chapitre 2), une étude de la phase $Sr_3Fe_2O_6$ (Chapitre 3), de la phase $Sr_2Fe_2O_5$ (Chapitre 4), de la phase $Sr_4Fe_4O_{11}$ (Partie synthèse et structure cristalline et magnétique = Chapitre 5 / Partie propriétés physiques = Chapitre 6 / Partie structure électronique = chapitre 7) et de la phase $SrFeO_2$ (Chapitre 8) avant la conclusion (Chapitre 9).

Les résultats obtenus sur la phase $Sr_3Fe_2O_6$ sont rassemblés au chapitre 3. La première partie démontre l'intérêt d'utiliser une voie de synthèse par précipitation par comparaison avec une synthèse en voie solide. Les structures cristallines et magnétiques ont été résolues pour la première fois sur une phase cristallographique pure à l'aide de diffraction de neutrons. Les moments magnétiques sont alignés antiparallèlement dans les plans (ab) avec un moment magnétique de $3.5\mu_B$ à 10K. Les mesures de spectroscopie d'absorption de rayons X (aux seuils $L_{2,3}$ du fer appuyées par des calculs multiplets au seuil K de l'oxygène) et de spectroscopie Mössbauer démontrent un environnement de type pyramide à base carrée pour le Fe^{3+} et que le transfert de charge Fe(3d)-O(2p) est positif.

Les résultats obtenus sur un cristal de $Sr_2Fe_2O_5$ sont présentés au chapitre 4. Les spectres de spectroscopie d'absorption de rayons X au seuils $L_{2,3}$ du fer s'affinent sans ambiguïté avec un signal composé de la somme pondérée du signal des cations Fe^{3+} en site octaédrique et du signal des cations Fe^{3+} en site tétraédrique en accord avec les mesures de spectroscopie Mössbauer et les mesures de diffraction de rayons X.

Les chapitres 5, 6 et 7 sont consacrés à l'étude de la phase $Sr_4Fe_4O_{11}$. La première partie (chapitre 5) explicite la stratégie de synthèse pour obtenir des phases cristalline pures et présente une étude de la structure cristalline par diffraction de neutrons et de rayons X synchrotron. Une analyse détaillée des distances Fe-O conclue sur un phénomène d'ordre des charges concernant les cations Fe^{3+} localisés dans les octaèdres et les cations Fe^{4+} dans les pyramides à base carrée. Malgré la grande pureté cristalline des phases, l'étude de diffraction magnétique de neutrons ne permet pas de différencier entre les deux structures magnétiques proposées. Finalement, une expansion thermique « négative » des paramètres de mailles a été mise en évidence, dont les raisons restent à ce jour à élucider. Ce phénomène pourrait être lié (i) à une transition structurale mais dont les pics de sur-structures ne sont pas encore clairement définis, (ii) à un phénomène magnéto-élastique en relation avec l'anomalie magnétique observée au voisinage de 90K lors de la dépendance en température des spectres de relaxation de muon.

Dans le chapitre 5, il a été démontré que la pureté cristalline de la phase induit des modifications drastiques des propriétés physiques par rapport à celles déjà publiées, mais ces dernières concernaient des matériaux contenant une phase secondaire ($Sr_8Fe_8O_{23}$). Nous avons ainsi pu mettre en évidence un fort pouvoir thermoélectrique à température ambiante et une anomalie magnétique au voisinage de 90K, phénomènes qui sont

interprétés comme un ralentissement des fluctuations de spins lors de l'étude de la dynamique de relaxation de muons.

Dans le chapitre 6, l'étude de la structure électronique de la phase $Sr_4Fe_4O_{11}$ est proposée. Par comparaison avec des phases modèles ($Sr_3Fe_2O_6$ contenant 100% Fe^{3+} en site pyramide à base carrée / $LaFeO_3$ contenant 100% de Fe^{3+} en site octaédrique / $SrFeO_3$ contenant 100% de Fe^{4+} en site octaédrique), les spectres d'absorption de rayons X aux seuils $L_{2,3}$ du fer et K de l'oxygène confirment la stœchiométrie en oxygène. Les mesures de photoémission résonnante permettent de déterminer les contributions des cations Fe^{3+} et Fe^{4+} à la bande de valence de la phase, cependant la question d'un ordre de charge des cations reste en suspend dans l'attente de mesures complémentaires de dichroïsme linéaire aux seuils $L_{2,3}$ du fer.

Exposée au chapitre 8, la réduction d'une pérovskite $SrFeO_{3-\delta}$ à l'aide d'hydrure de calcium stabilise une phase riche en Fe^{2+} situé au centre d'un environnement carré. Les mesures de diffractions de rayons X ont confirmé la qualité cristalline de la phase, par ailleurs une étude de spectroscopie Mössbauer en température a mis en évidence une phase magnétique dès la température ambiante. Le but de cette synthèse était de caractériser le cation Fe^{2+} par spectroscopie d'absorption de rayons X. La combinaison de mesures de spectres d'absorption aux seuils $L_{2,3}$ du fer et K de l'oxygène démontre que tous les résultats jusque là publiés sont significatifs d'une très forte quantité de Fe^{3+} en surface. Un signal caractéristique du cation Fe^{2+} n'est observé qu'après une réduction des joints de grains à l'origine de l'oxydation et par la suppression du processus de nettoyage pour éliminer l'oxyde de calcium mélangé à $SrFeO_2$ en fin de synthèse.

Contents

Chapter 1.

Introduction

Transition metal (TM) oxides often exhibit various interesting physical properties because of the complex interplay between chemical composition (in link with the possible oxygen non-stoichiometry), crystal structure, electronic structure, magnetism, and electrical transport properties. Strontium iron oxides belonging to the Ruddlesden-Popper series $Sr_{n+1}Fe_nO_{3n+1}$,(n=1,2,3...∞) have been the subject of intensive basic research[1–7].

For example, the perovskite $SrFeO_{3-x}$ ($Sr_{n+1}Fe_nO_{3n+1}$,n=∞) is a typical model to study the effects of oxygen-vacancy ordering, exhibiting an insulator to metal transition as the oxygen content changes from 2.5 to 3. Giant magnetoresistance effects in the full oxidized and oxygen deficient samples of strontium iron oxides are associated with the ordering of spin and charge degrees of freedom [1, 2], a subject which is of great interest in contemporary solid state sciences[8]. $SrFeO_3$ having Fe^{4+} ($3d^4$) in high spin state($t_{2g}^3 e_g^1$) has the same electronic configuration as Mn^{3+} in $LaMnO_3$, but exhibits profoundly different physical properties. $LaMnO_3$ is a Mott insulator and shows a cooperative Jahn-Teller effect, while $SrFeO_3$ remains metallic and adopts a cubic structure without Jahn-Teller effect at all temperatures. The strong covalency of the Fe-O bonding, which results in a negative charge transfer energy in $SrFeO_3$, is mainly responsible for this huge difference . The negative charge transfer energy occurs when the oxygen $2p$ energy levels lie high enough so that the top part of the oxygen $2p$ band can overlap with the bottom part of the upper transition metal $3d$ Hubbard band. Thus the holes in TM $3d$ orbitals can move to oxygen $2p$ orbitals and the real electronic configuration would have oxygen holes, e.g. in $SrFeO_3$ the ground state is dominated by $3d^5\underline{L}$ ($\underline{L}$ indicate an O 2p hole)[5]. Another example for the relationship between the crystal structure and the electronic structure is the charge disproportionation. It occurs in $CaFeO_3$ where Fe^{4+} formally reacts to Fe^{3+} and Fe^{5+}, but does not happen in $SrFeO_3$. The Fe-O-Fe bond angle in the orthorhombically distorted crystal structure of $CaFeO_3$ [9, 10] which is around 158° and thus far away from 180° is the original reason for the charge disproportionation.

In the more oxygen deficient materials with decreased iron oxidation states, the covalency of bonding is smaller than for Fe^{4+} and the importance of electron correlation becomes more prominent. It therefore gives more interesting behaviors of spin, charge and orbital interactions. For instance, $Sr_8Fe_8O_{23}$ ($SrFeO_{2.875}$) has a Verwey-like transition around 70K, where a combined charge-magnetic ordering phenomenon was observed together with a metal-insulator transition[2]. However, in the more oxygen deficient sample $Sr_4Fe_4O_{11}$ ($SrFeO_{2.75}$) , the Verwey-like transition is absent below room temperature. At room temperature the crystal structure of $Sr_4Fe_4O_{11}$ reveals ordering with chains of octahedral sites cross linked by dimers of pyramidal sites . This corresponds to charge ordering with equal amount of Fe^{4+} and Fe^{3+} as confirmed by the Mössbauer analysis. The vacancy and charge orderings explain the absence of the Verwey-like

transition in $Sr_4Fe_4O_{11}$ below room temperature . Furthermore, unlike in $Sr_8Fe_8O_{23}$ where Fe^{4+} and Fe^{3+} are magnetically ordered below Verwey-like transition, in $Sr_4Fe_4O_{11}$ only one site is magnetically ordered below the Néel transition temperature (T_N=232K). From the Mössbauer data it is believed to be Fe^{3+} . Conversely, the Fe^{4+} remains magnetically disordered in $Sr_4Fe_4O_{11}$ down to 4K in contrast to it in $SrFeO_{2.86}$, where Fe^{4+} is antiferromagnetically ordered. Moreover, the spin state of Fe^{4+} in $Sr_4Fe_4O_{11}$ is still an open question. Based on the value of the isomer shift in the Mössbauer spectrum alone, the question cannot be solved [11, 12] . Recently, a debate arising from the charge and spin ordering in $Sr_4Fe_4O_{11}$ has attracted great attention [13–18]. Therefore, the properties of $Sr_4Fe_4O_{11}$ are poorly understood yet, and studying in details this compound is one of the main focuses of this work.

A further extension to the work on the $SrFeO_{3-x}$ series, has been added recently [4] by the synthesis of $SrFeO_2$ which can be formally derived from the ideal perovskite $SrFeO_3$ by removing one oxygen atom. This results in an Fe^{2+} compound with a square planar oxygen environment. The energy difference between the oxygen $2p$ band and iron $3d$ band is supposed to be increasing with the lower valence of iron cations. But the Fe-O hybridization in $SrFeO_2$ is still strong enough [6, 7, 19] to keep Fe^{2+} stable in square planar coordination up to 900K[6]. The strong hybridization leads to superexchange interactions through the in-plane Fe-O-Fe and direct exchange interactions between the out-of-plane Fe-Fe [20]. The $t_{2g}^4 e_g^2$ electron configuration of Fe^{2+} is particular interesting as orbital ordering effects may be expected for this case.

Apparently, it is possible to change progressively the oxidation state of iron from +2 to +4 within the series $SrFeO_{3-x}$. It thus forms one of the basic themes of this PhD work.

Extending the research towards the other terms of the RP series, many efforts have been devoted to understand the spin, charge and orbital interactions of Fe^{4+} in $Sr_{n+1}Fe_nO_{3n+1}$(n=1,2,3), where the iron-oxygen bond lengths are nearly independent of the number n of iron-oxygen layers so that the bandwidth of the σ^* conduction band is directly related to the number of nearest-neighbor metal ions[3]. As the electronic ground state of Fe^{4+} oxides is at the insulator-metal borderline [3] where the effective electron correlation energy U is of similar size as the width ω_σ of the σ^* conduction band (anti-bonding) , the full oxidized stoichiometric $Sr_{n+1}Fe_nO_{3n+1}$(n=1,2,3) with the bandwidth ω_σ, are mainly controlled by the degree of condensation of the Fe-O network[3]. Therefore, the strontium iron oxides are considered as good examples for the characterization of the insulator-metal borderline region in a strongly correlated electronic system. However, the electronic properties of the oxygen-deficient materials in the Ruddlesden-Popper series with high Fe^{3+} fractions are poorly understood yet. As the free Fe^{3+} high spin state is electronically stable with no orbital angular momentum, the electronic structure change of these compounds are more directly related to the symmetry and the structure. This leads to the insulating Fe^{3+} oxides $Sr_3Fe_2O_6$ and $Sr_2Fe_2O_5$, which are very well-known compounds. $Sr_3Fe_2O_6$ has Fe^{3+} sitting in pure pyramidal sites and $SrFeO_{2.5}$ has Fe^{3+} sitting in octahedral and tetrahedral sites. There are few detailed experimental reports for the electronic and magnetic structures of $Sr_3Fe_2O_6$ and confusing reports of X-ray absorption spectra on $SrFeO_{2.5}$ [21–23]. It is important to clarify their electronic structures as they are important basic systems for understanding the higher and lower oxidation state compounds, for a chemical and physical point of view.

As a general trend, an important feature of the oxygen deficient material $SrFeO_{3-x}$ is the coexistence of different oxygen vacancy ordered phases in samples with x≠0 . This has hindered

4

the quantitative description of spin and charge ordering in oxygen deficient samples[24]. One purpose of this thesis is to prepare pure phases with a well-defined distribution of oxygen vacancies close to two of the four identified phases ($SrFeO_{2.75}$, $SrFeO_{2.5}$). For this purpose, single crystals and powder samples were prepared and characterized by various physical techniques.

The chapters are organized as follows:

Chapter 2, introduces the experimental techniques that have been used in this thesis. Starting with the description of the principle of diffraction as the important characterization of the crystallographic and magnetic structure of the samples, the principles of Mössbauer spectroscopy, X-ray absorption spectroscopy and photo emission spectroscopy are introduced. Then the principle of muon spin rotation (or relaxation/resonance) specialized on the magnetic properties is elaborated.

Chapters 3 and 4 are focused on the most well-known $Sr_3Fe_2O_6$ and $Sr_2Fe_2O_5$ compositions. Detailed descriptions of the preparation of a high quality powder sample $Sr_3Fe_2O_6$ and of a twinned single crystal $Sr_2Fe_2O_5$ are presented. The characterization has been performed by X-ray diffraction and Mössbauer analysis. Neutron powder diffraction results focusing on the nuclear and magnetic structure of $Sr_3Fe_2O_6$ are discussed. Electronic structure investigations based on experimental results from X-ray absorption together with cluster calculations are shown for both system.

Afterwards, the mixed valence (Fe^{3+} , Fe^{4+}) compound $Sr_4Fe_4O_{11}$ is largely studied in Chapters 5, 6 and 7. The preparation of high quality powder and single crystal samples is detailed in Chapter 5. Special efforts have been dedicated to the control of the oxygen stoichiometry of the compound. Neutron powder diffraction and single crystal diffraction are employed for the nuclear structure and magnetic structure determination. The structure change versus temperature has been studied with high resolution synchrontron measurements.

The magnetic and transport properties are elaborated in Chapter 6. Seebeck coefficient, magnetization, resistivity and Mössbauer measurements have been used for two different batches of samples with tiny differences in oxygen stoichiometry, and the results are discussed. Special attention has been paid to the study of the magnetic transitions versus temperature with the help of μSR and Mössbauer spectra.

The electronic structure has been explored with X-ray absorption spectra on Fe^{3+} and Fe^{4+} in different oxygen coordinations(Chapter 7). The resonant photoemission spectrum is used as a tool for specifying the contributions of Fe^{4+} and Fe^{3+} to the valence band.

The last but not least chapter is focused on $SrFeO_2$, which has been discovered recently with high spin Fe^{2+} stabilized in square planar coordination. Its interesting structure and potential interesting physical properties attract great attention but its electronic structure based on X-ray absorption spectroscopy has not been clarified yet. The main problem is arising from the low temperature preparation procedure, making it extremely difficult to prepare a well-sintered pellet. Large grain boundaries effects make the interpretation of x-ray absorption spectra not unambiguous due to the high surface sensitivity of the technique. Large efforts have been focused on solving the grain boundaries problems and the results will be described.

Chapter 2.

Experimental methods

In order to characterize the physical properties of the strontium iron oxides, different spectroscopic techniques have been used in this thesis. These spectroscopies analyze the interaction of a beam with the sample and yield intensity as a function of energy. There are four main processes of a beam (photons, microwaves, Infrared, UV, X-ray, Gamma ray, neutrons, electrons etc.) interacting with materials as sketched in Figure 2.1. A beam hits the sample, and its energy might partially loss or might stay the same depending on the interaction process. Part of the beam is transmitted through the material or maybe scattered without changing the energy e.g. X-ray diffraction, Neutron diffraction and Transmission electron microscopy. Part of the beam may loose energy by being absorbed through the material,e.g.Mössbauer spectrum, Raman, or being scattered such as inelastic neutron scattering, electron energy loss spectroscopy. Part of the absorbed beam may excite electrons or atoms inside the material and these excited states may emit light and decay into another state like in fluorescence, X-ray photoemission, μSR(muon spin rotation, relaxation or resonance) etc.

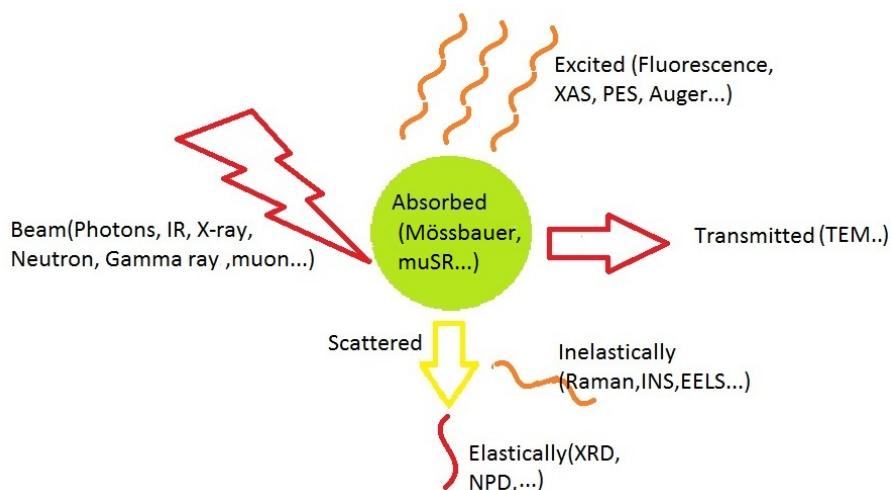Figure 2.1.: Different beam react with materials

During this thesis, we have used Mössbauer spectroscopy, μSR, X-ray absorption, photoelectron spectroscopy, neutron elastic scattering and powder diffraction(lab X-ray and synchrotron X-ray) in order to characterize the magnetic and electronic structures and its related physical properties. These techniques will be briefly introduced in this chapter.

2.1. Principle of Diffraction

When radiation incident upon a crystal and is scattered, the diffraction occurs if the wavelength of this radiation is similar to the atomic spacing in the crystal. The scattering of this radiation will give rise to a set of diffracted beam which contains the information of the characteristic geometry of this crystal. Consequently, the position and intensity of the diffracted beam in the diffraction pattern brings information about the arrangements of the atoms in space and some other atomic properties in the crystal. The Bragg law defines a specific condition when a beam of radiation is diffracted by sets of lattice planes and gives the position of a diffracted beam. It can be expressed as

$$2 \cdot d \cdot \sin(\theta) = n \cdot \lambda \qquad (2.1)$$

d is the interplanar spacing (the perpendicular separation) of the (hkl) planes (hkl is the Miller indices), n is an integer, 2θ is the scattering angle and λ is the wavelength of the incident beam. With vector notation, the Bragg equation displays that diffraction occurs when the magnitude of the scattering vector is an integral number of reciprocal lattice vector($\overrightarrow{1/d^*}$). The scattering vector depends on the geometry of the experiment setup whereas the reciprocal lattice is determined by the orientation and the lattice parameters of the reciprocal unit cell. Ewald's construction relate the scattering vector and the reciprocal lattice in a intuitive way. It contains a sphere with radius $1/\lambda$, centering on the tail of the incident wave vector $\overrightarrow{S}_0$ and the reciprocal lattice with the origin lying at the tip of the incident wave vector $\overrightarrow{S}_0$, see Fig 2.2a

If the ends of the scattering vector $\overrightarrow{d}^*$ in the Ewald sphere are reciprocal lattice points, Bragg's law can be satisfied when the two ends of $\overrightarrow{d}^*$ coincide with the surface of the sphere, see Fig. 2.2a. For a single crystal, it is exactly the case where the possible reflections between two reciprocal lattice points fulfill the Bragg law and may possible be detected if it satisfy the experimental constraints. For a powder sample , however, is more complicated as it contains individual crystallites in all possible orientations. The orientation of the scattering vector $\overrightarrow{d}^*_{hkl}$ is lost and different reciprocal lattice points construct a set of nested spherical shells centered at the reciprocal space origin. In three dimension, these shells form coaxial cones, which are called Debye-Sherrer cones, see Fig. 2.2b. These Debye-Sherrer cones will intersect with the Ewald sphere and recorded in the detector. It is exactly the case for the Debye-Scherrer diffractometer. The positions and intensities of the diffracted beams are recorded along narrow strips to yield a characteristic pattern of diffracted lines or peaks. This is the usual powder diffraction pattern. The position of a line depends only upon the spacing of the crystal planes involved in the diffraction and the wavelength of the incident beam. The intensities are related with the modulus of the structure factor which involves the atomic scattering factor. There are also other factors influencing the intensity of the pattern, such as temperature factor, multiplicity, Lorentz factor, polarization factors, sample size and sample shape[25]. The structure can be obtained by refining the diffraction pattern. There are different refinement methods [26]. In this PhD thesis, the Le-Bail and Rietveld Refinement have been used for determining the nuclear and magnetic structure. Since these techniques require a model of atom distribution in the unit cell very close to the actual positions, initial models of all the compounds in this thesis are taken from ICSD data base. They are used as initial input to start the refinement program and the variables are modified to obtain the best fit for the experimental pattern. The refinements presented in this

thesis were carried out using the Fullprof package[27].

Generally, the neutron and X-ray diffraction are basic tools to study the nuclear and magnetic structure of the compounds. The neutron is a particle with no charge, 1/2 spin and magnetic dipole moment $\mu_n = -1.913\ \mu_N$ (μ_N is nuclear magneton). It can closely approach the atomic nucleus and be scattered by nuclear force or via spin-spin interactions with both nuclear magnetic moments and unpaired electrons in magnetic atoms or ions. The scattering process is quasi punctual. The Fourier transform of punctual object in reciprocal space is widely spread thus the neutrons are strongly scattered at high angles. And since the neutron couple also to the magnetic moment of the electrons, it gives the information about the particular nucleus and the spin state of the nucleus-neutron system in terms of the value of the scattering length. As the nuclear scattering of neutrons results from interaction with the nucleus, rather than with the electron cloud, it is easier to sense light atoms, e.g. oxygen atoms. In this PhD thesis, we have tried to use neutron scattering to investigate the nuclear and magnetic structure of different strontium iron oxides. The experiments are carried out in D20 and D2B at the ILL in Grenoble, France and in Trics at PSI in Villigen, Switzerland. In case of X-ray, the scattering process occurs between the photon and the electrons surrounding the atomic nuclei. The photon is the quantum of the electromagnetic field with no magnetic moments, no charge and one spin. It reacts with electron cloud thus weakly diffused for the high $\sin\Theta/\lambda$. For the synchrotron radiation source, it can provide high energy, high flux with high resolution X-rays which can give more detailed inter-atomic information about the structure. Hence, it is more sensitive to the tiny structure phase transition and symmetry change. In this PhD thesis, high resolution synchrotron measurement have been performed in X04SA beam line at PSI in Switzerland.
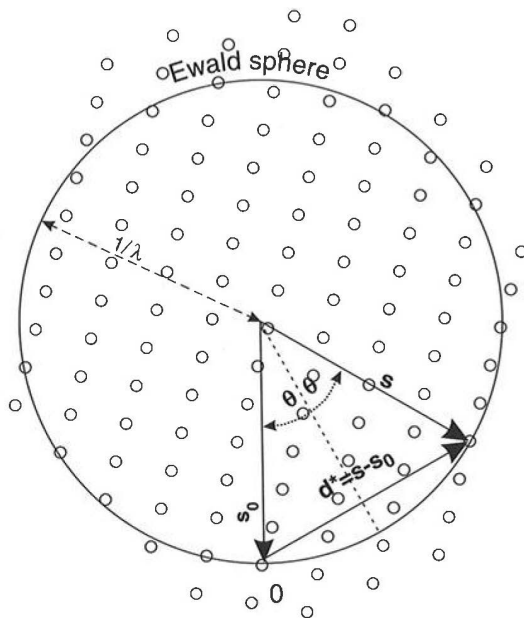
(a) The geometrical construction of the Ewald circle. $\vec{S}_0$ incident wave vector , pointing in the direction of the incident beam and $\vec{S}$ is scattered wave vector, pointing in a direction from the sample to the detector. The scattering vector $\vec{d}^*$ is from the tip of $\vec{S}$ to the tip of $\vec{S}_0$.[26]
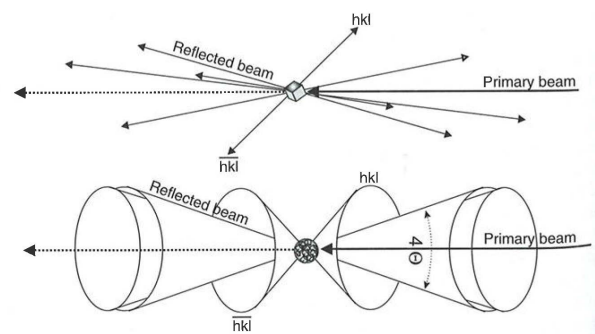
(b) Comparison between the scattered beams originating from a single crystal (top) and a powder (bottom). For the powder, some Debye-Sherrer cones are drawn.[26]

2.2. Principle of XAS

In x-ray absorption spectroscopy, light in the x-ray range (λ = 10 to 0.01nm, E=100eV to tens of keV) is used to excite strongly bound electrons in the core shell states to weakly bound states near the Fermi level. At the transition metal $L_{2,3}$ edge, one excites electrons from the $2p$ states into the d shell, which in an one-electron picture, would probe the unoccupied density of states of the ion, see Figure 2.2. However, this simple picture completely neglects the electron interaction, especially the influence of the core hole.
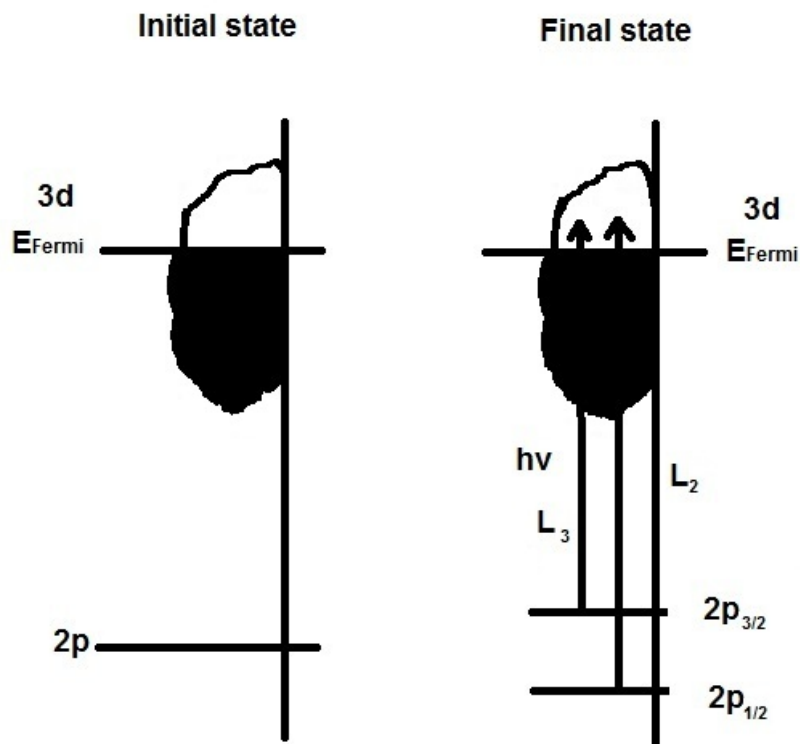
Figure 2.2.: X-ray absorption scheme for 2p to d excitations.

X-ray absorption spectra is strongly element specific, the energy position of the so-called absorption edges, where prominent features are observed, is determined by the binding energy of core electrons of special element. In this thesis we will concentrate on iron, which belongs to the $3d$ transition metals, and the excitations from the $2p$ to $3d$ shell known as $L_{2,3}$ edge, corresponding to the Fe $2p$ core hole in $2p_{1/2}$ and $2p_{3/2}$ final states respectively. In addition, we will look at the $1s$ to $2p$ excitation in oxygen, the oxygen K-edge. These excitations are dipole allowed and therefore do have good absorption cross sections[28]. These spectra give plenty of information about the valence shell.

From a theoretical point of view, the sensitivity of the charge in the x-ray absorption process

can be understood in a simplified many-body picture[29]. The electrons in the initial state absorb a photon and are excited into various final states with a core hole:

$$2p^6 3d^n + hv \longrightarrow 2p^5 3d^{n+1}$$
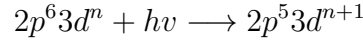
We use on-site energies E_p and E_d for $2p$ and $3d$ electrons, respectively, and a Coulomb repulsion of two electrons at d shell U_{dd}, and in addition U_{cd} as the interaction between core-hole and the valence electrons. The energy conservation in this process can be then expressed as:

$$6E_p + nE_d + \frac{1}{2}n(n-1)U_{dd} + hv \longrightarrow 5E_p + (n+1)E_d + \frac{1}{2}(n+1)nU_{dd} - (n+1)U_{cd}$$

Thus,

$$hv_n = -E_p + E_d + nU_{dd} - (n+1)U_{cd} \tag{2.2}$$

For the atoms with lower valence and $3d^{n+1}$ electrons, the absorption process can be expressed as :

$$2p^6 3d^{n+1} + hv \longrightarrow 2p^5 3d^{n+2}$$
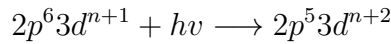
Using the same definition of on-site energies in the different shells as well as of the terms for the interactions as above, the energy conservation can be expressed as:

$$6E_p + (n+1)E_d + \frac{1}{2}(n+1)nU_{dd} + hv \longrightarrow 5E_p + (n+2)E_d + \frac{1}{2}(n+2)(n+1)U_{dd} - (n+2)U_{cd}$$

Thus,

$$hv_{n+1} = -E_p + E_d + (n+1)U_{dd} - (n+2)U_{cd} \tag{2.3}$$

Hence, the energy difference between these two different valences in the spectrum is:

$$hv_{n+1} = hv_n + U_{dd} - U_{cd} \tag{2.4}$$

Normally $U_{cd} > U_{dd}$ and $U_{cd} - U_{dd} \approx 1 \sim 2eV$, and then

$$hv_{n+1} < hv_n$$

. Thus, a lower valence of a transition metal will appear at lower absolute energy position in its $L_{2,3}$ XAS spectrum.

In addition to the valence sensitivity, x-ray absorption spectroscopy is also sensitive to the crystal field. The crystal field can be described as the derivative of the Madelung potential. The Madelung potential is the electrostatic long range Coulomb potential that one ion in the lattice feels from the other ions. By considering the symmetry of the coordination around a special ion, the parameters that determine the crystal field splitting can be reduced. Fig. 2.3 is an example of the energy level diagram for the coordination of an atom changing from O_h point group to the lower symmetries. For a free TM ion, the five d orbitals are degenerate. When the ion is situated in cubic point group symmetry, the degeneracy of the $3d$ orbitals will be lifted as the energy of the orbitals will depend on the spacial orientation of the orbital in comparison to the
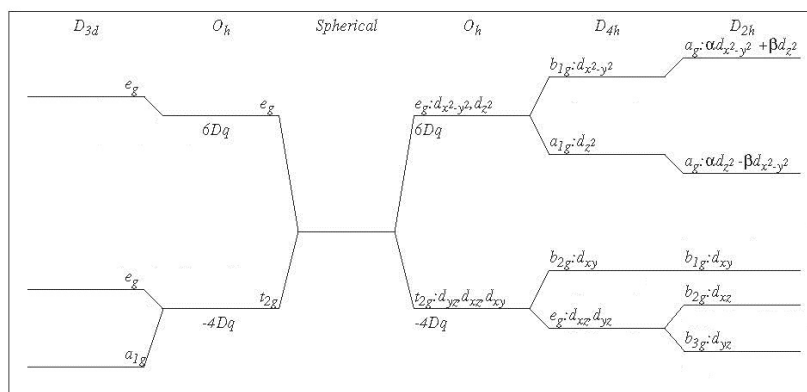
Figure 2.3.: The splitting of energy level diagram for a d shell on different symmetry from left to right: Trigonal(D_{3d}),Cubic(O_h), Tetragonal(D_{4h}) and orthorhombic (D_{2h}) symmetry [28]

bonding. Then one parameter known as $10Dq$ is used to describe the crystal field splitting within the $3d$-shell. If the symmetry goes to a lower point group, e.g. D_{4h}, D_{3d} and D_{2h}, the degeneracy of the $3d$ orbitals is further lifted as indicated in Fig. 2.3, and more parameters have to be taken into account in order to describe the crystal field splitting.

Typical Fe $L_{2,3}$ XAS spectra are shown in Figure. 2.4[30] with common typical features. Two groups of peaks which are assigned to two possible final core states with the hole spin parallel or antiparallel to its orbital angular momentum, $2p_{1/2}$ (L_2) and $2p_{3/2}$ (L_3). The energy separation between these levels scales with the 2p core hole spin-orbit splitting. From Figure 2.4, we can see the increase of the valence state of Fe by one causes a shift of the spectra at $L_{2,3}$ edge by around one eV toward higher energies due to Coulomb interaction. Thus the XAS is sensitive to the valence. The spectra also indicated the high sensitivity of the XAS to the symmetry, which are indicated in the spectral shape. Due to the complexity of the multiplet structure, the local symmetry is usually not directly accessible and one needs to simulate the spectra to understand the influence of the symmetry (see Figure 2.4).

As the absorption promotes an electron from a core level to an unoccupied state above the Fermi level, a hole is left at the core level. There are two paths for the excited atom to be relaxed, through either radiative or non-radiative decay. The radiative decay is the creation of a photon when the core hole is filled by a corresponding electron. The corresponding detection method is called fluorescent yield (FY) mode. The probing depth of this method is in the order of 1000 Å. The non-radiative decay is shown in terms of energy transfer to an Auger electron, which escapes from the sample surface, in conjunction with secondary electrons. They can be measured by the drain current that neutralize the charge loss of the secondary electron with the sample being connected to the ground. This detection method is called total electron yield (TEY) mode which has a small probing depth (40-100Å), depending on the material.

2.3. Principle of PES

Photoelectron spectroscopy (PES) is based on the photoelectric effect, where the incoming photons transfer the energy to the electrons in the material and a detector collects the emission of
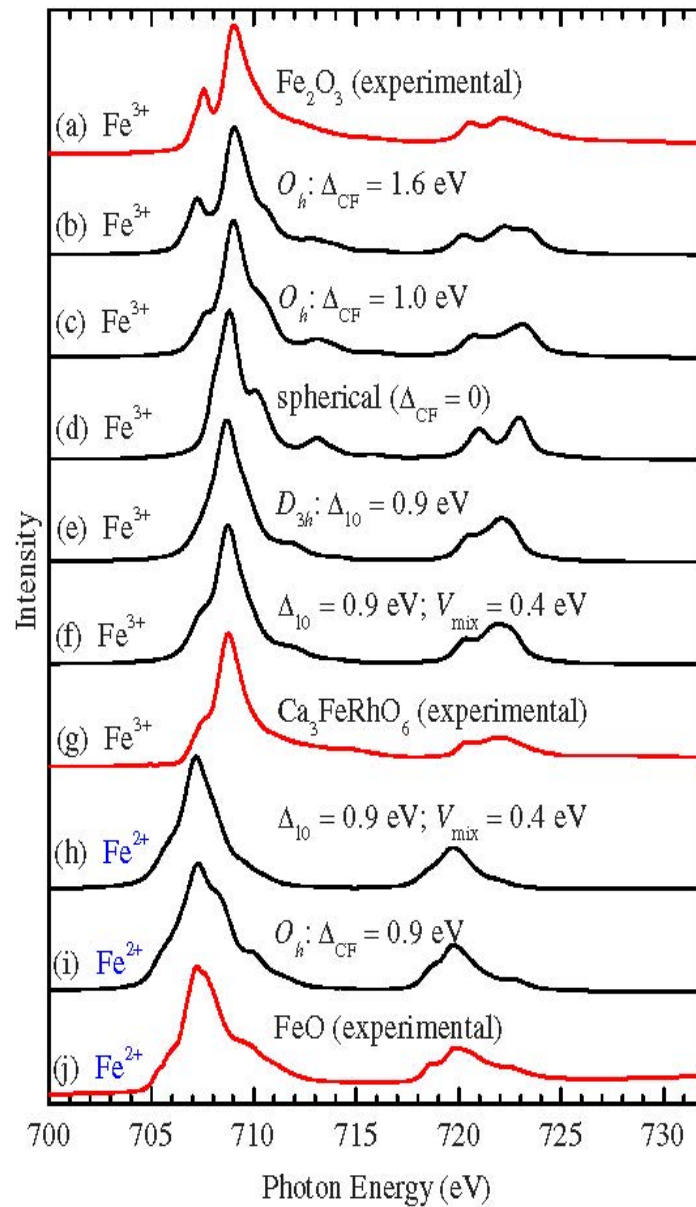
Figure 2.4.: This figure is reproduced from Ref[30]. The red lines are the experimental XAS spectra at the Fe $L_{2,3}$ edge of (a) Fe_2O_3 (Fe^{3+}), (g)Ca_3FeRhO_6, and (j)FeO(Fe^{2+})(Taken from Park[31]). Together with simulated spectra (b) and (c) in O_h, (d) spherical, and [(e) and (f)] D_{3h} symmetry for Fe^{3+} and simulated spectra in (h) D_{3h} and (i) O_h symmetry for Fe^{2+}. The simulated spectra have been broadened by a Gaussian with a HWHM of 0.2eV and Lorentzian with a HWHM of 0.3eV

the excited photoelectrons from the sample. This technique yields information on the electronic structure of solids. In one electron theory, the scheme of PES is shown in Figure 2.5. The Fermi energy E_F is at the top of the valence band and has a separation ϕ from the vacuum level E_{vac}.

The energy conservation law in the photoemission process is the basis for the photoelectron spectroscopy:

$$E_{kin} = h\nu - E_B - \phi \tag{2.5}$$
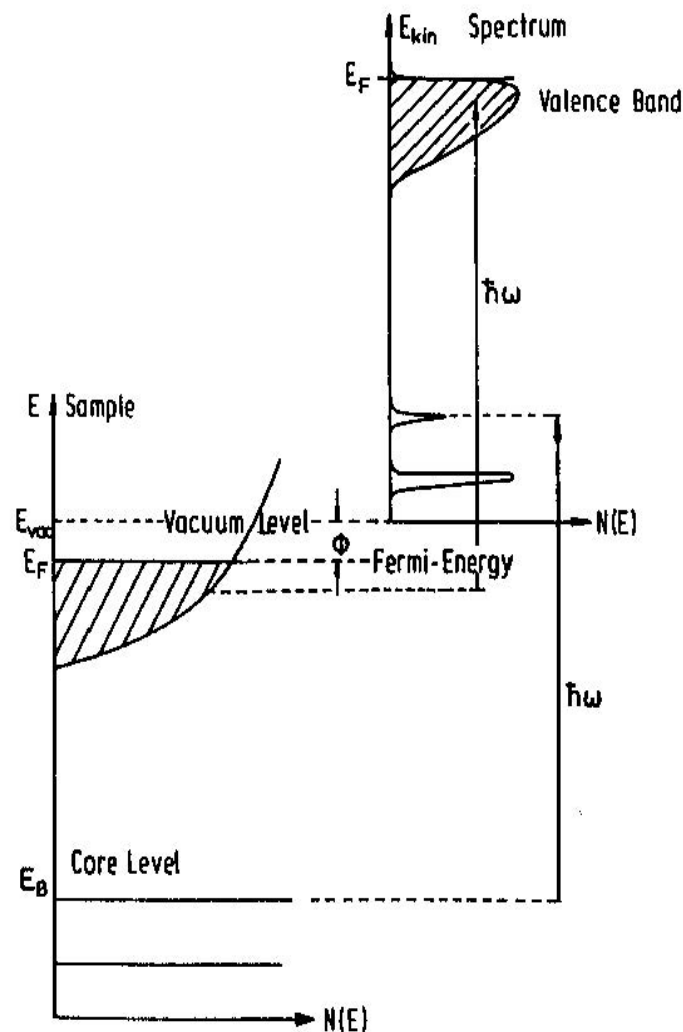
Figure 2.5.: In PES, electrons (in the core level or valence band) are excited with a constant photon energy h_ν into the vacuum. E_B is the binding energy ($E_B = 0$ at E_F). According to the kinetic energy of the photoelectron that is detected in the PES analyzer, bonding energy E_B can be calculated from equation 2.5, ϕ the work function that separate the Fermi energy E_F from the vacuum level E_{vac}[32]

with $h\nu$ being the incoming photon energy and ϕ the work function. By analyzing the kinetic energy E_{kin}, the binding energy E_B of the electron in the material can be deduced(E_B=0 at E_F). The binding energy is identified with the difference of the total energies of the excited final state and the ground state. Assuming the photoelectron escaped from the solid without interaction with the system left behind, the photoemission spectrum then is given by the number of electrons as a function of binding energy. In a one-electron approximation, the PES spectrum is comparable to the occupied density of electronic states. Especially in weakly correlated systems, density-functional theory can be used to describe the spectrum of the valence band. But the many-body character of the excitation makes the one-electron approximation in general incorrect. The independent-electron model and the DFT method are not accurate enough when applied to strongly correlated materials[33]. Strongly correlated electrons need to be treated using a

many-body framework. There are several models used to interpret some important characteristics of the electronic structure of strongly correlated oxides. One is the Hubbard model, which is developed from tight-binding model by including an energy U for any atomic site occupied by more than one electron. The competition involved in the Hubbard model is between the kinetic energy (electron hopping) to delocalize the electrons into itinerant (Bloch) states and the on-site Coulomb interaction to localize the electrons, driving systems into Mott-Hubbard insulators. The transition from a delocalized to a Mott-Hubbard insulating state is sketched in Figure 2.6. Compounds with the bandwidth larger than the Coulomb interaction tend to be metallic. When the on-site Coulomb energy is larger than the bandwidth, an insulating state can be found with band gap determined by the magnitude of the $d-d$ Coulomb repulsion (U_{dd}).
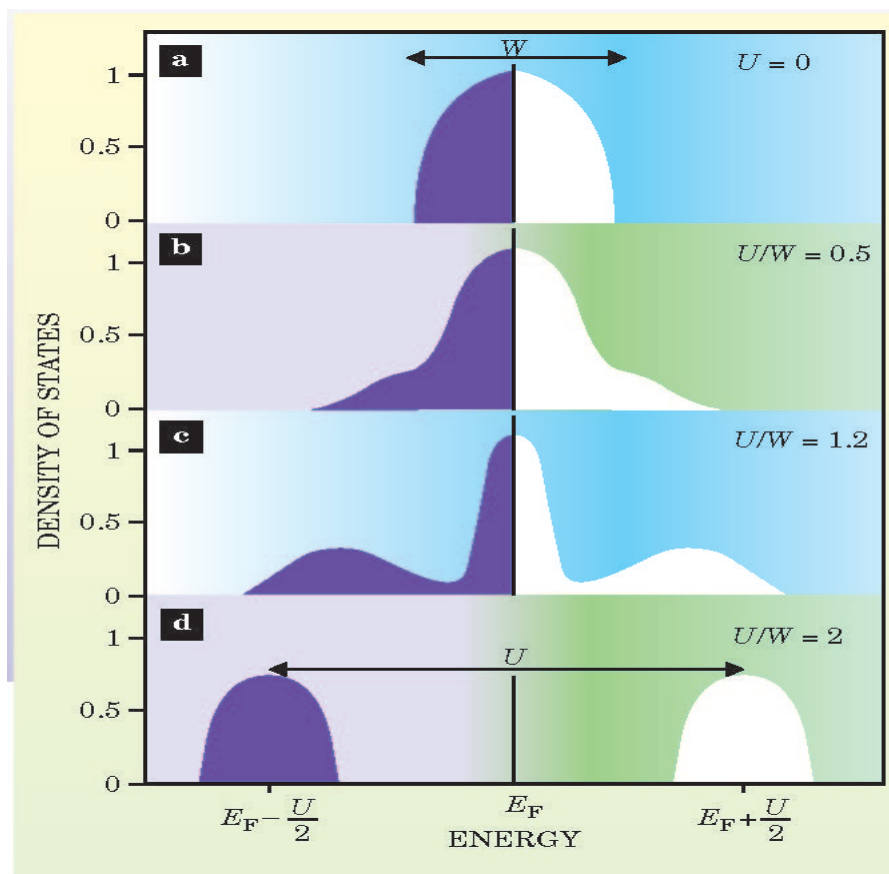
Figure 2.6.: This figure is directly reproduced from Reference[33]. It shows the density of states of electrons in a solid as function of the local Coulomb interaction, where U is the interaction energy and W the bandwidth of the noninteracting electrons.(a) For independent electrons, one obtains a half ellipse, filled up to the Fermi energy E_F. (b) For weakly correlated systems the DOS still resembles the free electrons. (c) In strongly correlated materials one finds a characteristic three-peak structure: the two Hubbard bands and a quasiparticle peak near the Fermi level. (d) The Mott-Hubbard insulating state where the electron interaction are strong enough to suppress the quasiparticle peak, whose weight is transferred to the Hubbard bands.

When one start to consider the role of the ligands, the charge transfer energy has to be introduced in order to describe the band gap. The charge transfer energy (Δ) is defined as the

energy cost to transfer an electron from the ligand to the metal ion, which is directly related to the energy positions of the oxygen levels. It is commonly used to describe the scenario when the O $2p$ band lies between the lower and upper Hubbard bands and the magnitude of the band gap is determined by Δ. Zaanen, Sawatzky, and Allen have provided a clear classification scheme based on the Anderson-impurity model, to describe the dependence of the band gap on ω, Δ, and U[34].

2.3.1. Resonant Photoemission

For 3d transition metal oxides, the valence band spectra are not straightforward to analyze, because the binding energies of the transition metals and the low lying ligand states of the O $2p$ shell are close to each other or even overlap. This makes it difficult to extract the properties of the transition metal. From the experimental spectra, however, with resonant photoemission at the transition metal $2p$ threshold, the incident photon energy resonates with a core-electron $2p$ to $3d$ excitation, the features belonging to the $3d$ shell can be enhanced in the valence band. Since the absorption process is sensitive to the element and charge, one can observe the change of the spectra as a function of the photon energies, and therefore more detailed information can be deduced. This can be understood by considering not only direct photoemission process, but on resonance another indirect excitation channel involving core level absorption and subsequent Auger-decay contributes to the spectra weight[35]. The indirect excitation channel for transition metal can be described as follows :

$$2p^6 3d^n + hv \longrightarrow 2p^5 3d^{n+1} \longrightarrow 2p^6 3d^{n-1} + e^-$$
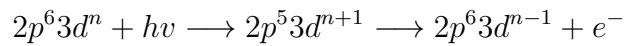
. This process involves a core level absorption where one electron from the $2p$ shell gets excited into the 3d shell, and a subsequent Auger decay where one electron from the $3d$ shell goes back to the $2p$ shell while another electron is excited and escapes from the atom. These two processes with the same final states interfere with each other, and result in asymmetry of the RESPES intensity as a function of the incident energy [36].

2.3.2. Experimental conditions

The spectroscopic measurements in this thesis are carried out at the Dragon Beamline of the National Synchrotron Radiation Research Center (NSRRC) in Hsinchu, Taiwan with an energy resolution of about 0.3eV at the Fe-L_3 edge. Clean Sample surfaces are obtained by cleaving the single crystal $insitu$ in an ultra-high vaccum chamber with a pressure of 10^{-10} mbar. The absorption of the $L_{2,3}$ edges of Fe is recorded using the total electron yield mode. The oxygen K edge x-ray absorption is measured by the total electron and fluorescence yield mode. Fe_2O_3 single crystals are also measured simultaneously as energy reference for the Fe $L_{2,3}$ edges. A MBS analyzer is utilized to obtain the PES spectra, with incidient photon energies of 100 eV and 600 eV. By fitting a broadened Fermi function to the Ag spectra, we obtain 0.072eV and 0.24eV as resolution for 100 eV and 600 eV photon energies, respectively.

2.4. Principle of the Mössbauer effect

The principle of Mössbauer spectroscopy is investigating the energy levels of a nucleus (situated in a solid) by measuring the energy dependence of the resonant absorption of Mössbauer gamma rays by nuclei. The gamma ray emission of radioactive nuclei in excited states might excite other nuclei of the same isotope, thereby giving rise to nuclear resonant absorption and fluorescence. Resonant absorption occurs when the energy of the gamma ray just matches the nuclear transition energy for a Mössbauer nucleus in the absorber, see Figure 2.7. A typical Mössbauer spectrum
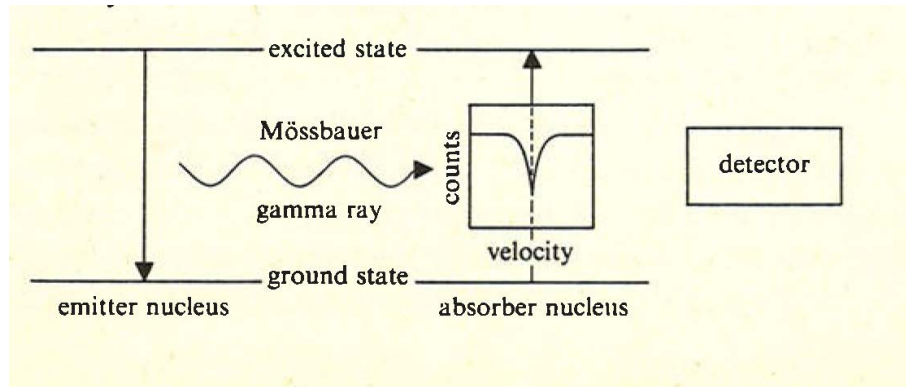
Figure 2.7.: A schematic representation of Mössbauer spectroscopy with the simplest situation of source and absorber nuclei in identical environments and showing the resulting Mössbauer spectrum with an absorption line at zero velocity.[37]

consists of a plot of gamma ray counts(or relative absorption)against the velocity of the source with respect to the absorber, usually measured in millimetres per second, which constitutes the energy axis of this spectroscopy. There are various hyperfine interactions and other effects which determine the nature of the Mössbauer spectrum. But the most general and important factors that one can obtain are isomer shift, quadrupole splitting and magnetic hyperfine splitting.

2.4.1. Isomer shift

As we can see in Figure 2.8, if in a system where there is only electric monopole interaction(Coulomb interaction) affecting the nuclear energy levels, the nuclear ground and excited states are unsplit,but their separation is different in the source and absorber by an amount given by the isomer shift δ. When additional hyperfine interactions are present the isomer shift sets the position of the centre of gravity of the whole Mössbauer spectrum.

All hyperfine parameters of the Mössbauer spectrum are a function of both nuclear and electronic properties of the system. The isomer shift is the result of electric(Coulomb) interaction between the nuclear charge distribution over the finite nuclear volume and the electronic charge density over this volume.

$$\delta = \alpha[|\psi_A(0)|^2 - |\psi_S(0)|^2] \tag{2.6}$$

where the constant of proportionality α depends principally on the relative change in the nuclear radius between the excited state and the ground state δR/R. $|\psi_A(0)|^2$ and $|\psi_S(0)|^2$ correspond to the total electron density at the nucleus of the absorber and the standard separately. The major
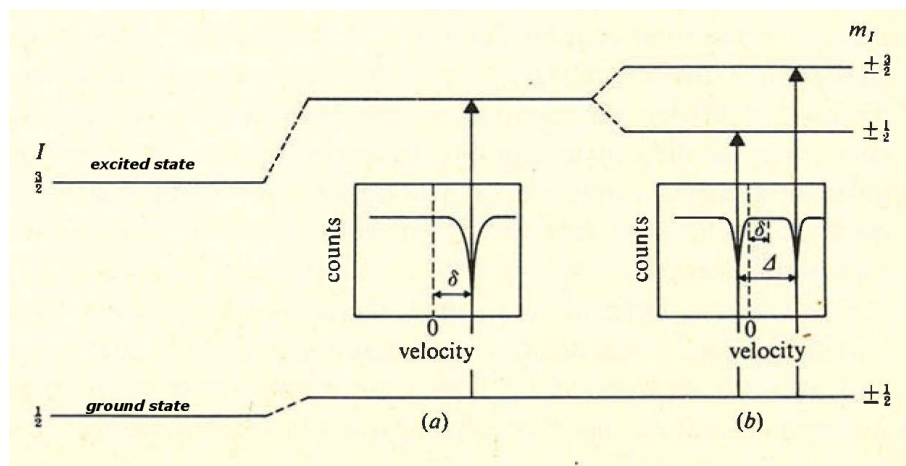
Figure 2.8.: The effect on the nuclear energy levels of ^{57}Fe of (a)the isomer shift and (b)the quadrupole splitting.[37]

contribution to the total electron density at the nucleus comes from the 1s electrons. Other s electrons make lesser contributions as the principal quantum number increases, while p and d electrons exert shielding effects. If the nuclear radii of the ground and excited states are known, the electronic parameters(electron densities) at the Mössbauer nuclei in the source and absorber can be obtained. The S electronic densities are dependent on the electronic structure of the atom and hence the isomer shift is an important mean by which atomic oxidation states as well as chemical bonding can be investigated. For ^{57}Fe, α is negative as δR/R < 0 for this isotope. Generally the isomer shift becomes more positive as the number of d electrons increases,i.e. as the s electron density becomes more shielded. When the iron ions have a high spin configuration, there is a sharp distinction between oxidation states.But if ligands are sufficiently strong in the spectrochemical series the crystal field is large, giving spin pairing and a low spin configuration, the isomer shift values cover much narrower ranges, and the sharp distinction between oxidation states is lost. For instance, spin pairing in iron compounds produces a decrease in the isomer shift, i.e.an increase in s electron density at the nucleus.

2.4.2. Quadrupole splitting

Nuclei in states with a nuclear angular momentum quantum number I>1/2 have non-spherical charge distributions and therefore a non-zero quadrupole moment. A quadrupole split Mössbauer spectrum results from a nucleus with an electric quadrupole moment which experiences an electric field gradient(EFG).An EFG results from the distribution of charge around the nucleus which has less than cubic symmetry. The EFG can be specified by its principal component:

$$V_{zz} = \frac{\partial^2 V}{\partial Z^2} = \frac{1}{4\pi\varepsilon_0} \sum_i q_i r_i^{-3} (3\cos^2\theta_i - 1) \tag{2.7}$$

where the summation is over all charges q$_i$ with polar coordinates r$_i$ and θ_i. If the EFG has axial symmetry: -1/2V$_{zz}$=V$_{xx}$=V$_{yy}$. The charges concerned may be external to the Mössbauer atom (lattice charges) giving a contribution(V$_{zz}$)$_{lat}$ or maybe due to the electrons of the bond system

or to the non-bonding electrons, giving contributions $(V_{zz})_b$ and $(V_{zz})_{nb}$ respectively. The last two are often treated together as the valence shell contribution $(V_{zz})_{val}$. For non-axial symmetry another parameter is required to specify the EFG in addition to the principal component, namely the asymmetry parameter $\eta=(V_{xx}-V_{yy})/V_{zz}$ ($0 \leq \eta \leq 1$) All Mössbauer nuclei possess a quadrupole moment in either the ground or excited state or both, and are therefore liable to show quadrupole splitting. An inhomogeneous electric field produced by a non-cubic electronic charge distribution and/or by a non-cubic ligand arrangement give rise to a non-zero electric field gradient and therefore to a splitting of the nuclear energy levels. The different nuclear energy levels directly correspond to the alignments of the quadrupole moment with respect to the principal axis of the electric field gradient. For a given nuclei, the value of the nuclear quadrupole moment is fixed, so the information that can be derived from the Mössbauer spectrum is about the details of the EFG. In case of ^{57}Fe, the I=3/2 excited state is split by the quadrupole splitting into the $m_J=\pm$ 1/2 and $m_J=\pm$ 3/2 states. Its a result one obtains a quadrupole doublet in the Mössbauer spectrum (Figure 2.8)

2.4.3. Mössbauer spectrum for magnetic materials

The magnetic splitting arises from the interaction between nuclear magnetic moment and the magnetic field, when a nucleus is placed in a magnetic field. In the case of ^{57}Fe, the ground state with I=1/2 splits into two sub-states and the excited state with I=3/2 splits into four sub-states. The selection rule ($\triangle m_I=0, \pm1$) leads to six possible transitions and therefore six absorption lines in a Mössbauer spectrum, see Figure 2.9
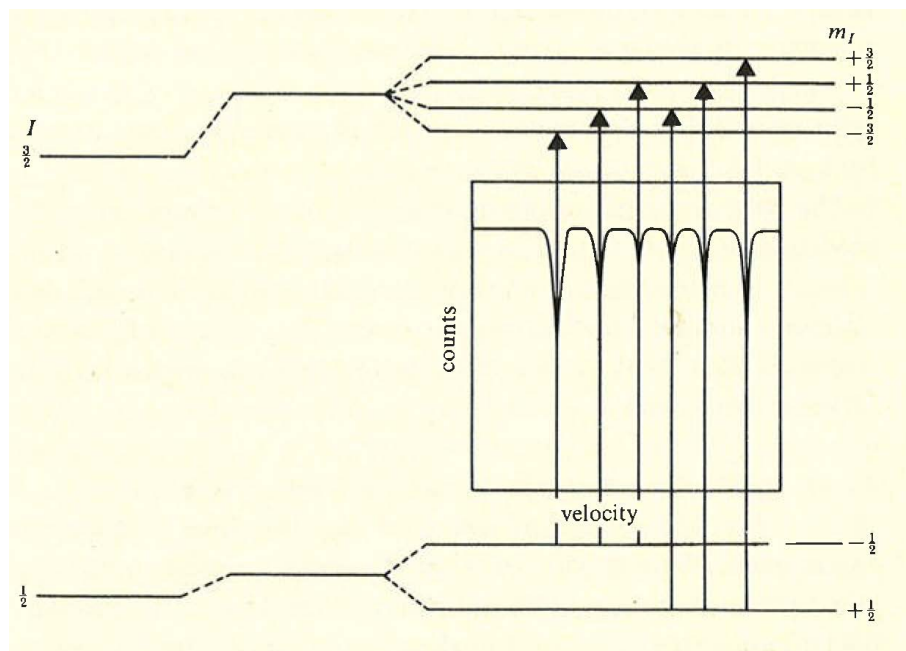

Figure 2.9.: A copy of Reference[37]. The effect of magnetic splitting on the nuclear energy levels of ^{57}Fe, showing the Mössbauer absorption transitions and the resulting spectrum in the absence of quadrupole splitting. The overall splitting of the lines in the spectrum is proportional to the total magnetic field at the nucleus.[37]

Quite often, the Mössbauer spectra are used to investigate magnetic solids, especially iron compounds. In this case, spin Hamiltonians are defined in order to represent the energy level for the different states caused by direct or indirect interaction of the Mössbauer nucleus and its environment. Despite the complex mathematic formulae Spin Hamiltonian for the magnetic solid, the most important term that forms Spin Hamiltonian formulae, without the applied external field, are the magnetic hyperfine interactions I· A · S and electric quadruple interactions $\Delta = \frac{1}{2}eQV_{zz}(1 + \eta^2/3)^{\frac{1}{2}}$.For convenient usage, the nuclear-atom magnetic interaction is always expressed in terms of an internal magnetic field called the hyperfine field, B_{hf}. and it is composed of three components:

$$B_{hf} = B_c + B_{orb} + B_{dip} \tag{2.8}$$

B_c is the contact interaction whereby a static non-zero spin of a partly-filled atomic shell polarises the s electrons which have a finite density at the nucleus to give a net spin density at the nuclear site. B_{orb} is the magnetic field produced at the nucleus by the orbital motion of the electrons of the partly-filled shell. B_{dip} the magnetic hyperfine interaction produced by the dipolar field of the spins of the 3d or 4f electrons.

2.4.4. Experimental conditions

Our Mössbauer measurements were performed using a constant acceleration HALDER-type spectrometer with a room temperature ^{57}Co source (Rh matrix) in transmission geometry. Poly-crystalline absorbers containing about 10 mg cm^{-2} of iron were used to avoid the experimental widening of the peaks. The velocity was calibrated using pure α-Fe as the standard material at 293K. The data were analyzed using standard computer software with different fitting modes (distribution of quadrupole doublets and a superposition of several sites with Lorentzian lineshapes) for the low temperature and room temperature spectra.

2.5. Principal of μSR

μSR is an acronym for muon spin rotation, relaxation or resonance.It utilizes a short-lived subatomic particle called a muon, whose spin and charge are sensitive local magnetic and electronic probes of matter. Muons are particularly very sensitive to small internal magnetic fields making them very usable to measurements where magnetism is weak or dilute. It is also a good complementary technique to the relatively faster neutron scattering and the slower NMR. It is a valuable probe in studying materials in which the magnetic order is random or of very short range. The detective range of μSR for static field distribution sensitivity is 10^{-3}-$10^{-4}\mu_B$ and for fluctuation rates are 10^5-10^9 Hz.

The muon was discovered as a secondary radiation from cosmic rays. It is a result from pion decay in which the weak interaction responsible for the decay violates parity. This violation of parity actually gives the unique characteristics of the muon that make it suitable for μSR spectroscopy.[38]

The muon is an unstable particle, with a lifetime of only two millionths of a second. Muons are spin-$\frac{1}{2}$ particles that carry a positive (μ^+) or negative (μ^-) charge, and spontaneously decays

into a positron (or an electron) and a neutrino anti- neutrino pair as follows[38]:

$$\mu^+ \longrightarrow e^+ + v_e + \overline{v_\mu} \qquad (2.9)$$

$$\mu^- \longrightarrow e^- + \overline{v_e} + v_\mu \qquad (2.10)$$

Although either positive or negative muons can be used to perform μ^+SR, their very different behavior in matter makes μ^+ more suitable for most condensed matter physics or chemistry applications. Having a negative charge, μ^- behaves as a heavy electron and is easily captured into the atomic orbitals while μ^+ avoids the positively charged nuclei in the host material. For our purpose, we made use of the positive muon to probe the magnetic properties of our sample.

There are three main muon characteristics that make μ^+SR spectroscopy possible: 1.) The muon is 100% polarized, 2.) The decay positron is preferentially emitted along the muon spin direction, 3.) The muon precesses in a magnetic field.

Once implanted in the sample, it probes the local field at its site. The muon spin behavior inside a material is relayed to us via its decay positron. This positron is preferentially emitted in the direction of the muon spin at the instant of decay. Detection of the positrons emitted from a sample following implantation of polarized muons therefore gives information about the muon spin interactions within the compound. μ^+SR experiments involve what we call time-differential measurements where we follow the muon polarization as a function of time. One has the advantage of choosing from a number of different experimental configurations when doing a μ^+SR experiment: the Transverse Field (TF- μ^+SR), the Longitudinal (LF- μ^+SR) and Zero Field (ZF- μ^+SR) geometries.

TF- μ^+SR involves the application of an external magnetic field perpendicular (transverse) to the initial direction of the muon spin polarization. Figure 2.10 shows a schematic diagram of a Muon Spin Rotation experiment with transverse applied magnetic field with the output data that one can analyze and obtain information about the magnetic properties of the material. In an external or internal magnetic field, the muon spin precesses with the Larmor frequency, $\omega = \gamma_\mu B$, around that field. The muon decay is anisotropic and the positron is preferentially emitted along the direction of the muon spin of the moment of the decay. Therefore, if muons decay fast, the positron emitted is preferentially detected by the backward detector. Otherwise, if decay is later, the positron emitted is detected by the forward detector. Thus the positron beam from an ensemble of precessing muons can be likened to the beam of light from a lighthouse. The time evolution of the numbers of positrons in the forward and backward detectors is described by two functions, the forward function NF(t) and backward function NB(t), respectively. Thus, the muon spin polarization can be obtained by examining the normalized differences of these two functions via the asymmetry function A(t)[38]

$$A(t) = \frac{N_B(t) - N_F(t)}{N_B(t) + N_F(t)} \qquad (2.11)$$

As already mentioned, the muon undergoes Larmor precession in a magnetic field, internal or external and this precession can be followed by measuring the asymmetry. The frequency of precession is directly related to the magnetic field. Therefore, implanted muons in magnetically ordered materials precess in the internal magnetic field and directly yield oscillating signals
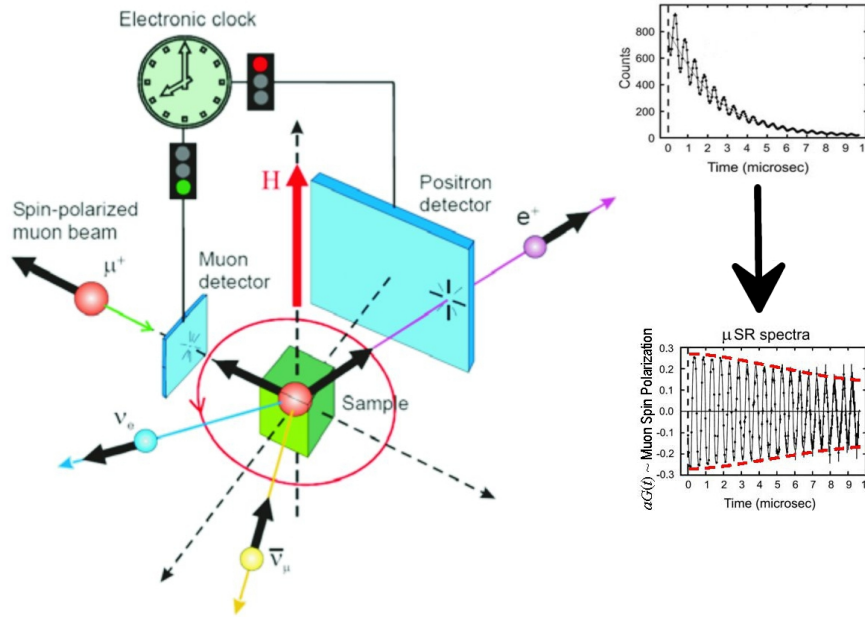
Figure 2.10.: Schematic of transversal field- μ^+SR of the μ^+SR. A plot of Muon Spin Polarization versus Time as the output during the experiment[39]

whose frequency is proportional to the internal magnetic field. LF- μ^+SR involves the application of an external magnetic field parallel to the the initial direction of the muon spin polarization. In this geometry, one measures the time evolution of the muon polarization along its original direction.

ZF- μ^+SR is a special case of the LF configuration done with the absence of an external field. This is a very sensitive method of detecting weak internal magnetism that arises due to ordered magnetic moments, or random fields that are static or fluctuating with time. In the ZF configuration, the muon is only subject to the internal magnetic fields at the place where it comes to rest, the muon site. Local fields are due either to nuclear magnetic moments (often static in the time window of the μ^+SR experiment) or to electronic moments. The capability of studying materials in zero external fields is a big advantage of μ^+SR over other magnetic resonance techniques. Figure 2.11 shows a schematic diagram of a ZF-μ^+SR experiment.

From the schematic diagrams, an electronic clock is started just when a muon is implanted into the sample. The clock is then stopped when the positron produced by the muon is detected. A histogram is built from the positron counts versus the time spent by the muons in the sample. The decay of the average count demonstrates the finite muon lifetime. An excess or a shortage in the actual counts is reflected in the anisotropy of the muon decay. This deviation from the mean provides the physical quantity that gives the physics, $a_0P_\alpha(t)$, which is called asymmetry because it quantifies the asymmetry of the muon decay. The parameter a_0 is the initial asymmetry and $P_\alpha(t)$ the normalized polarization function ($|P_\alpha(t)| \leq 1$), which is commonly denoted as the muon polarization function.

The polarization functions monitor the properties of local magnetic field ($B_{l}oc$) through Larmor precession. If all the muon spins precess in the same local field $B_{l}oc$ oriented at an angle θ from
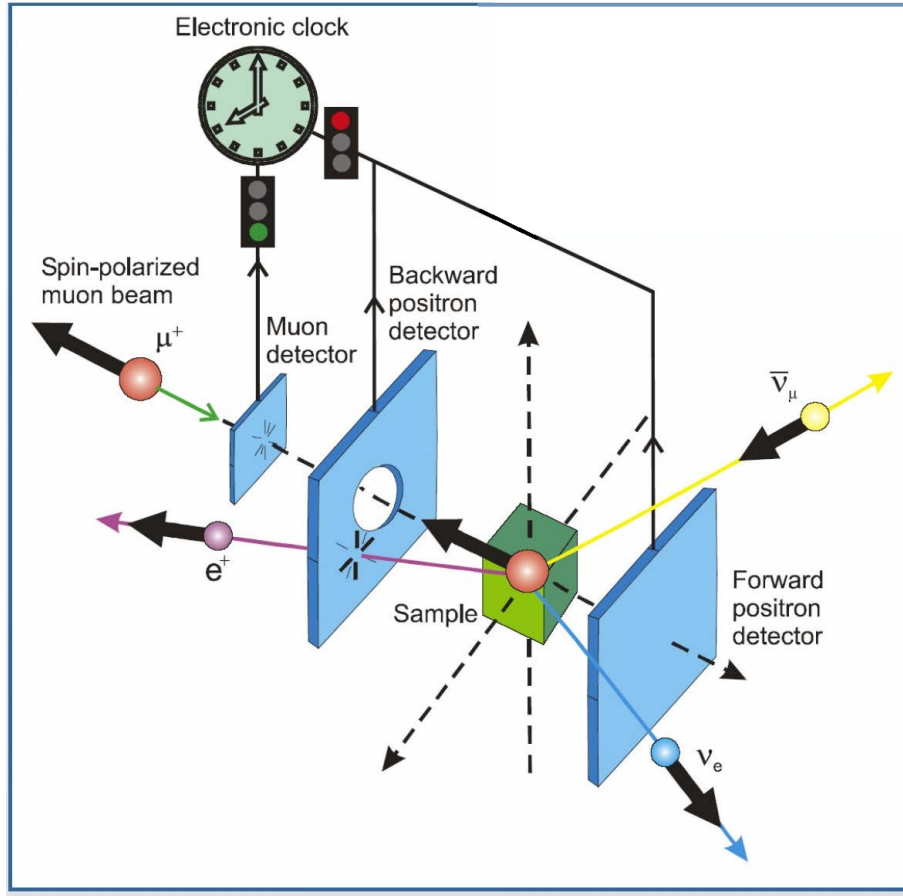
Figure 2.11.: Schematic of a Zero-Field μ^+SR experiment[39]

S_μ, the Larmor equation yields the important result[38]:

$$P_z(t) = \cos^2(\theta) + \sin^2(\theta)\cos(\omega_\mu t) \tag{2.12}$$

In this equation, $\omega_\mu = \gamma_\mu B_{loc} = 2\pi\nu_\mu B_{loc}$ where γ_μ is the precession frequency and γ_μ is the muon gyromagnetic ratio (γ_μ=851.6 Mrad s^{-1} T^{-1}). The gyromagnetic ratio is related to the muon magnetic moment m$_\mu$ through the relation[38]

$$m_\mu = \gamma_\mu \hbar S_\mu \tag{2.13}$$

with S$_\mu$ = 1/2.

As a simple application of the previous equation, let us consider a magnet in zero external magnetic field[40]. The local field at the muon site is usually not zero in the ordered phase: we denote this spontaneous field by B$_0$. For a magnet in polycrystalline form, the spatial average of equation(2.12) must be performed. If the crystallites in the sample have no preferred orientation, we obtain for the ordered magnetic state[38]

$$P_z(t) = 1/3 + 2/3\cos(\omega_\mu t) \tag{2.14}$$

The oscillating component reflects the magnetic order in the compound. We assume the presence of only one type of muon localization site characterized by a single spontaneous local

field. If the magnet is not perfectly ordered, i.e. if its correlation length is relatively small, the local field can take a large number of values close to each other. Then the oscillation is strongly damped and can even disappear. If the muon spins precess too quickly relative to the time resolution of the spectrometer, the oscillation will be averaged out to zero and the resulting muon polarization will be constant at a level of 1/3 . Then, at a magnetic phase transition, if no wiggles are observed in the muon signal, one expects a drop in the effective initial asymmetry, a_{eff}, from $a_{eff} = a_0$ in the paramagnetic state to $a_0/3$ in the ordered state.

Chapter 3.

Synthesis, characterization, magnetic and electronic structure of $Sr_3Fe_2O_6$

The Ruddlesden-Popper series with its general chemical formula $Sr_{n+1}Fe_nO_{3n+1}$,(n=1,2,3...∞) form a group of layered perovskites. These types of structure consist of slabs of n layers of corner-sharing FeO_6 octahedra separated by inter layers of rock salt structure SrO. By changing the number of n, the magnetic and electronic structures change drastically with the modification of the nuclear structure . For the extreme case, when $n = 1$, the structure has only one layer of octahedra e.g., Sr_2FeO_4 , K_2NiF_4, and La_2CuO_4. While when $n = \infty$, the structure is a simple perovskite such as $SrFeO_3$, $LaCoO_3$ and $RETiO_3$(RE is a rare-earth element). Tremendous efforts have been made to understand the huge variety of physical properties found in these compounds [41–43]. $Sr_3Fe_2O_{7-x}$ belongs to the oxygen deficient derivatives of the Ruddlesden-Popper type structure, and its oxygen stoichiometric compound $Sr_3Fe_2O_7$ ($n = 2$ of the Ruddlesden-Popper series) are characterized by a two dimensional network of double layers of FeO_6 octahedra. The crystal structure of the oxygen deficient derivatives can be explained by removing the oxygen between the double layers of FeO_6. When the oxygen stoichiometry changes to x=1, the oxygen sites, which link together the FeO_6 octahedra in double layers, are all removed. Consequently, the coordination of iron changes from six-fold octahedral to five-fold base pyramidal. This five-fold base pyramidal coordination of Fe^{3+}, in comparison to octahedral or tetrahedral coordinations, is quite unusual in nature [44]. For instance, $LaFeO_3$ has Fe^{3+} in octahedral coordination and is a very stable antiferromagnetic insulator with Néel transition temperature around 750 K [45]. $YBaCo_3FeO_7$ has Fe^{3+} in tetrahedral site, and two magnetic phase transitions, around 590 K and 50 K[46]. $Sr_3Fe_2O_6$ has Fe^{3+} situated in only pyramidal sites, and is reported to have an antiferromagnetic transition temperature around 550 K [47]. A thorough theoretical and experimental understanding of the electronic structure of $Sr_3Fe_2O_6$ is still lacking. Zainullina et al. have studied the electronic and magnetic structure with an ab initio LSDA+U approach and proposed a high spin state [47], with a mixture of d^5 and $d^6\underline{L}$ configurations, where $\underline{L}$ denotes a hole on the oxygen ligands. The prevalence presence of $d^6\underline{L}$ as found by Zainullina et al. is explained due to the electron with opposite spin pass from oxygen p orbital to the splitted e_g orbital of Fe, similar to the tetravalent Co compound $SrCoO_3$. This is very surprising for Fe^{3+} compounds, which are usually seen as being dominated by the $3d^5$ configuration, e.g.the Fe-$L_{2,3}$ XAS spectrum of Fe_2O_3 , Fe^{3+} can be well reproduced by an atomic multiplet calculation [48]. The resulting magnetic moment of the unusual configuration $t_{2g}^{3\uparrow}e_g^{2\uparrow}e_g^{1\downarrow}$ [47] in $Sr_3Fe_2O_6$is 3.94 μ_B from the LSDA+U calculation , lower than the expected spin-only value of 5 μ_B for high spin Fe^{3+} . This theoretical explanation is a bit surprising and there is no experimental approval until now according to our knowledge.

In order to clarify the electronic and magnetic structure of $Sr_3Fe_2O_6$, we have prepared highly pure polycrystalline samples and carried out neutron diffraction, as well as x-ray absorption spectroscopy combined with full-multiplet cluster calculations.

3.1. Synthesis of $Sr_3Fe_2O_6$

The oxygen-deficient $Sr_3Fe_2O_{7-x}$ phase with $x \leq 1$ has been synthesized by solid state reaction and by wet-chemistry method which provides more homogeneous precursors.

The solid state reaction is performed according to Ref. [49]. $SrCO_3$ (Alfa Aesar Ref:012593) and Fe_2O_3 (Sterm Chemicals Ref:933803), with the purity of 99.9% and 99.99% respectively, are used as the starting reactants. The $SrCO_3$ is preheated under 523K for 10h to remove the absorbed water. The mass of $SrCO_3$ and Fe_2O_3 are weighted according to the molar ratio 1:1. The control of the molar ratio of Fe/Sr is very important for the single phase preparation as the by-phase product $SrFeO_{3-x}$ is quite easy formed during the reaction [50]. The mixed powder is ground with ethanol for half an hour and dried in air. Then the mixture is heated in air at 1173 K for one night to remove CO_2 and then ground again. The intermediate product is then put into the furnace at 1573 K for 90h with intermediate grinding until the x-ray diffraction pattern show single phase pattern, named sample A.

For the wet-chemistry method, we have used two different ways. In both cases, we need to preheat $SrCO_3$ (99.99% Alfa Aesar) to remove the absorbed water as described above. The main difference of the two methods are the starting materials. One way is, according to Ref. [51], started with $Fe(NO_3)_3 \cdot 9H_2O$ (98+%) from Alfa Aesar Ref:12226 as one of the precursors.
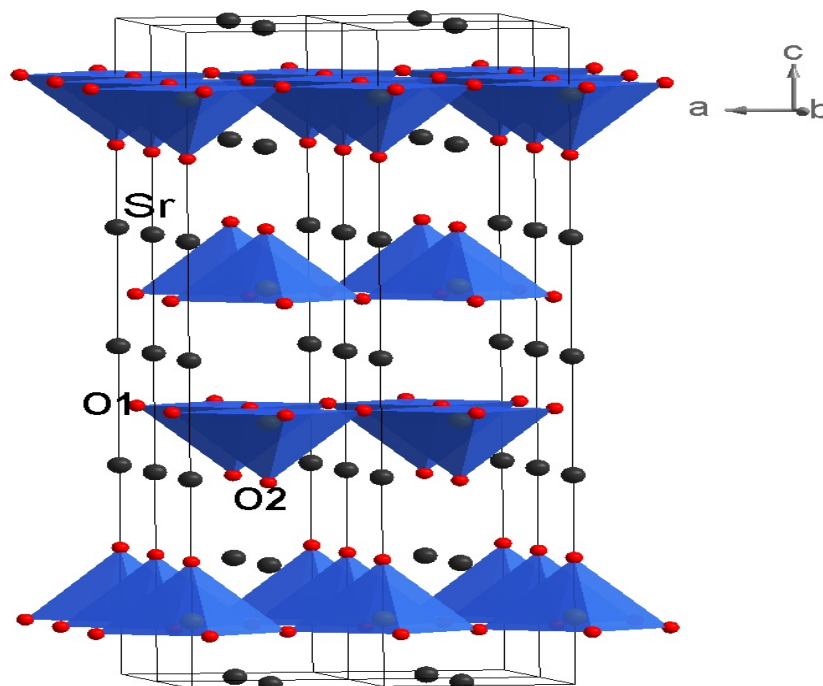

Figure 3.1.: Structure of $Sr_3Fe_2O_6$

There are always some errors from the official marked water content in $Fe(NO_3)_3 \cdot 9H_2O$, as this compound is highly hydrophilic. The precise water content is determined by the weight loss through the decomposition of a certain molar of $Fe(NO_3)_3 \cdot (9+x)H_2O$ into Fe_2O_3 after heating up for several hours in the furnace. The calculated mass of $Fe(NO_3)_3 \cdot (9+x)H_2O$ and $SrCO_3$ are weighted according to the stoichiometry and solved into nitric acid. The control of the molar ratio of Fe/Sr is also paid attention to. The citric acid (99.5% Acros organics) and ethylene glycol (99% Alfa Aesar) are added to the solution and dissolved, supported by stirring. The ammonium hydroxide (28% Alfa Aesar) is added until the solution is basic, as tested by litmus paper. The solution is then slowly evaporated at 180 °C on a hotplate with magnetic stirring. The left resin is heated at 923 K to decompose the organic compounds. A grey powder is then ground and calcined in air at 1473 K for 72h with intermediate grinding until the x-ray diffraction pattern show single phase pattern, named sample B.

The other way is started with $SrCO_3$ and iron powder(99.9+% Alfa Aesar). They are weighted according to the stoichiometric amounts and dissolved in nitric acid. The control of the ratio of Fe/Sr is also paid attention to. Similar to the procedure described above, an excess amount of citric acid (99.5% Acros organics), ethylene glycol (99% Alfa Aesar), and ammonium hydroxide (28% Alfa Aesar) are added to the solution. The pH value of the solution is adjusted into the basic regime. After the solution is dried on a hotplate, the calcination steps of the left product are the same as in the other wet chemistry method. The final product is named sample C.

After the above steps of synthesis, the black powder of the parent $Sr_3Fe_2O_{7-x}$ compound is immediately put into pure hydrogen atmosphere in a well sealed furnace so that no traces of oxygen can go inside the furnace and the reduction takes place at 625K for 10h. The final reduced product $Sr_3Fe_2O_6$ is achieved after heat treatment and furnace cooling into room temperature.

3.2. Crystal structure of $Sr_3Fe_2O_6$

The reported crystal structure of $Sr_3Fe_2O_6$ is tetragonal (I/4mmm space group) with unit cell parameter a=3.8940Å and c=20.0396Å[49], see Figure 3.1. The Fe^{3+} cations are sitting in five coordinated pyramidal sites. Unlike $Sr_3Fe_2O_7$ having double layers of octahedra stacking along the c axis, $Sr_3Fe_2O_6$ has only double layers of pyramids. The oxygen linking together the double layers of octahedra in $Sr_3Fe_2O_7$ is removed in $Sr_3Fe_2O_6$, leaving two types of oxygen anions: the O(1) in the basal plane and the O(2) in the rock salt layers.

Neutron diffraction and X-ray diffraction have been used to study the crystal and magnetic structures of $Sr_3Fe_2O_{7-x}$[49, 52–54]. According to our knowledge, no detailed neutron diffraction data on the most reduced phase $Sr_3Fe_2O_6$ has been reported until now.

Our samples from different synthetic routes are checked before and after reduction by powder X-ray diffraction on a HUBER G670 imaging plate Guinier camera with Co K$_{(\alpha 1)}$ radiation ($\lambda = 1.78919$ Å, 2θ interval of 3.5-100.5°, exposure time 15mins). The reduction phase of the sample C is measured at D2B at ILL in Grenoble France with wavelength $\lambda = 1.6$Å . The data is refined with Fullprof-suite software. An initial structure model I4/mmm is used for indexing the neutron powder diffraction pattern as proposed by Sandra E.Dann[49]. During the refinement the Pseudo-Voigt function is used for the peak shape. The background is refined with a linear interpolation of N selected points. The cell parameters, atomic positions and isotropic thermal
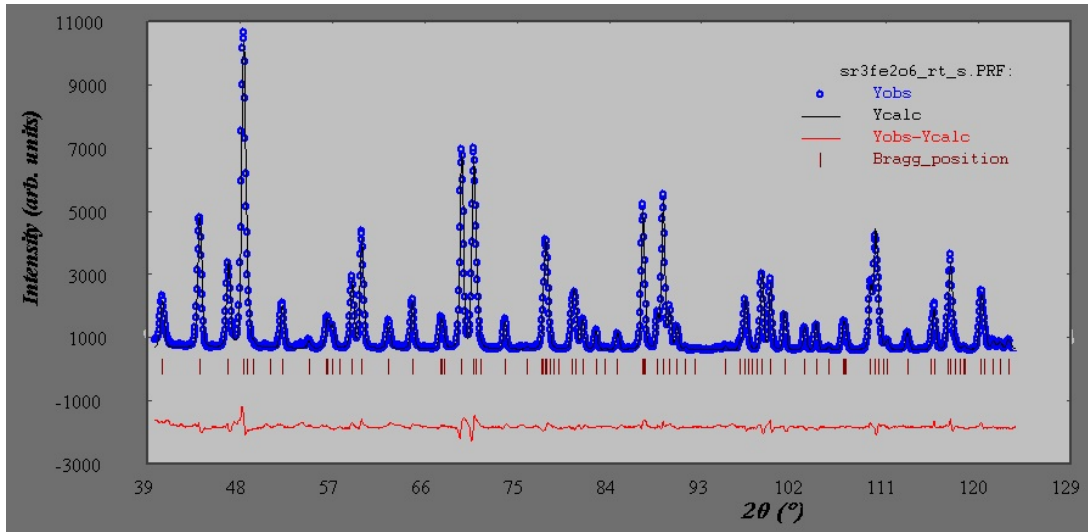
Figure 3.2.: Neutron powder diffraction pattern of $Sr_3Fe_2O_6$ at room temperature, data taken from D2B in ILL, λ= 1.6Å. Black line: measured data I_{obs}; Red bars: peak positions of the nuclear peaks; Blue circles: Rietveld fit (I_{calc}); Red line: the difference between I_{obs} and I_{calc}

Atom	X	Y	Z	Biso($\mathring{A}^2$)
Sr1	0.0000	0.0000	0.5000	0.626(41)
Sr2	0.0000	0.0000	0.31966(7)	0.531(29)
Fe1	0.0000	0.0000	0.10218(5)	0.355(21)
O1	0.0000	0.50000	0.08459(6)	0.718(26)
O2	0.0000	0.0000	0.19651(9)	0.751(32)

Table 3.1.: Structure parameters for $Sr_3Fe_2O_6$ at room temperature from neutron powder diffraction refined in I4/mmm space group. a=3.90743(6)Å,b=3.90743(6)Å,c=20.11332(36)Å. $R_{Bragg} = 4.01$, R_f=3.01, Chi2=32.3

parameters are modified during the refinement. The occupancies are fixed. An excellent fit of the observed diffraction data and the calculated profile is obtained in Fig 3.2, the structure parameters are listed in table 3.1. The distances between iron and five coordinated oxygen are 1.9855(2)Å$\ast$ 4 and 1.898(2)Å.

3.3. Mössbauer spectra of $Sr_3Fe_2O_6$

Previous Mössbauer spectra of $Sr_3Fe_2O_6$ have been fitted with one major magnetic hyperfine sextet and another second phase[55], see Fig 3.3. The single magnetic hyperfine sextet has an isomer shift δ=0.12 mm/s at 298K, which is assigned to Fe^{3+} and the second phase with an isomer shift δ=0.19 mm/s is explained as Fe^{4+} species. As illustrated in Chapter 2, if the number of d electron increases, the s electrons become more shielded and the isomer shift is more positive. Thus, the Fe^{3+} has a more positive isomer shift than Fe^{4+} . The charge assignment from the different isomer shifts in the work of P. K. Gallagher is apparently doubtful. However, it is noted that the isomer shift of a given charge state also depend on the coordination geometry.
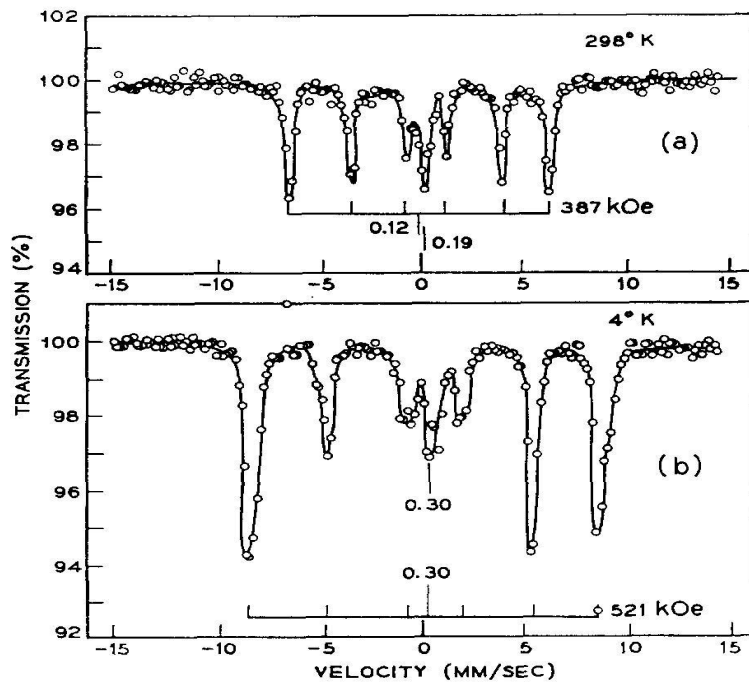
Figure 3.3.: Mössbauer spectra of $Sr_3Fe_2O_{6.0}$ at room and low temperature.[55]

Different batches of the samples that are synthesized during this PhD thesis have been checked by Mössbauer measurements, using the setup that mentioned in Chapter 2. The results are shown in Fig 3.4. We can see a single magnetic hyperfine sextet as the majority phase in all the spectra of the reduced products of the sample A, B, C. This sextet has an isomer shift δ=0.29 mm/s which is typical for Fe^{3+} . The magnetic hyperfine interactions arise from the interaction between the nuclear magnetic moment and the electronic magnetic moment. The latter is due to the spin order which develops below the Néel temperature T_N for antiferromagnets or the Curie temperature T_C for ferromagnets and leads to a local spin <S>$\neq$0 at the iron site. In the case of $Sr_3Fe_2O_6$, the magnetic hyperfine splitting of Fe^{3+} confirms the Fe^{3+} magnetically ordered at room temperature and its magnetic transition temperature is higher than room temperature. The distribution of the peaks is not symmetrical with respect to the center of the pattern, especially observable from the difference Δv in Doppler velocities between lines 1/2 and 5/6, respectively. This is in line with the Fe^{3+} in square pyramidal coordination in the structure that can give pronounced quadrupole interaction. Thus, the Fe^{3+} spectrum is modeled by a single hyperfine sextet with the hyperfield B_{hf} and the quadrupole interaction parameter ε. The data evaluation gives the quadrupole interaction parameter ε = -0.17 mm/s in the magnetically ordered phase and the hyperfine field B_{hf}= 38T. All the parameters of Mössbauer analysis for the three batches of sample are shown in Table 3.2. The second phase looks similar like in the reported spectrum shown in Fig 3.3. Its isomer shift is very close to the center of the sextet with δ =0.3 mm/s. But its intensity is lower than the literature reported one's and decreasing from reduction phase of Sample A to reduction phase of Sample B. The main difference between different batches is the synthetic route. The reduction phase of Sample A is made from solid state reaction, while the reduction phase of Sample B and C are from sol-gel method. By comparing with different

(a) Reduction phase of Sample A : Synthesized by Solid state reaction

(b) Reduction phase of Sample B : Synthesized by Sol-gel method, starting with hydrate nitrate of the corresponding cations

(c) Reduction phase of Sample C : Synthesized by Sol-gel method, starting with iron powder and strontium carbonate solving in nitric acid
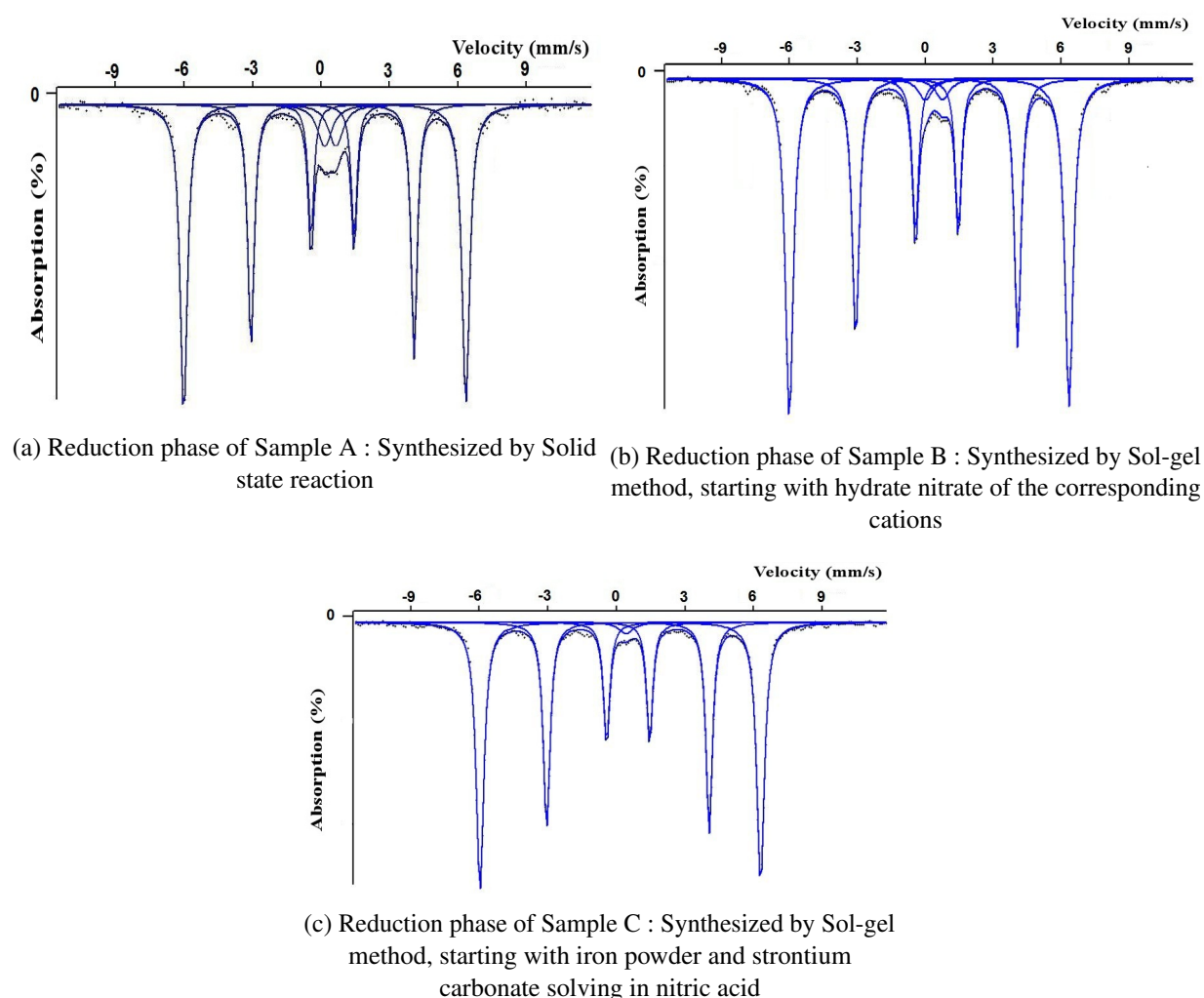
Figure 3.4.: Mössbauer spectra of different batches of $Sr_3Fe_2O_6$ measured at room temperature

iron oxides Mössbauer spectra , we propose this second phase may come from $SrFeO_{3-x}$. The reason for the second phase may be because of the mixing process or the thermal stability of the compounds. As the sol-gel method can give a better homogeneous mixture than the solid state reaction, the intensity of the secondary phase has decreased. Furthermore, the reduction phase of Sample C starts from iron powder and strontium carbonate solved in nitric acid while the reduction phase of Sample B starts from the tradition sol-gel method with nonahydrate iron nitrate and strontium carbonate. This indicates the control of the exact stoichiometry of Sr/Fe is very important as starting with nonahydrate iron nitrate may a give bigger error than with iron powder solved in nitric acid. Thus, the intensity of the secondary phase in the Mössbauer spectra further decreased. From the third batch, the linewidth at half-height for the secondary phase is very high so that the refinement is significantly overlapped with the majority sextet.

Site	δ(mm/s)	Γ(mm/s)	ε(mm s^{-1})	Δ(mm s^{-1})	B_{hf}(T)	%	Synthetic route
1	0.288	0.344	-0.173	-	38.4	88Fe^{3+} Pyramidal	Synthesis(a)
2	0.364	0.785	-	0.497	-	12Fe^{3+} Octahedral	Synthesis(a)
1	0.29	0.36	-0.17	-	38	95	Synthesis(b)
2	0.3	0.5	-	0.8	-	5	Synthesis(b)
1	0.29	0.38	-0.17	-	38	98	Synthesis(c)
2	0.3	0.7	-	-	-	2	Synthesis(c)

Table 3.2.: Mössbauer analysis parameters for the three batches of sample trough different synthetic route.δ is the isomer shift, Δ is the quadrupole splitting, ε is the quadrupole interaction in the magnetically ordered phase , B_{hf}(T) is the magnetic hyperfine field.

3.4. Magnetic structure of $Sr_3Fe_2O_6$

The previously reported magnetic structure of $Sr_3Fe_2O_{6.2}$ from low temperature neutron powder diffraction shows the magnetic unit cell is $\sqrt{2}a \times \sqrt{2}a \times c$ with spin direction antiferromagnetic ordered along c axis [53, 56]. But no detailed magnetic structure information of $Sr_3Fe_2O_6$ is given until now, according to our knowledge.
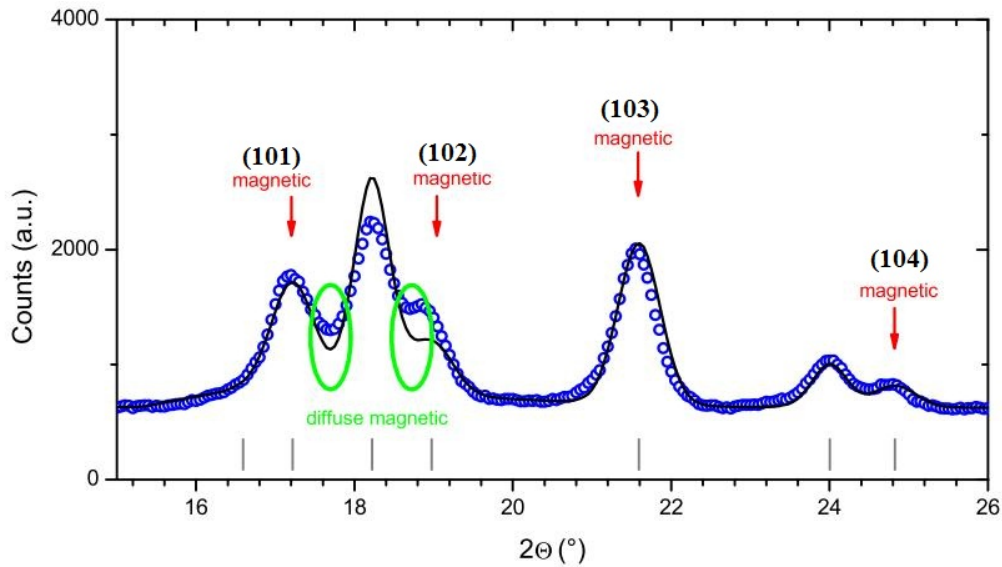
Figure 3.5.: Neutron powder diffraction pattern of $Sr_3Fe_2O_6$ at 10K, data taken from D2B, λ = 1.6Å. Blue circles: measured data I_{obs}; Gray bars: peak positions of the nuclear/magnetic peaks; Black lines: Rietveld fit (I_{calc}). Red arrows: magnetic peaks.

The magnetic structure of the reduction phase of the Sample C has been refined, based on our neutron powder diffraction data, at room temperature and 10K, respectively. Figure 3.5 shows the magnetic refinement at 10K. The strong magnetic peaks are marked in red in the figure. The whole fitting for all the nuclear and magnetic peaks are fitted very well except the first two magnetic peaks (belongs to (10l) reflections). The green circles indicate the discrepancy of the calculated peak intensity and the measured peak intensity. The reason maybe because of the diffused magnetic scattering that some of the magnetic intensity can not be calculated within the

Atom	X	Y	Z	Biso($Å^2$)
Sr1	0.0000	0.0000	0.5000	0.077(41)
Sr2	0.0000	0.0000	0.31980(7)	0.016(29)
Fe1	0.0000	0.0000	0.10211(5)	-0.093(21)
O1	0.0000	0.50000	0.08451(6)	0.195(27)
O2	0.0000	0.0000	0.19680(9)	0.140(32)

Table 3.3.: Structure parameters for $Sr_3Fe_2O_6$ at 10 K from neutron powder diffraction refined in I4/mmm space group. a=3.89889(6)Å,b=3.89889(6)Å,c=20.06899(36)Å. $R_{Bragg} = 5.17$, R_f=4.38, Chi2=41.3

fitting.

Table 3.3 gives the structure parameters of $Sr_3Fe_2O_6$ at 10 K measured by neutron powder diffraction. The negative Debye-waller factor of the iron site may arise from the diffused magnetic scattering or ferromagnetic component in the compound. Unfortunately, these hypothesis have to be proved by magnetization measurement and this measurement hasn't been successfully implemented during the PhD thesis. The magnetic R factor is 14.5% and the magnetic moment on Fe is $3.5\mu_B$ at 10K. For the room temperature refinement, the magnetic R factor is 22.6% and the magnetic moment on Fe is $3.1\mu_B$. The magnetic moment at low temperature on Fe^{3+} site is much lower than theoretical magnetic moment of high spin state Fe^{3+} ($\approx$5 μ_B). The reason may come from the partially disordered iron spin inside the sample. Another assumption for the low magnetic moment is due to strong hybridization of Fe3d-O2p orbitals causing the opposite
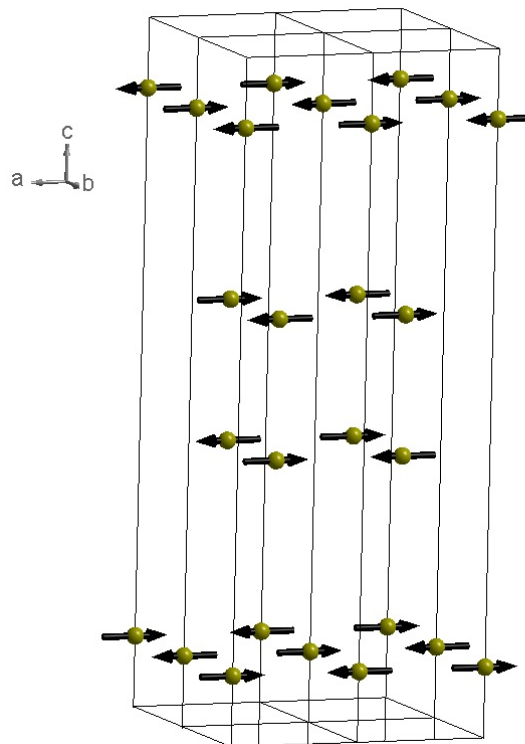

Figure 3.6.: The proposed magnetic structure. For simplicity, strontium and oxygen atoms are neglected.

spin pass from oxygen p orbital to the empty e_g orbital of Fe[47]. From our refinement, we have drawn the schematic picture of the magnetic spin ordering in Figure 3.6. Our refinement clearly indicate the magnetic spin ordering on the iron site are antiferromagnetic ordered in ab plane, in contrary with the previous reported results of $Sr_3Fe_2O_{6.2}$ that the magnetic spins are along c axis[53]. However, the data can be equally described with small angles along a/b axes, it is not possible to distinguish the exactly direction of the spin based on the available data.

3.5. Electronic structure of $Sr_3Fe_2O_6$

The electronic structure of the Ruddlesden-Popper series, containing mainly Fe^{4+}, is characterized by a competition between a local state and an itinerant continuum state. The local state is formally arising from Fe $3d^4$ high spin state and the itinerant continuum state can be formulated as a local $d^5\underline{L}$ configuration with holes having predominantly O $2p$ character. In the two dimensional Ruddlesden-Popper compound Sr_2FeO_4, the local d^4 configuration dominates the ground state, and it is separated by an energy gap from the d^5L^{-1} continuum. Whereas in the three-dimensional perovskite $SrFeO_3$, an increased O $2p$ bandwidth W_p, resulting from the larger numbers of Fe-O-Fe interactions comparing with the two dimensional Sr_2FeO_4, leads a band-gap closure and forms a metallic ground state.

Although the Fe valence is 3+ in $Sr_3Fe_2O_6$ and the sample is insulating, theoretical band-structure calculations show a large contribution of the ligand hole state (d^6L) to the ground state, hinting towards a small value of the charge transfer energy Δ which would be unusual for Fe^{3+} high spin state. With x-ray absorption spectroscopy (XAS), we have a closer look at the electronic states of Fe^{3+} in this compound.

Fig 3.7 shows the experimental Fe $L_{2,3}$ XAS spectra of $Sr_3Fe_2O_6$ along with that of a single crystal of Fe_2O_3 as Fe^{3+} reference. The Fe $2p$ core-hole spin-orbit coupling splits the spectrum roughly in two parts, namely the L_3 (707-710 eV) and L_2 (720-723 eV) white lines regions. The line shape strongly depends on the multiplet structure given by the Fe $3d$-$3d$ and $2p$-$3d$ Coulomb and exchange interactions, as well as on the local crystal fields and the hybridization with the O $2p$ ligands. Unique to soft XAS is that the dipole selection rules are very sensitive in determining which of the $2p^53d^{n+1}$ final states can be reached and with what intensity, starting from a particular $2p^63d^n$ initial state (n = 5 for Fe^{3+}). This makes the technique extremely sensitive to the symmetry of the initial state, i.e., valence states, the spin, orbital and as well as local environment of the ions [30, 57–59]. The main peak of the Fe $L_{2,3}$ structure of the $Sr_3Fe_2O_6$ lie at the same as that of Fe_2O_3 indicating trivalent iron ions in $Sr_3Fe_2O_6$. However, the detailed spectral structure in $Sr_3Fe_2O_6$ is different from that in Fe_2O_3 reflecting a local pyramidal symmetry in the former and octahedral symmetry in the latter. Considering that there is no experimental and theoretical report on the Fe-$L_{2,3}$ XAS spectrum for Fe^{3+} compound in a pyramidal symmetry, we have performed quantitative simulations of the XAS spectra using a configuration-interaction cluster model including full atomic-multiplet theory [60, 61]. The multipole parts of Coulomb interaction and the single-particle SOC constant ζ are estimated from Hartree-Fock values that are reduced to 80%. For the monopole parts of the Coulomb interaction, the typical values are used U_{dd} = 5 eV and U_{pd} =6 eV [30, 61]. The Fe-O hybridization is estimated with Harrison's description. For Fe-O_{apical}, $V_{pd\sigma}$=-1.473 eV, $V_{pd\sigma}$=0.682eV. And for

Fe-$O_{basal_pyramid}$, $V_{pd\sigma}$=-1.747 eV, $V_{pd\sigma}$=0.8088eV. Fig 3.7 shows a good agreement between experiment and theory for the charge-transfer energy Δ =2.5 eV. To check the scenario of a negative charge transfer energy, we present a further simulation of the spectrum in Fig 3.7. It can be seen that the agreement between experiment and the simulation with $\Delta < 0$ is rather poor. This can not only be seen from the fine structure in the line shape, but also in the too small energy separation between the L_3 and L_2 in the theory as compared with experiment.
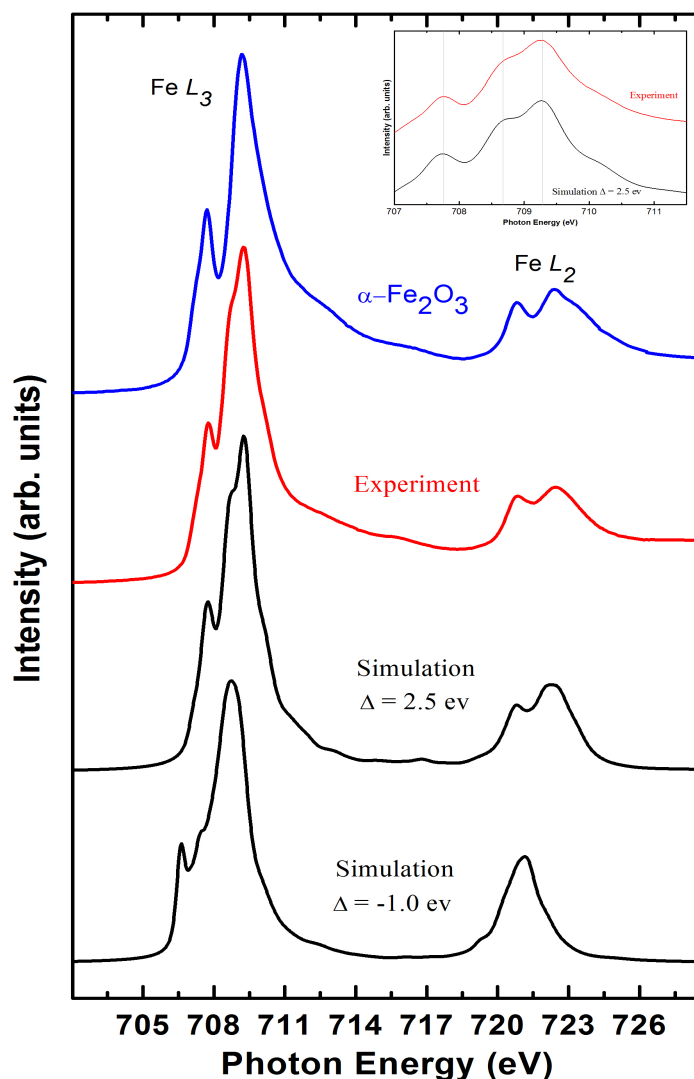
Figure 3.7.: Comparison of Fe_2O_3 (blue), $Sr_3Fe_2O_6$(red) and theoretical simulation with different charge-transfer energy (black).

More spectroscopic features for the high spin Fe^{3+} in the pyramidal FeO_5 coordination can be found in the O K-edge XAS spectrum as shown in Fig 3.9. The structures from 528.5 to 532 eV are due to transitions from the O $1s$ core level to the O $2p$ orbitals that are mixed with the

$$E(x^2 - y^2)$$ ▬▬▬▬

$10Dq = 1.49475$ $\qquad$ $\Delta_{eg} = 0.74657$

$$E(z^2)$$ ▬▬▬▬

$$E(xy)$$ ▬▬▬▬

$$E(xz/yz)$$ ▬▬▬▬ $\qquad$ $\Delta_{t2g} = 0.20442$
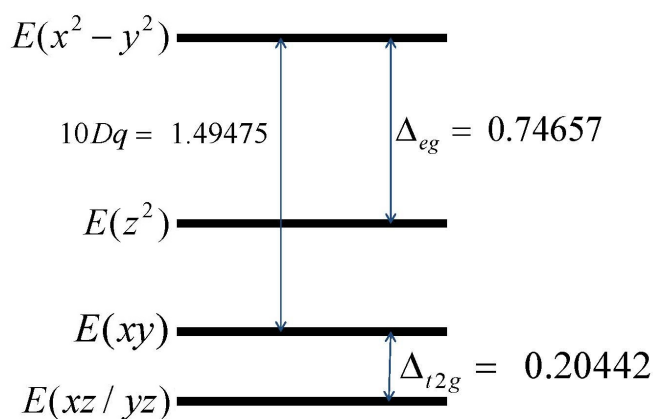
Figure 3.8.: Crystal field splitting energy diagram of $Sr_3Fe_2O_6$

unoccupied Fe $3d$ t_{2g} and e_g states. The broad structures at 533.6 eV found in $Sr_3Fe_2O_6$, which cannot be seen in Fe_2O_3, is indicative of the Sr $4d$ related band. It is now interesting to look for more detailed difference in the oxygen K-edge XAS between $Sr_3Fe_2O_6$ and Fe_2O_3. In the O K-edge spectrum of Fe_2O_3, two features can be seen at 530eV and 531.3eV. These are directly related to the splitting of t_{2g} and e_g states, respectively, in the local O_h symmetry of the FeO_6 octahedron. Because of the missing of one of the apical oxygens in the FeO_5 coordination in $Sr_3Fe_2O_6$, here the level splitting is different. In the full-multiplet calculation the unoccupied $3d_{z^2-r^2}$ level is lower in energy by 0.75 eV compared to the $dx^2 - y^2$, see Fig 3.8. The density states of high lying e_g consists of only $d_{x^2-y^2}$ related states and therefore the related spectral feature appears lower in intensity as compared to the FeO_6 coordination. In this sense, the O
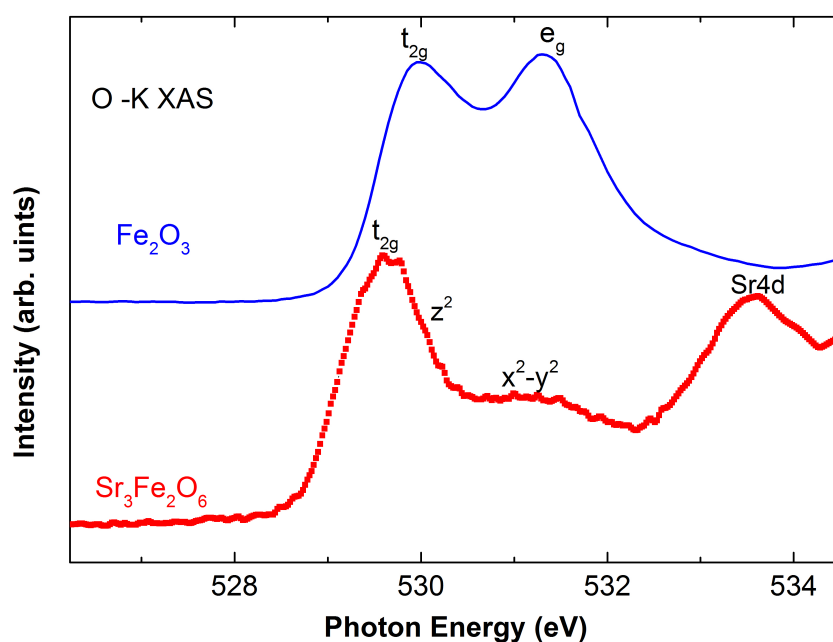
Figure 3.9.: Comparison of oxygen K-edge XAS spectra of $Sr_3Fe_2O_6$ and Fe_2O_3

K-edge spectrum is in good agreement to the calculation of the Fe $L_{2,3}$ edge. The unoccupied O $2p$ states are in fact very similar to these in Sr_2CoO_3Cl with Co^{3+} in the pyramidal CoO_5 coordination [62].

3.6. Conclusion

Different synthetic routes have been used in order to obtain the pure $Sr_3Fe_2O_6$ sample. Neutron diffraction for the crystallographic structure analysis gives the precise bond distances of Fe-O in pure pyramidal sites. The magnetic structure refinement show the magnetic moment on the iron site is $3.5\mu_B$ at 10K and they are antiferromagnetic ordered in the ab plane. By comparing with the previous Mössbauer spectra result, we have further confirmed the purity of our sample. The electronic structure of $Sr_3Fe_2O_6$ has been studied by x-ray absorption spectroscopy. Our experimental spectra of Fe-$L_{2,3}$ is well reproduced by the cluster calculation with the charge-transfer energy Δ=2.5eV, instead of a negative charge transfer energy that we would expected from the previous LSDA+U calculation. With further support from oxygen K-edge XAS spectra, the crystal field splitting energy diagram of this Fe^{3+} in pure pyramidal site is obtained.

Chapter 4.

Synthesis, characterization and electronic structure of $Sr_2Fe_2O_5$

4.1. Synthesis powder and Single crystal of $Sr_2Fe_2O_5$

Solid state reaction is used to prepare rods for the single crystal growth in the floating zone furnace. Preliminary heat treatment of $SrCO_3$ is carried out under 523K for 10h to remove the absorbed water. Stoichiometric $SrCO_3$ and Fe_2O_3 with purities of 99.9% and 99.99%, respectively, from Alfa Aesar Ref:012593 and from Sterm Chemicals Ref:933803 are weighted and mixed together with ethanol by fine grinding. Afterwards the mixture is heated at 1173 K for the pre-reaction. The $SrCO_3$ is decomposed into SrO and partially reacted with Fe_2O_3. The intermediate product is then put into the furnace at 1473K for 48h with intermediate grinding. After furnace cooling, the black powder is put into thin rubber tubes and compressed under hydrostatic pressure of 400 MPa into rods, with diameter of 5 mm and length of 100 mm. The rods are then sintered at 1473 K for 24 hours in air. In order to achieve the reduced oxygen stoichiometric $SrFeO_{2.5}$, the feed and seed rods are resintered under argon atmosphere mixed with 5% hydrogen at 833 K for 12h, with a cooling rate of 1 K/mins in order to avoid stacking faults.

The as-sintered rods are then put into floating zone furnace for single crystal growth as feed and seed rods. The whole growth process is done under 1 bar argon atmosphere, with velocity 7 mm/h, two snapshots of the crystal growth and the crystal are shown in Fig. 4.1. Due to the structural transition around 800°C in the phase diagram of $Sr_2Fe_2O_5$ and the similarity of the unit cell a and c parameters, the single crystal is twinned along a and c directions.

Polarized light microscopy is used to further characterize the quality of the crystal. Through the polarized light, the different orientations of the twinned domains within the crystal would generate contrast colors due to the different index of refraction of the twinned domains for different polarizations , as shown in the Fig. 4.2. We can see that the crystal has strong twinning in the μm range. The Laue pattern also show the twinning of the crystal arising from the similar a and c cell parameters.

4.2. Nuclear Structure of $Sr_2Fe_2O_5$

In the phase diagram of $SrFeO_{3-x}$, the oxygen-deficient end member $Sr_2Fe_2O_5$ has an orthorhombic oxygen-vacancy-ordered brownmillerite type structure [63]. $Sr_2Fe_2O_5$ possesses an $\sqrt{2}a_p \times 4a_p \times \sqrt{2}a_p$ supercell in comparison with the cubic perovskite. The unit cell consists of alternating layers of FeO_6 octahedra and FeO_4 tetrahedra along the b-axis, whereas oxygen

(a) Single crystal growth of $Sr_2Fe_2O_5$

(b) $Sr_2Fe_2O_5$ single crystal
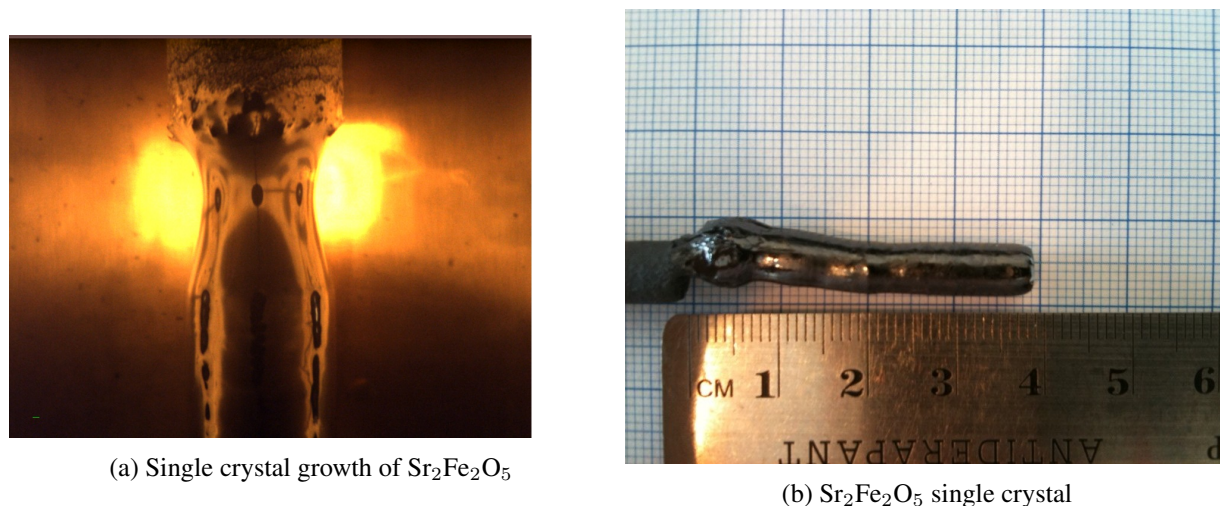
Figure 4.1.: Two snapshots of the single crystal
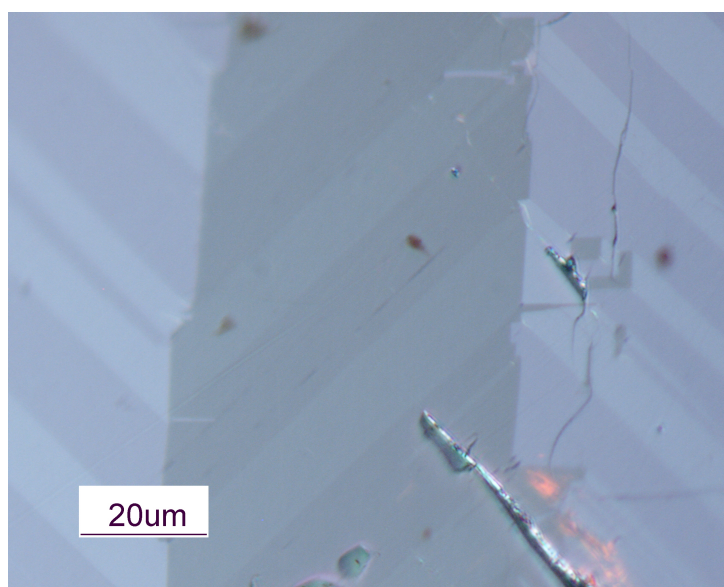
Figure 4.2.: Polarized Optical Microscopy photo of $Sr_2Fe_2O_5$ crystal

vacancies are ordered in the [101] direction forming 1D channels at room temperature. There is a debate about the exact space group of $Sr_2Fe_2O_5$ arising from the ordered or disordered alternating tetrahedral layers. At the atomic position (0,0,0) in the octahedral cation site, if the point symmetry is $\bar{1}$, the space group is Pnma; if the point symmetry is 2, the space group belongs to I2mb [64]. Hence, the tetrahedral (at y=0.25) are related to the other tetrahedral (at y=0.75) through the symmetry operations at the octahedral cation site. They are normally called adjacent T and T/ of FeO_4 layers, respectively . The irregular occurrence of a $\bar{1}$, rather than a 2 point symmetry, causes the crystal structure to be finally given by a higher symmetry space group Icmm [13, 64]. When the temperature reaches above 1000 K, the structure changes into cubic symmetry with the oxygen vacancies in a disordered state. It is considered as the first example of an ordering-disordering transition in AMO_{3-y} perovskite-type compounds at constant

defect concentration $y = 0.5$ [64]. The detailed structure analysis is still under discussion in the literature [13, 64]. In the regions where the point symmetry 2 exists regularly in the structure, the crystal space group is anticipated to be Ibm2[65]. Different synthesis conditions, crystallinity, and stacking faults make the structure of $Sr_2Fe_2O_5$ change. The x-ray diffraction pattern for the single crystal is shown in Fig. 4.3.
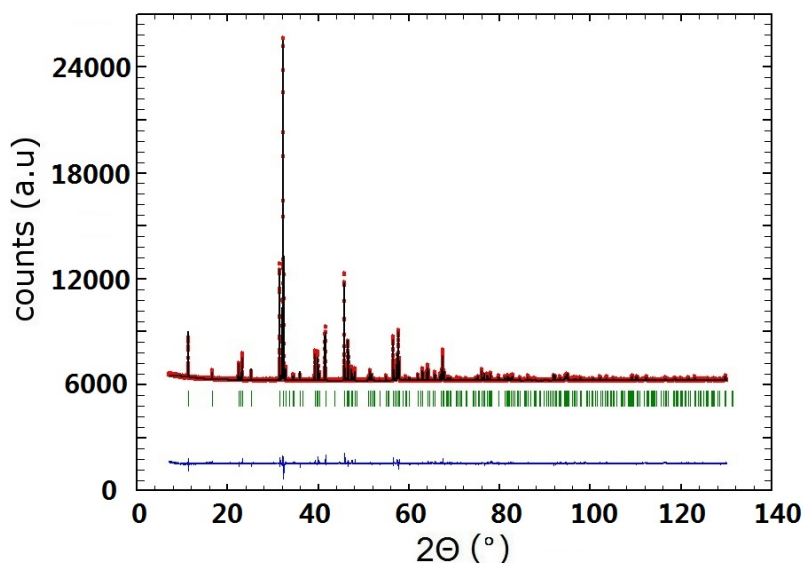
Figure 4.3.: Le Bail refinement of X-ray diffraction pattern of $Sr_2Fe_2O_5$ in Imma space group. Cell parameters : a=5.52783(2)Å,b=15.58292(6)Å,c=5.67325(2)Å,$\alpha = \beta = \gamma = 90°$. Black circles:measured data(I_{obs}); Red line: Calculations (I_{calc}); Blue line:I_{obs}-I_{calc}; Green bars:bragg peak positions.

The phase transition of $Sr_2Fe_2O_5$ has been investigated by differential scanning calorimetry, shown in Figure 4.4. The mass of the measured sample does not change during the heating and cooling procedure, indicating the oxygen stoichiometry staying constant. This is a direct proof that the structure transition is not due to the variation of the oxygen stoichiometry, which is commonly expected in the system of $SrFeO_{3-x}$. No change of the mass certifies also the good stoichiometry of the sample. The exothermic and endothermic change above 800°C are only caused by the structure transition from the ordered phase to the disordered phase, specifically from orthorhombic to cubic symmetry. This observation is in agreement with the previous reports [64, 66]. The structural transition is a first order phase transition. During the floating zone crystal growth, this transition cannot be avoided and results in the twinning of the crystal.

4.3. Mössbauer spectrum of $Sr_2Fe_2O_5$

The Mössbauer spectrum of $Sr_2Fe_2O_5$ at room temperature is shown in Fig 4.5, and the fitting parameters are listed in Table 4.1. The spectrum is composed of two magnetic hyperfine sextets corresponding respectively to the isomer shift 0.37 mm/s and 0.18 mm/s. These values are

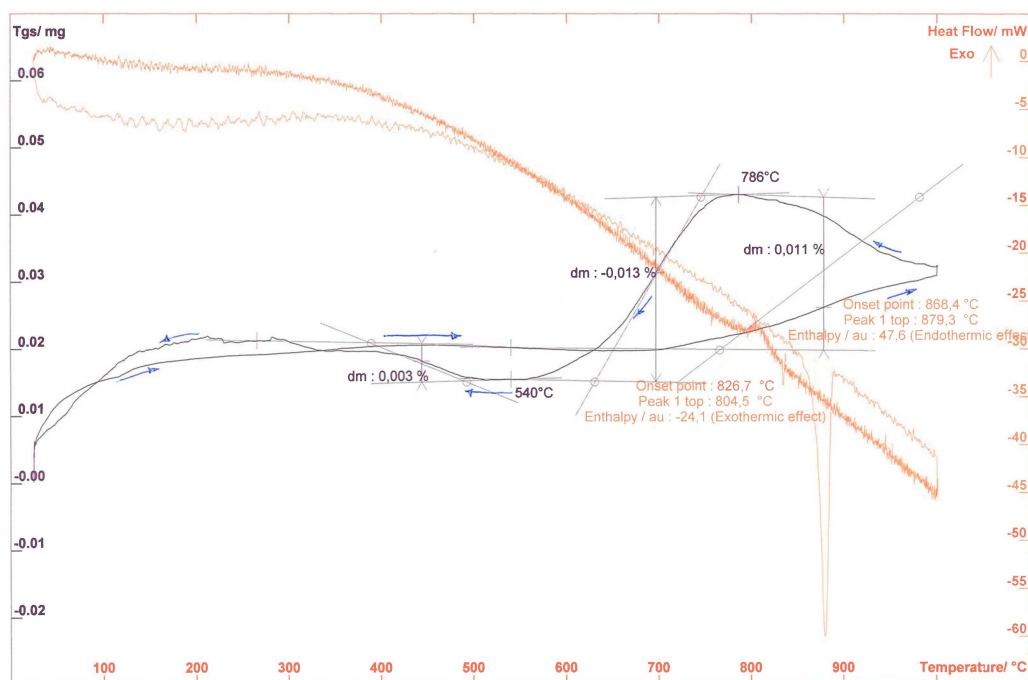Figure 4.4.: DSC combined TGA measurements for $Sr_2Fe_2O_5$ under argon atmosphere with 0.5°C/h cooling rate

characteristic of Fe^{3+} and are assigned to octahedrally and tetrahedrally coordinated Fe^{3+} sites respectively [63]. The magnetic hyperfine splitting observed for both Fe^{3+} sites is in accordance with the fact that $Sr_2Fe_2O_5$ is antiferromagnetically ordered at room temperature. The two hyperfine sextets are not symmetrically distributed along the velocity axis, with respect to the center of the pattern. This is clearly observable from the distances between the two outer lines at the left side and at the right side of each sub-spectrum. This indicates the strong quadrupole interaction in $Sr_2Fe_2O_5$. No further signals are seen in the spectrum, proving the good sample quality. The values of the hyperfine fields B_{hf} and quadrupole splitting are in line with the previous reported work[15]. The Fe^{3+} with high spin state has a $3d^5$ electronic configuration where the five $3d$ orbitals are equally occupied. Therefore, there is no valence contribution to the EFG and the quadrupole splitting is only due to a non zero lattice contribution, arising from the distorted lattice sites[55]. The symmetry at the iron site can only be deduced from the lattice contribution to the EFG. The evaluation of the spectrum revealing combined magnetic and quadrupole interaction gives different values of the quadrupole interaction parameter ε for the octahedral site (-0.33mm/s) and for the tetrahedral site (0.28mm/s) respectively. The different signs of ε reflect different signs of the principal component V_{zz} at the two sites. The magnetic hyperfine fields are arising from the isotropic contact field B_c and dipolar interaction B_{dip} as the spherical charge distribution of Fe^{3+} makes the orbital contribution B_{orb} vanishing. Despite of the spherical charge distribution of Fe^{3+}, the distorted crystallographic structure around Fe^{3+} makes the dipolar contribution B_{dip} contribute to the magnetic hyperfine field B_{hf}.
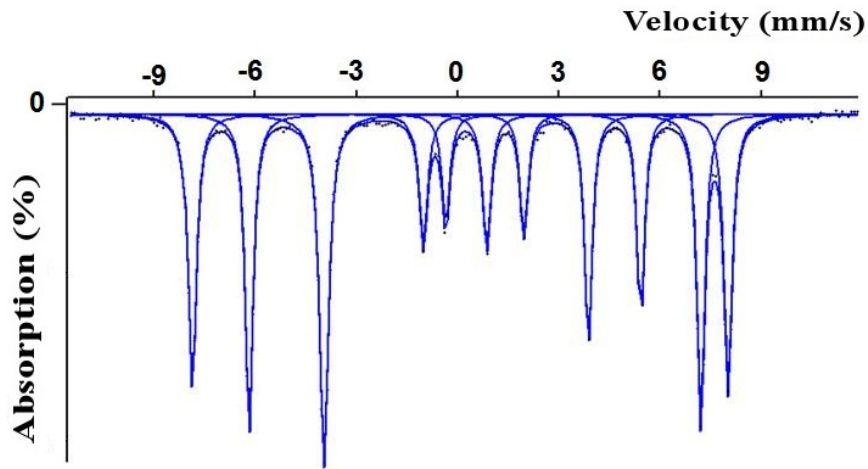
Figure 4.5.: Mössbauer spectrum of $Sr_2Fe_2O_5$ single crystal at room temperature

Site	δ(mm s^{-1})	ε(mm s^{-1})	B_{hf}	%
1	0.37	-0.33	49.5	48 (Octa)
2	0.18	0.28	41.3	52 (Tetra)

Table 4.1.: δ is isomer shift,ε is the quadrupole interaction in the magnetically ordered phase, B_{hf} is magnetic hyperfine field .
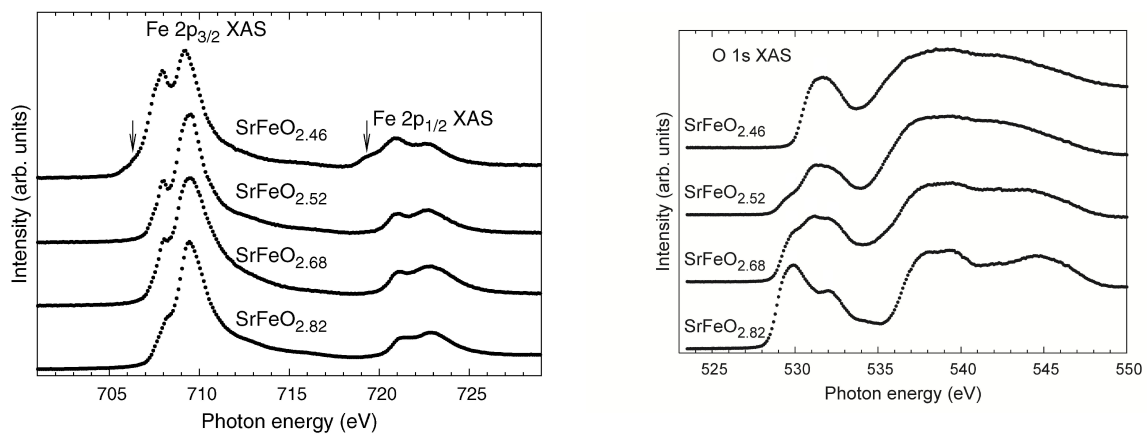
Figure 4.6.: The figures are reproduced from Ref. [67]. The left panel shows the Fe-$L_{2,3}$ edge x-ray absorption spectra of polycrystalline $SrFeO_{2.46}$,$SrFeO_{2.52}$, $SrFeO_{2.68}$ and $SrFeO_{2.82}$. The arrows indicate features formed by Fe^{2+} ions. The right panel depicts oxygen-K edge x-ray absorption spectra of these compounds.
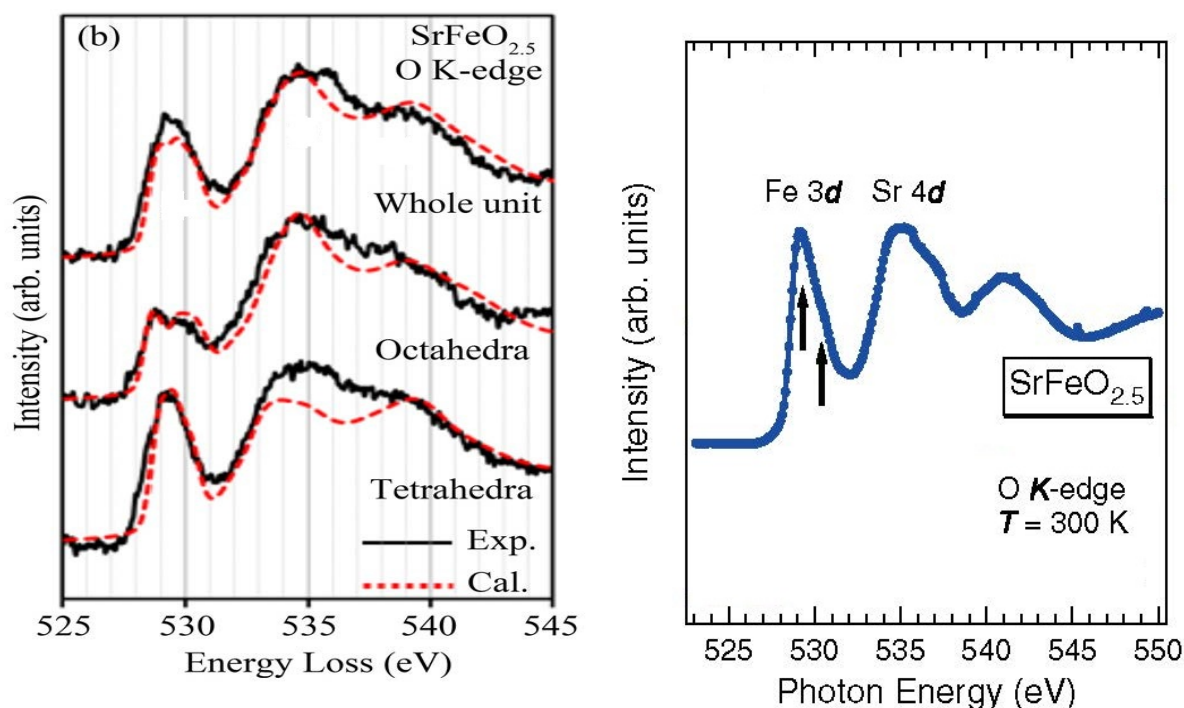
(a) The figure is reproduced from Ref[23]. It shows experimental (blue solid line) and calculated (red dotted line) O K-edge ELNES of $Sr_2Fe_2O_5$ measured over the whole unit cell, and at the individual FeO_6 octahedral and FeO_4 tetrahedral sites.

(b) The figure is partially reproduced from Ref. [21]. It shows the O-K edge x-ray absorption spectra of $Sr_2Fe_2O_5$.

Figure 4.7.: Comparison of literature reported spectra of $Sr_2Fe_2O_5$

4.4. Electronic Structure of $Sr_2Fe_2O_5$

$Sr_2Fe_2O_5$ is an insulator containing formally Fe^{3+} ions coordinated in both octahedral and tetrahedral environment. The electronic structure of $Sr_2Fe_2O_5$ has been studied by several groups using x-ray spectroscopy. Galakhov et al. have investigated the x-ray absorption spectra of Fe $L_{2,3}$ edge and oxygen K- edge on a series of powder samples $SrFeO_{3-x}$ with x=0.54, 0.48, 0.32, and 0.18 [67]. The spectra are reproduced in Fig. 4.6. From the spectra it is concluded that the doped holes are situated both in the Fe $3d$ and O $2p$ states. Later on, Haruta et al. [23] have analyzed the local electronic structure of $Sr_2Fe_2O_5$ on thin film sample using site-resolved energy-loss near-edge structures, see Fig. 4.7a. They confirm that the crystal field at the octahedral site is stronger than at the tetrahedral site. The covalent character of the Fe-O bonds is however stronger at the tetrahedral site in comparison to the octahedral site due to the oxygen atom linked with tetrahedral Fe atom and octahedral Fe atom together having larger charge transfer to the tetrahedral Fe than the octahedral one. This is a reason for the different bond length of Fe-O between the two sites. Very recently, Chikamatsu et al.[21] have studied the electronic structure of $SrFeO_2$ on thin film samples and used $Sr_2Fe_2O_5$ thin film sample as reference, see Fig. 4.7b. Even though it is marked with two arrows in the pre-edge peak region(527-532eV), explained as t_{2g}-e_g orbital splitting, the splitting in the spectrum is actually quite vague.

Comparing the O K-edge spectra in Figs. 4.6-4.7b, it can be seen that the fine structure of the

feature around 530 eV, which corresponds to the hybridized Fe $3d$ and O $2p$ states, is different in the three publications. This could be caused by the difference in oxygen stoichiometry in the powder bulk samples and the thin film samples. No clearly splitting is observable in this feature in all of the spectra, although it is predicted from the calculated density of states [23]. This might also be caused by low resolution in the spectra. To get a more accurate representation of the electronic structure in spectroscopy and also to understand the different coordination of the iron site effects, we have performed x-ray absorption spectroscopy on the Fe-$L_{2,3}$ and O-K edge on our single crystals of Sr$_2$Fe$_2$O$_5$.
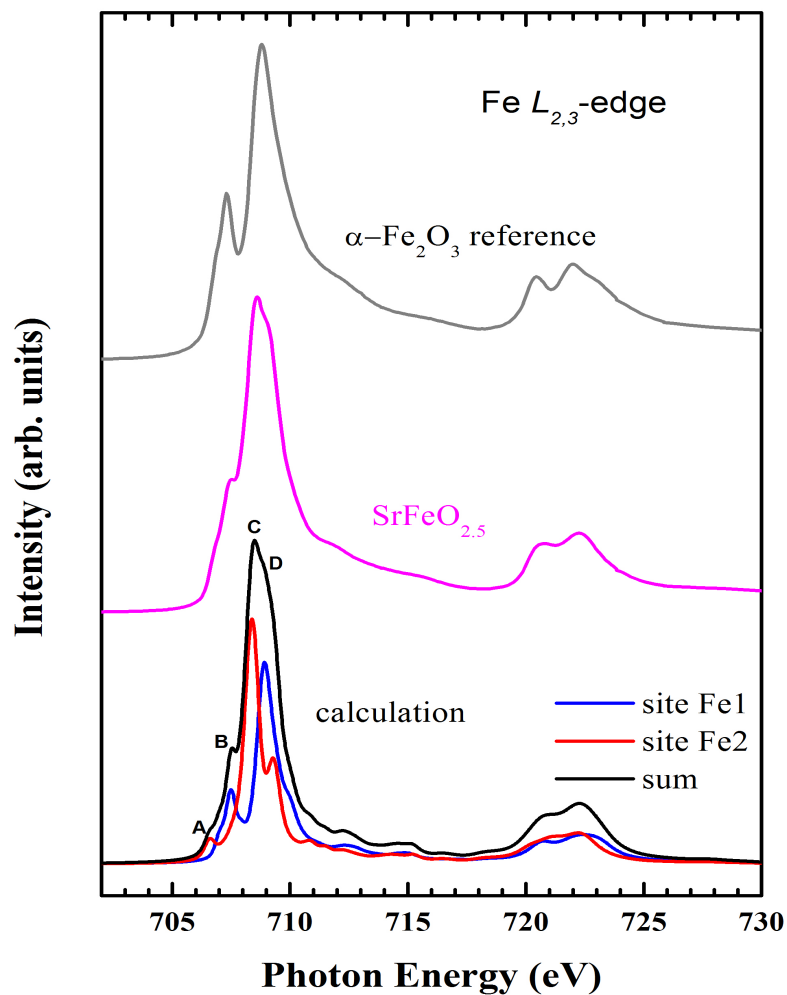
Figure 4.8.: Comparison of Fe$_2$O$_3$ (grey), Sr$_2$Fe$_2$O$_5$(magenta) and theoretical simulation (sum is black,blue is for octahedral Fe1 and red is for tetrahedral Fe2)

In Fig. 4.8 we show the Fe-$L_{2,3}$ edge XAS of the Sr$_2$Fe$_2$O$_5$ single crystals, along with a

Fe_2O_3 reference. The experimental line shape shows slight differences to the one found for polycrystalline sample $SrFeO_{2.52}$, see the left panel in Fig. 4.6, which can be partly attributed to an improved resolution in our measurements. From comparison to the reference spectrum of Fe_2O_3, we can clearly see that the charge state of Fe in the $Sr_2Fe_2O_5$ single crystals is Fe^{3+}. There is a splitting of the L_3 main feature at around 709 eV into two features labeled C and D, in combination with two prepeak features A and B. The splitting of the main feature is likely a result of the difference in on-site energies of the two Fe sites.

To prove this conjecture, we have performed full-multiplet cluster calculations to model the spectral line shape of the Fe-$L_{2,3}$ edge. The XTLS 9.0 code has been used [61] to calculate the spectra for the two iron sites which are added incoherently. The slater integrals are estimated from Hartree-Fock values that are reduced to 80%. As parameters, $U_{dd} = 6.0$ eV, $U_{cd} = 7.5$ eV, and $\Delta = 2.0$ eV have been used. The symmetry of each site has been approximated as cubic, and the hybridization is estimated from Harrison's book [68] using the average Fe-O bond length. For tetrahedral site, the bond length is 1.877Å and $V_{pd\sigma}$=-1.774 eV. For octahedral site, the bond length is 2.062Å and $V_{pd\sigma}$=-1.2787 eV. As ionic crystal field, $10Dq = 0.7$ eV and -0.4 eV are used for the octahedral and tetrahedral Fe sites, respectively. The result of the calculation is shown on the bottom of Fig. 4.8. It reproduces the experimental result well, and it can be seen that indeed features A and C are caused by the tetrahedral site (Fe2), while features B and D originate from the octahedral site (Fe1). The agreement between experiment and calculation also
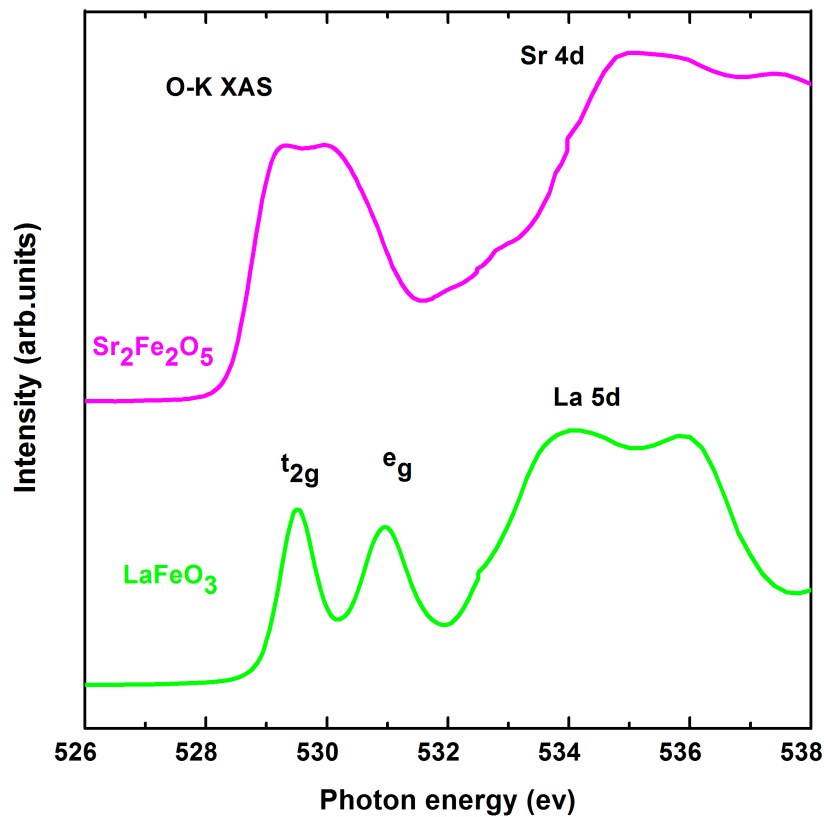
Figure 4.9.: Oxygen K-edge of $Sr_2Fe_2O_5$

shows that there is no sign of another Fe valence in the spectrum, proving the correct oxygen stoichiometry.

The oxygen K-edge XAS spectra of $Sr_2Fe_2O_5$ is shown in Figure 4.9, together with a comparison of $LaFeO_3$ oxygen K-edge XAS. A splitting in the prepeak, which is corresponding to the hybridzation of Fe and O, is clearly observed. The spectrum is in qualitative agreement with the data recorded on thin films in Fig. 4.7b with better resolution. Comparing with $LaFeO_3$ oxygen K-edge, the broad feature at 534.9eV in $Sr_2Fe_2O_5$ is indicative of Sr $4d$ related band while a broad feature at 533.8eV in $LaFeO_3$ correspond to La $5d$. Notice that the prepeak features between 528eV $\sim$ 532eV are quite different between $LaFeO_3$ and $Sr_2Fe_2O_5$. In $LaFeO_3$, which has pure Fe^{3+} in octahedral coordination, the splitting of the prepeak at 529.5eV and 531eV can be associated with the separation between t_{2g} and e_g states, respectively. However, in $Sr_2Fe_2O_5$ the Fe^{3+} situated in octahedral and tetrahedral sites equally, the oxygen K-edge spectrum shows a result of mixed octahedral and tetrahedral crystal fields, which is also proposed in Reference[21].

4.5. Conclusion

Good quality single crystal of $Sr_2Fe_2O_5$ have been prepared and checked by x-ray diffraction and Mössbauer spectroscopy. Well resolved x-ray absorption spectra have been taken on Fe $L_{2,3}$ edge and oxygen K-edge. Full-multiplet cluster calculations have illustrated the different coordinations of the Fe^{3+} contribution to the spectra.

Chapter 5.

Synthesis and characterization of $Sr_4Fe_4O_{11}$

5.1. Synthesis powder and single crystal of $Sr_4Fe_4O_{11}$

Solid state reaction had been used for synthesizing $Sr_4Fe_4O_{11}$ polycrystalline. $SrCO_3$ (Alfa Aesar Ref:012593) and Fe_2O_3 (Sterm Chemicals Ref:933803) with the purity of 99.9% and 99.99% respectively were used as the starting reactant. The $SrCO_3$ was preheated under 523K for 10h to remove the absorbed water, then the mass was weighted directly according to the stoichiometry. The weighted mass of $SrCO_3$ and Fe_2O_3 were calculated according to the molar ratio 1:1. The reactants were then mixed with ethanol in order to get better intermixture. After drying in ambient atmosphere, the mixture was first preheated under air at 1173K for one night and then ground again, sintered at 1473K for another 48h with intermediate grinding. Based on the different cooling rate, the final products had different oxygen stoichiometry. Here list examples of the batches prepared with the different cooling rate.

The different preparation processes for the three batches of the sample $SrFeO_{3-x}$ are listed in Table 5.1

LQ12R	heated at 1340°C for 60h and cooled down with a rate of 200°C/h
LQ22R	heated at 1150°C for 55h and cooled down with a rate of 180°C/h
LQS11	heated at 1200°C for 60h and cooled down with a rate of 60°C/h to 800°C for 1h and then with a rate of 30°C/h to 200°C

Table 5.1.: Different synthetic routes for the three different batches of the sample $SrFeO_{3-x}$

Owing to the different cooling rate, the three samples had different crystallographic structure. Two of them(LQ12R,LQ22R), preparing by fast cooling rate, were mixture of the two phases : $Sr_4Fe_4O_{11}$ (S.G.Cmmm) and $Sr_8Fe_8O_{23}$ (S.G.I4/mmm). The only one (LQS11) was pure phase $Sr_4Fe_4O_{11}$ (S.G.Cmmm), prepared with slow cooling rate. Their X-ray diffraction pattern, refined by full pattern matching have been listed in Table 5.2 and Fig 5.1

Cell Parameter	LQ12R		LQ22R		LQS11	
	Sr4Fe4O11	Sr8Fe8O23	Sr4Fe4O11	Sr8Fe8O23	Sr4Fe4O11	Sr8Fe8O23
a(Å)	10.8932(2)	10.8992(3)	10.96750(5)	10.92680(4)	10.9359(3)	-
b(Å)	7.6871(1)	10.8992(3)	7.69656(2)	10.92680(4)	7.7035(1)	-
c(Å)	5.46053(9)	7.6686(2)	5.46560(2)	7.69494(5)	5.4719(1)	-

Table 5.2.: Structure parameters of the three different batches of the sample $SrFeO_{3-x}$

There are several possible factors that may influence the oxygen stoichiometry and consequently influence the structure: 1. The equilibrium of the oxygen content between the air and the

(a) LQ12R

(b) LQ22R

(c) LQS11
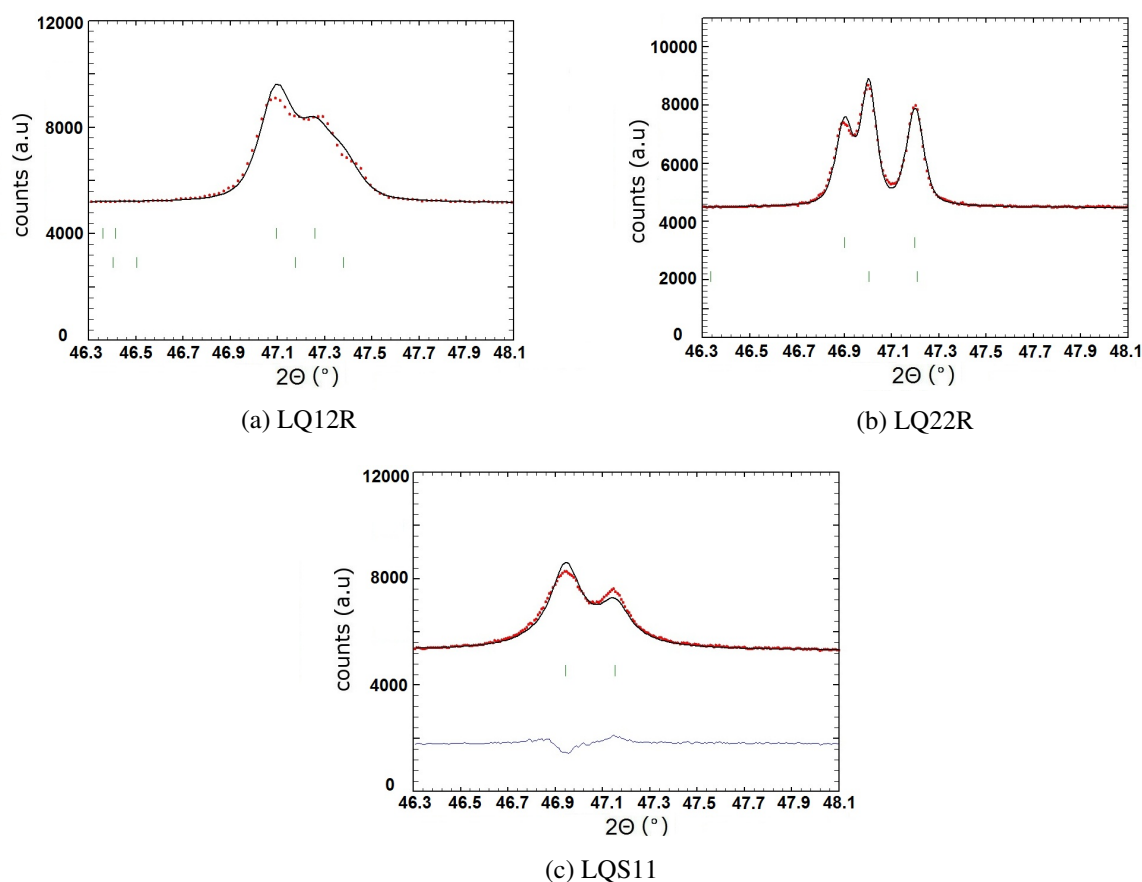
Figure 5.1.: X-ray Diffraction pattern of the different batches. Red circles: measured data I_{obs}; Green bars: peak positions of the nuclear peaks; Black lines: Rietveld fit (I_{calc}); Blue lines: I_{obs}-I_{calc}

sample can only be reached with slow cooling rate[69]. 2. The stacking fault that may form in the packing of oct/pyra layers also attributed to the full width half maximum of the peak[64]. Cooling rate of 1K/h in air has been tested during the whole cooling process, the final product has the chemical formulae $SrFeO_{2.81}$ (Determined by titration and Thermogravimetric analysis). This is in accordance with the other works, see Reference [11, 70]. In order to prepare the high quality sample with the oxygen stoichiometry close to $Sr_4Fe_4O_{11}$, quenching has been chosen at the end of the reaction. Two batches of sample have been sintered in the air at 617°C. One batch has been sintered for one week , another batch has been sintered for two weeks. Both of them are all quenched in the air. Surprisingly, even though the two batches are all kept in the same furnace and the same speed of air flow, they have different structure patterns and physical properties, which will be presented in the following sections.

Single crystal $SrFeO_{3-X}$ has been prepared in the floating zone furnace by Dr.Alexander Komarek. The Laue pattern shows that the crystal is twinned along a and c axis, see Fig 5.2. Due to the thermal gradient which is not avoidable in the crystal growth of the floating zone technique, the oxygen stoichiometry slightly changes from the (cold) lower end to the (hot) upper end of the as-grown single crystal. Therefore, the crystal has been carefully checked and cut based on the results of the chemical titration and magnetization measurement, which are two of

the important ways in this thesis to determine the oxygen stoichiometry. And the best part close to the idealistic oxygen stoichiometry $Sr_4Fe_4O_{11}$ is used for the X-ray absorption, photoemission and single crystal neutron diffraction measurement.

(a) a or c axis   (b) b axis
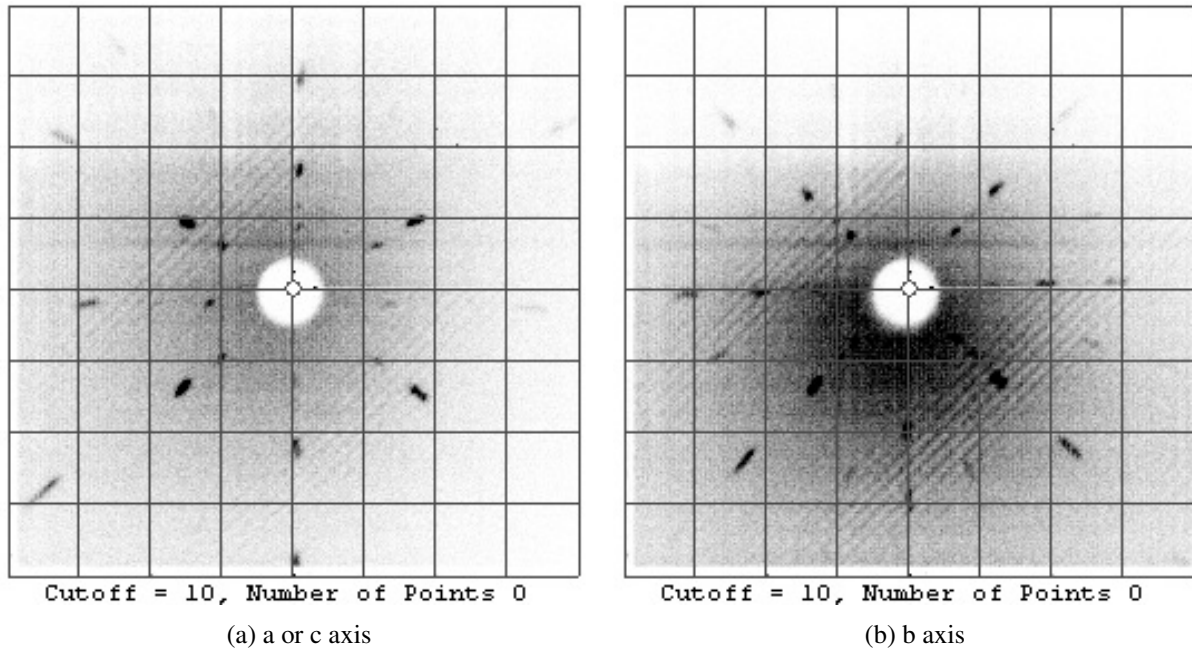
Figure 5.2.: Laue pattern of the crystal $Sr_4Fe_4O_{11}$

5.2. Control the Oxygen stoichiometry

As already mentioned, the oxygen stoichiometry is crucial not only for the structure but also for the physical properties of this series $SrFeO_{3-x}$. In order to precisely determine the oxygen stoichiometry of the as-sintered sample $SrFeO_{3-x}$, the thermogravimetric analysis (TGA) and chemical titration have been used.

The TGA has been performed under 1-atm Ar flow mixed with 5% H_2 flow and heat up to 560°C for 12h, and the final reduced product is $Sr_2Fe_2O_5$. The titration has been performed using modified Mohr Salt method, which is listed in the appendix. There are unavoidable errors for both methods, especially $SrFeO_{3-x}$ can absorb carbon dioxide in the air, if the sample has been kept for long time in the air, and thus gives an error in TGA measurement. An example has been shown in Fig. 5.3, where the main weight loss coming from the reduction of the oxygen, but the carbon dioxide has been released around 400°C and 680°C and contributes some amount of the weight loss. This leads to the final calculation of the oxygen stoichiometry equals to $SrFeO_{2.9}$. However, the result of the chemical titration, for the same batch of the sample, gives oxygen stoichiometry $SrFeO_{2.81}$. Such a big discrepancy, arising from the absorbed carbon dioxide, is mainly due to several days exposition into the air. This will influence the TGA measurement more directly than the titration. Previous study on the difference of the results of these two techniques is approximately $\mid X_{chem\cdot anal}$ - $X_{TG} \mid \leq 0.03$ (X is the oxygen vacancy in $SrFeO_{3-x}$), which is also shown in our other results of the as-sintered samples.

Figure 5.3.: The TGA measurement combined with the Mass spectrometry.The black line is the weight loss of the original compound $SrFeO_{3-x}$. The green line corresponds to oxygen detected from the Mass spectrometry and the blue line corresponds to carbon dioxide detected from the Mass spectrometry

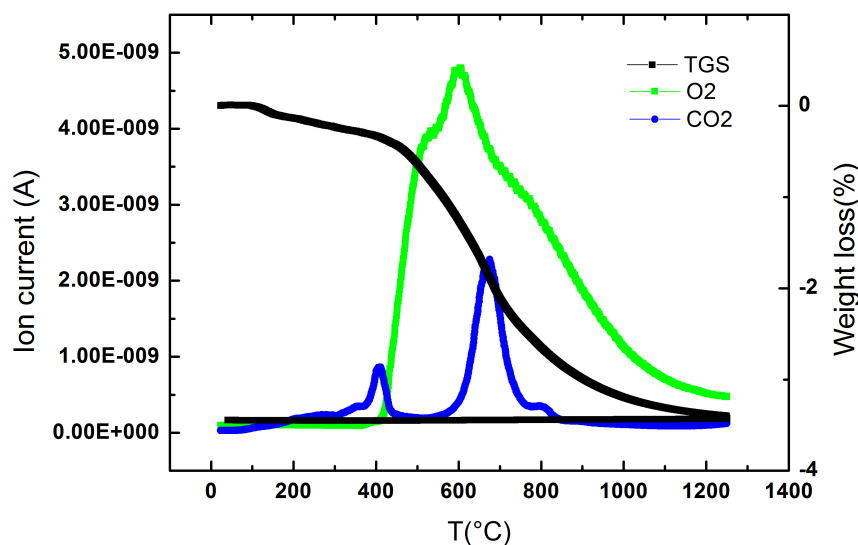## 5.3. Nuclear Structure of $Sr_4Fe_4O_{11}$

There are two other stable phases in the phase diagram of $SrFeO_{3-x}$, existing between the fully oxidized phase $SrFeO_3$ and the fully reduced phase $SrFeO_{2.5}$, namely the $Sr_8Fe_8O_{23}$ ($SrFeO_{2.875}$) and the $Sr_4Fe_4O_{11}$ ($SrFeO_{2.75}$). $Sr_8Fe_8O_{23}$ has a tetragonal unit cell $2\sqrt{2}a_p \times 2\sqrt{2}a_p \times 2a_p$. The general structure has been show in Fig 5.5c, and it involves three different types of iron sites Fe1, Fe2 and Fe3 with a relative abundance of 1:2:1. The Fe1 site is in an approximate square pyramidal environment of oxygen atoms, whereas the Fe2 and Fe3 sites are six-fold coordinated. The Fe1O square pyramids form dimers via the O1 atom. The nearly regular Fe3O6 octahedra form rows along the c direction and each of these rows is surrounded by four columns of Fe2O6 units. This distorted Fe2O6 octahedral are further connected to Fe1O pyramids.

   For $Sr_4Fe_4O_{11}$, it has orthorhombic structure $2\sqrt{2}a_p \times 2a_p \times \sqrt{2}a_p$($a_p$ donate the unit-cell edge of the perovskite subcell), where dimers of Fe1O5 units are formed. These dimers are connected to rows of strongly distorted Fe2O6 octahedra. J.P.Hodges has investigated its crystal structure by the time of flight neutron powder diffraction and confirms the crystal structure should be Cmmm instead of C12/m1. The validity of the structure model is further proved by analyzing the distribution of Fe-O bond lengths and O-O distances. Actually the bond-length distribution and bond-strength sum calculation are important tools to confirm the crystal structure. For $Sr_4Fe_4O_{11}$ and $Sr_8Fe_8O_{23}$ there are several plausible space groups and the agreement factors of the refinement are close. By comparing the bond length of the structure, one can clearly notice the unreasonable short bond length and therefore exclude the correspondent space group. Through this way, the space group Cmmm for $Sr_4Fe_4O_{11}$ and I4/mmm for $Sr_8Fe_8O_{23}$ are chosen. One can consider the evolution of $Sr_4Fe_4O_{11}$ into $Sr_8Fe_8O_{23}$ as the $[001]_p$ lines of $(FeO_5)_2$

bow-tie units has been fulfilled with oxygen every other two .

$Sr_8Fe_8O_{23}$ has a Verwey-like transition around 70K, where a combined charge-magnetic ordering phenomenon was observed together with a metal-insulator transition[2]. However, for $Sr_4Fe_4O_{11}$, the Verwey-like transition is absent below room temperature. The crystal structure reveals crystallographic ordering at room temperature with chains of octahedral sites cross linked by dimers of pyramidal sites and charge ordering, equal amount of Fe^{4+} and Fe^{3+} as confirmed by the Mössbauer spectrum. The allocation of the charge to the two crystallographic sites are still an open question. In this thesis, the mainly focused phase is $Sr_4Fe_4O_{11}$ and its structure refinement is listed below.
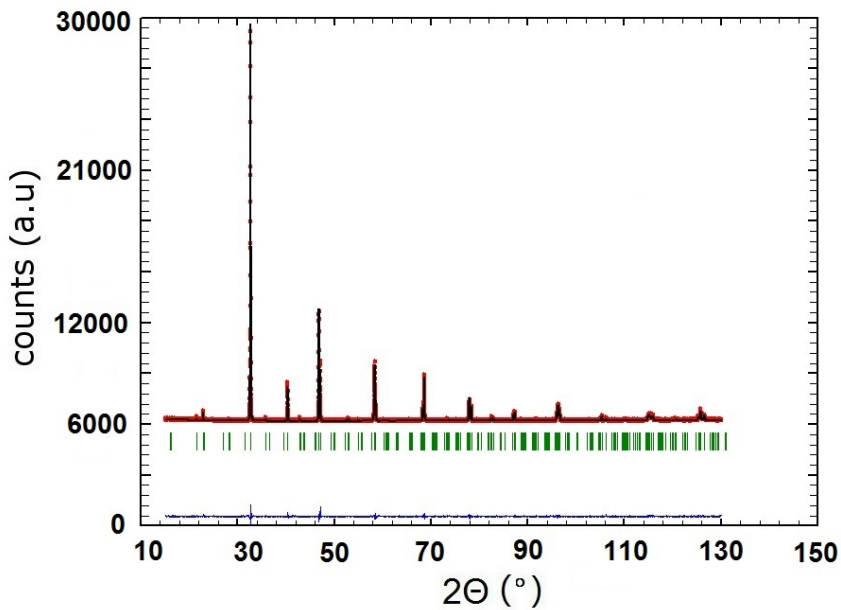
Figure 5.4.: Rietveld refinement of $Sr_4Fe_4O_{11}$ in Cmmm space group, a=10.97293 (6)Å, b=7.70502(4)Å, c=5.47178(3)Å, $\alpha = \beta = \gamma = 90°$. Wavelength: CuK$\alpha$1=1.54056Å. R-Bragg factor =4.04, R$_f$ factor = 6.18. Red circles: measured data I$_{obs}$; Green bars: peak positions of the nuclear peaks; Black lines: Rietveld fit (I$_{calc}$); Blue lines: I$_{obs}$-I$_{calc}$

Cell Parameter	x	y	z	Occ
Sr1	0.50000	0.00000	0.50000	0.125
Sr2	0.00000	0.00000	0.50000	0.125
Sr3	0.25819(19)	0.00000	0.00000	0.250
Fe1	0.50000	0.24773(49)	0.00000	0.250
Fe2	0.25000	0.25000	0.50000	0.250
O1	0.50000	0.00000	0.00000	0.125
O2	0.27141(115)	0.00000	0.50000	0.250
O3	0.37468(62)	0.27420(45)	0.77255(113)	1.000

Table 5.3.: Structure parameters of $Sr_4Fe_4O_{11}$ pure phase in this thesis

(a) $SrFeO_3$

(b) $Sr_8Fe_8O_{23}$

(c) $Sr_4Fe_4O_{11}$
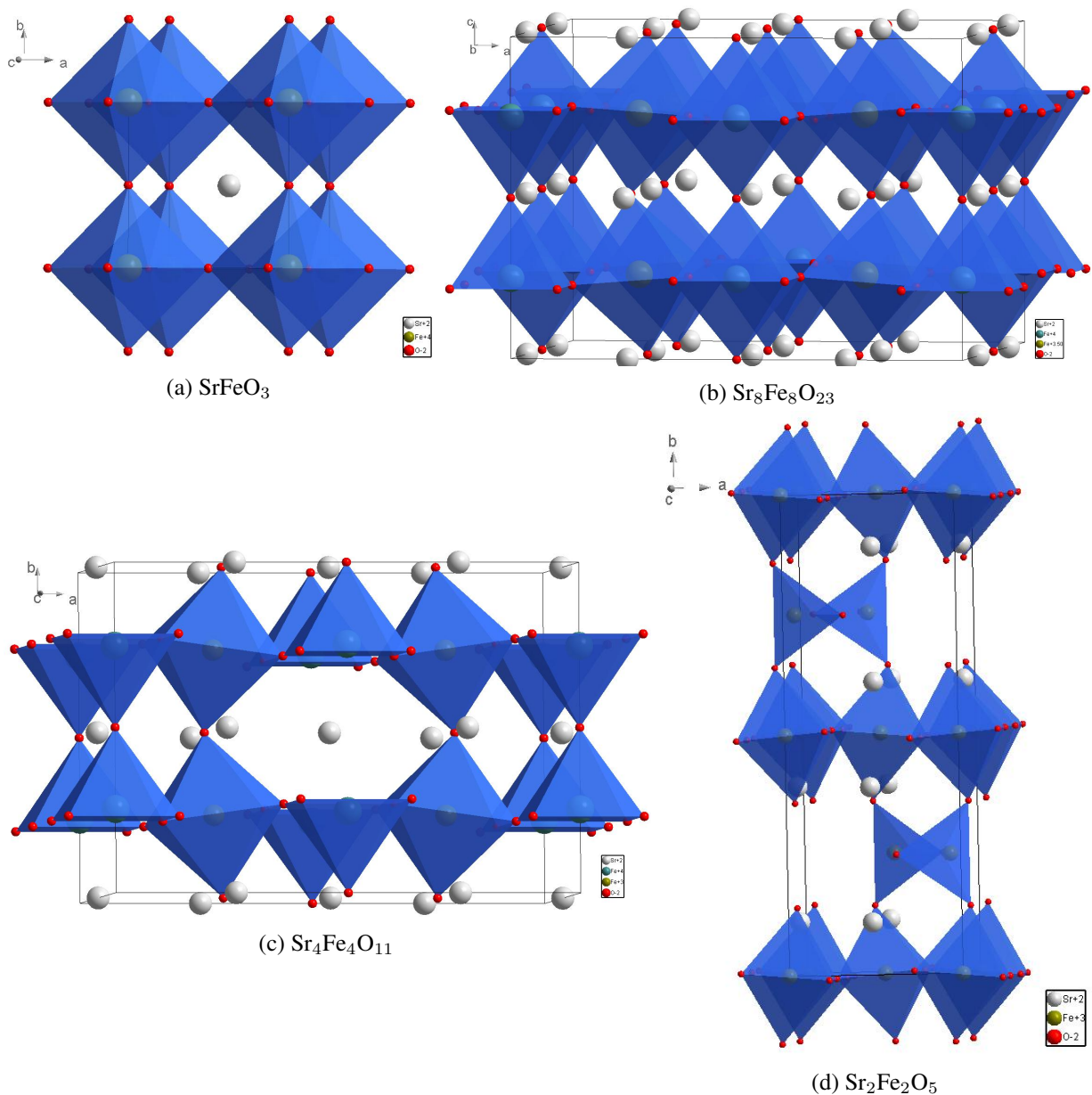
(d) $Sr_2Fe_2O_5$

Figure 5.5.: The structure of $Sr_2Fe_2O_5$, $Sr_4Fe_4O_{11}$, $Sr_8Fe_8O_{23}$ and $SrFeO_3$

The extremely sensitivity of the structure to the oxygen stoichiometry has indeed been observed during the synthesis and structure analysis. We compare here two batches of sample. The only difference of these two through the whole synthetic route is the annealing time. As already mentioned in Section 5.1, one batch has been sintered at $617°C$ for one week , another batch has been sintered at the same temperature for two weeks. Then both samples are quenched into the air. The structure refinement show clearly differences between these two batches, see in Fig 5.6. A small hump ($2\theta = 46.96°$), existing between the Bragg peaks of $Sr_4Fe_4O_{11}$, belongs to the phase $Sr_8Fe_8O_{23}$ in the one week annealing sample; While only pure $Sr_4Fe_4O_{11}$ phase exists in the two weeks annealing sample within the experimental error.

This difference in the structure directly influences the physical properties, which will be
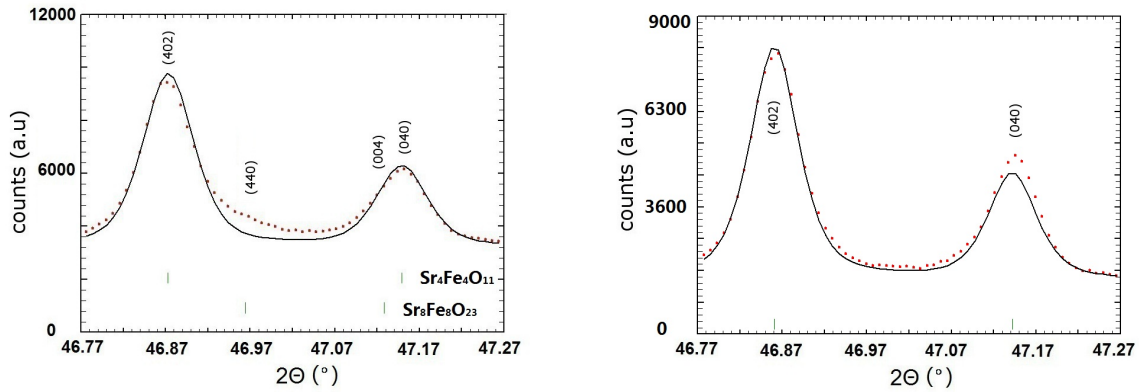
(a) One week annealing sample $SrFeO_{3-x}$ contains two phases $Sr_8Fe_8O_{23}$, $Sr_4Fe_4O_{11}$

(b) Two weeks annealing sample $SrFeO_{3-x}$ contains only one phase

Figure 5.6.: The influence of the annealing time to the structure and oxygen stoichiometry. Red circles: measured data I_{obs}; Green bars: the nuclear peak positions; Black lines: Rietveld fit (I_{calc}).

presented in the next chapter.

5.4. Magnetic Structure of $Sr_4Fe_4O_{11}$ and its symmetry

5.4.1. Background

Neutron powder diffraction[14] has observed the compression of the octahedral sites (Fe(2)) in $Sr_4Fe_4O_{11}$ as the temperature goes down to 1.5K. It is explained by the Jahn-Teller distortion of Fe^{4+} in Fe(2) site. Meanwhile, the iron atom Fe(1) inside the pyramidal site moves away from the base of the pyramid. No structural transition is observed from 1.5K to 300K. And the low temperature neutron pattern can be fitted within two magnetic space groups Cm$'$m$'$m$'$ and Cmm$'$m$'$, see Fig 5.7. In Cm$'$m$'$m$'$ model, the magnetic moments of Fe(1) in pyramid sites are aligned along the [010] direction antiferromagnetically. But in Cmm$'$m$'$ space group, the magnetic moments are permitted on both Fe(1) and Fe(2) sites. However, by combining with the Mössbauer spectra results, which show only one iron site has magnetic moment, Schmidt defined the magnetic moment along the b axis only seated in the Fe(2) site in Cmm$'$m$'$ space group.

Regarding the sublattices of the Fe(1) and Fe(2) atoms are almost identical in the structure , the Rietveld refinement of the neutron powder diffraction alone is not possible to finally determine the correct magnetic space group. The charge ordering of Fe^{3+} and Fe^{4+} to the two crystallographic sites will provide important information for the magnetic ordering. Based on the two listed reasons: 1. The appearance of pyramidal sites is always associated with the lowering of the average Fe valence below Fe^{4+}. There exists only Fe^{3+} in pure pyramidal site compound in the nature ($Sr_3Fe_2O_6$). 2. The compression of the octahedral site can be seen as the expected Jahn-Teller effect of Fe^{4+} . Thus the allocation of the different iron valence is the Fe^{3+} sits in pyramidal site (Fe(1)) and Fe^{4+} sits in octahedral site (Fe(2)) and the Cm$'$m$'$m$'$ magnetic model has been chosen .
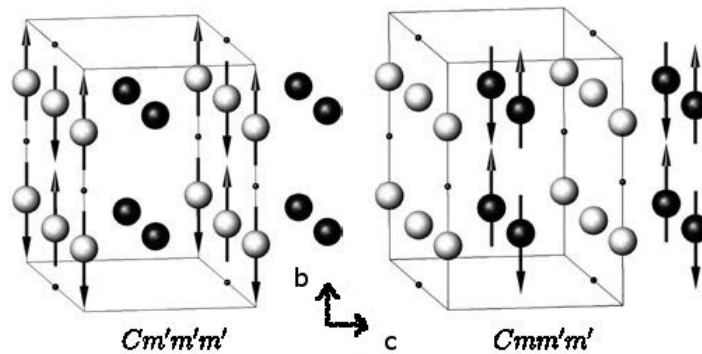
Figure 5.7.: The picture is directly reproduced from [14]. Two magnetic models of the $Sr_4Fe_4O_{11}$ magnetic structure. The grey and black spheres represent the Fe(1) and Fe(2) atoms respectively.

Later on, the theoretical study, using spin-polarized electronic-structure total-energy calculation[16], has proposed another magnetic structure, where $Sr_4Fe_4O_{11}$ can be considered as a phase-separated system with one phase in the G-type antiferromagnetic state as the magnetic ground state and the other in a spin-glass-like state, see Fig 5.8.
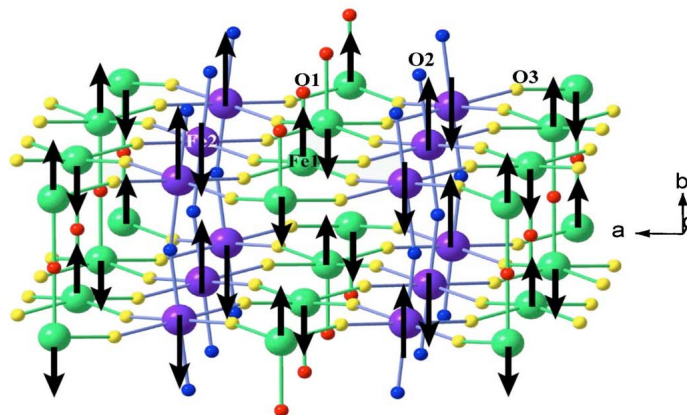
Figure 5.8.: The picture is directly reproduced from [16]. The schematic ground-state magnetic structure for $Sr_4Fe_4O_{11}$ obtained from the spin-polarized total energy calculations. The longer arrow corresponds to a moment of 3.52 μ_B at the Fe(2)^o site and the smaller arrow reflects a moment of 2.83 μ_B at the Fe(1)^s site.

The magnetization measurement shows the offset of the magnetization loops from the origin, see Fig 5.9. This phenomenon is explained as exchange bias like effect which commence at Néel temperature. The author assume the Fe(2) moments involved in this exchange bias like effect as they are antiferromagnetically ordered below Néel temperature and the spins of Fe(1) moment are frustrated and form a spin glass arising below 50K[71].

Recently, another work[72] on neutron single crystal of $SrFeO_{3-x}$(x=0.0,0.03,0.13 and 0.23) have found some new magnetic phase transition, listed in Fig 5.10. Three new magnetic phases (Phase IV, V and VI) have been observed at different magnetic transition temperature. Phase IV (the transition temperature T_N=65K) has propagation vector k=(0,0,1/2) and the spin tilted with respect to the c axis with an angle of 54(1)°. The other two new magnetic phases (V and
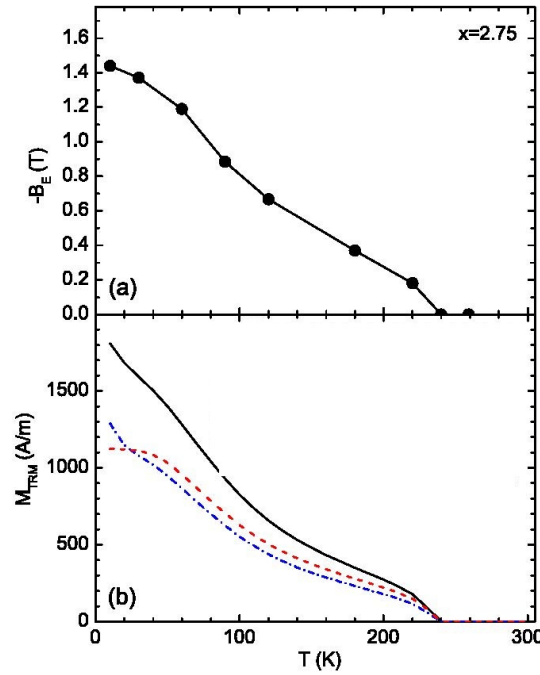
Figure 5.9.: The figure is directly reproduced from reference[71] (a)Plot of the exchange-bias-like field B_E against temperature after cooling in a field of 6T. (b) Plot of the thermoremnant magnetization M_{TRM} after field cooling to 10K in a field of 5T and then turning the field off, for x=2.80(dot-dashed curve), x=2.75(solid curve), and x=2.72(dashed curve). Inset:Plot of M_{TRM} at 10K against time after cooling in a field of 5T and then turning the field off. The solid curve is a stretched exponential fit to the data. 81, 2.80, 2.75, and 2.72. Inset: Plot of the offset field B_E against the oxygen content x.

VI) can not be determined due to the weakness of the observed reflections, which appear at new magnetic transition temperatures. All these new magnetic phases can not be solved by any magnetic structure because of the mixed phases of the single crystals and the superstructure reflections of the minority phases are rather weak.

Magnetic phase	Propagation vector k	Type of spin order	T_N (K)	Samples	Crystal structure
Phase I	$(0.13, 0.13, 0.13)_{cub}$	Helical	133(1), 134	$SrFeO_{2.87-3.00}$ (crystal)	$SrFeO_3$
Phase II	$(0.20, 0.20, 0.20)_{cub}$	Helical	75(2)	$SrFeO_{2.87}$ (crystal)	$Sr_8Fe_8O_{23}$
Phase III	$(0.17, 0.17, 0.17)_{cub}$ $(0.687, 0, 0.326)_{mon}$	SDW	75(2)	$SrFeO_{2.87}$ (powder)	$Sr_8Fe_8O_{23}$
Phase IV	$(0, 0, \frac{1}{4})_{cub}$ $(0, 0, \frac{1}{2})_{tetr}$	Canted AF	65(4)	$SrFeO_{2.77-3.00}$ (crystal)	Unknown
Phase V	$(0.30, 0.30, 0.75)_{cub}$	SDW or helical	110(4)	$SrFeO_{2.77}$ (crystal)	Unknown
Phase VI	$(0.79, 0.79, 0)_{cub}$	SDW or helical	60(5)	$SrFeO_{2.77}$ (crystal)	Unknown
Phase VII	0	AF	232(2), 232(4)	$SrFeO_{2.77}$ (crystal)	$Sr_4Fe_4O_{11}$

Figure 5.10.: The table is directly reproduced from reference [72]. Magnetic phases in the system $SrFeO_{3-\delta}$ ($0\le \delta \le 0.25$)found by single-crystal or powder neutron diffraction.In this system the magnetic moments of the iron atoms show commensurate antiferromagnetic (AF), helical, and amplitude-modulated spin-density wave (SDW) structures.)

5.4.2. Structure and its charge ordering

We have reinvestigated the magnetic structure of $Sr_4Fe_4O_{11}$ during the PhD thesis with powder neutron diffraction in D20 and D2B at ILL in Grenoble France from room temperature to low temperature and single crystal neutron diffraction in Trics at PSI in Villigen Switzerland at 120K.

For the measurement in D2B, three different temperatures have been measured with wavelength $\lambda = 1.594216$Å. An initial magnetic structure model Cmmm has been used for indexing the neutron powder diffraction pattern as proposed by J.P.Hodges [13]. Excellent fits between the observed diffraction data and calculated profile are obtained for all the three different temperatures and shown in Fig 5.11, the structure parameters are listed separately in Table 5.4, 5.5, 5.6. Notice that at 10K, the thermal motion of the oxygen O(1) is a small negative value. This can be explained as the thermal parameters become poorly defined and act as a dumping ground for systematic errors when there are a large number of variables during the refinement[73]. Given the fact that the thermal motion of the oxygen should be small at low temperature, we constrain (the thermal motion parameter of O(1) and O(2)) during the refinement and all the occupancies are fixed.

Atom	X	Y	Z	Biso(Å^2)
Sr1	0.5000	0.0000	0.5000	0.329(202)
Sr2	0.0000	0.0000	0.5000	0.153(161)
Sr3	0.2566(6)	0.0000	0.0000	0.353(149)
Fe1	0.5000	0.2467(5)	0.0000	0.133(76)
Fe2	0.2500	0.2500	0.5000	0.152(76)
O1	0.5000	0.0000	0.0000	0.261(64)
O2	0.2691(5)	0.0000	0.5000	0.261(64)
O3	0.3803(4)	0.2750(2)	0.2384(8)	0.512(35)

Table 5.4.: Structure parameters for $Sr_4Fe_4O_{11}$ at 10K from neutron powder diffraction refined in Cmmm space group. a=10.95120(15)Å, b=7.68420(9)Å, c=5.45824(7)Å. $R_{Bragg} = 4.35$, R_f=4.32, Chi2=3.33

Atom	X	Y	Z	Biso(Å^2)
Sr1	0.5000	0.0000	0.5000	0.583(239)
Sr2	0.0000	0.0000	0.5000	0.267(189)
Sr3	0.2568(7)	0.0000	0.0000	0.497(167)
Fe1	0.5000	0.2460(5)	0.0000	0.256(81)
Fe2	0.2500	0.2500	0.5000	0.174(79)
O1	0.5000	0.0000	0.0000	0.333(212)
O2	0.2697(5)	0.0000	0.5000	0.252(141)
O3	0.3798(4)	0.2750(2)	0.2396(9)	0.646(36)

Table 5.5.: Structure parameter for $Sr_4Fe_4O_{11}$ at 150K from neutron powder diffraction refined in Cmmm space group. a=10.95617(15)Å, b=7.68952(9)Å, c=5.46194(7)Å. $R_{Bragg} = 4.48$, R_f=3.83, Chi2=3.14

The schematic picture of the structure of $Sr_4Fe_4O_{11}$ is shown in Fig 5.12. The O(1) atom is shared by the neighbor Fe(1) atoms in pyramidal sites and the O(2) atom is shared by the neighbor Fe(2) atoms in octahedral sites. The O(3) atom works as a bridge link the octahedral
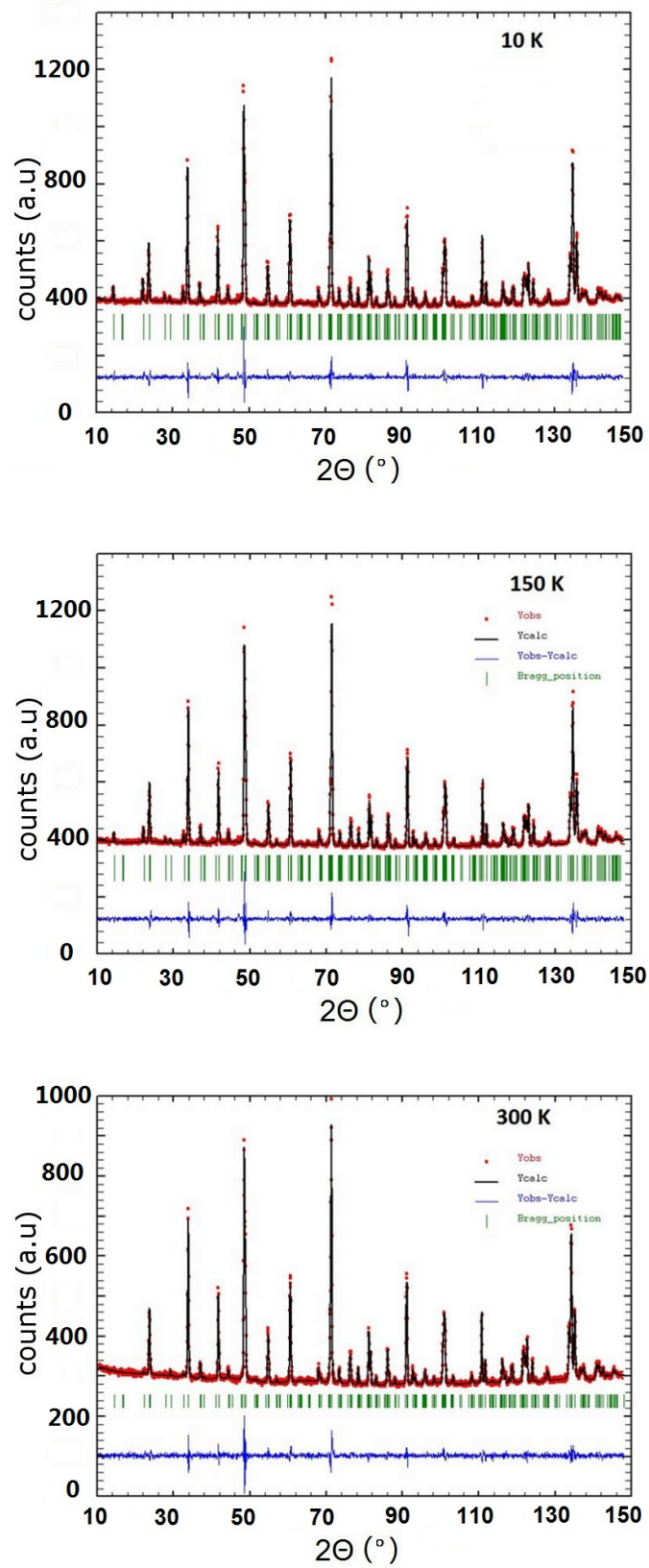
Figure 5.11.: Neutron powder diffraction pattern of $Sr_4Fe_4O_{11}$, data taken from D2B, $\lambda = 1.594216$Å. Red circles: measured data I_{obs}; Green bars: peak positions of the nuclear/magnetic peaks; Black lines: Rietveld fit (I_{calc}); Blue lines: I_{obs}-I_{calc}

Atom	X	Y	Z	Biso($\mathring{A}^2$)
Sr1	0.5000	0.0000	0.5000	0.765(234)
Sr2	0.0000	0.0000	0.5000	0.249(183)
Sr3	0.2579(7)	0.0000	0.0000	0.901(177)
Fe1	0.5000	0.2467(5)	0.0000	0.267(78)
Fe2	0.2500	0.2500	0.5000	0.497(86)
O1	0.5000	0.0000	0.0000	0.742(232)
O2	0.2679(6)	0.0000	0.5000	0.629(152)
O3	0.3803(4)	0.2750(2)	0.2394(9)	0.871(38)

Table 5.6.: Structure parameter for $Sr_4Fe_4O_{11}$ at 300K from neutron powder diffraction refined in Cmmm space group. a=10.96962(20)Å, b=7.70362(12)Å, c=5.47045(8)Å. $R_{Bragg} = 3.84$, R_f=3.73, Chi2=1.94

and pyramidal sites. According to the bond distance of the Fe-O, Fe^{4+} and Fe^{3+} can be assigned to the different coordination in the structure of $Sr_4Fe_4O_{11}$, respectively. Adler has listed the bond length of the four distinguishable phases ($SrFeO_3$, $Sr_8Fe_8O_{23}$, $Sr_4Fe_4O_{11}$ and $Sr_2Fe_2O_5$) in $SrFeO_{3-x}$ series, see Fig. 5.13. Here we compare our results with the previous reported values, listed in Table 5.7.
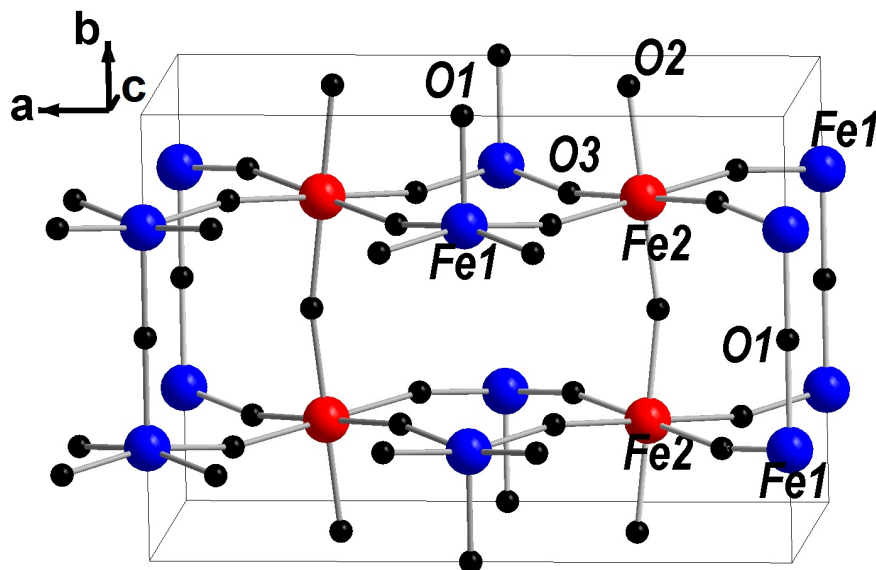
Figure 5.12.: Schematic structure of the bond distance of $Sr_4Fe_4O_{11}$

For the room temperature of our experimental data, the bond distances of Fe-O in the two different crystallographic sites agree very well with J.P.Hodges[13]. More accuracy can be reached in our case thanks to the high flux and high resolution($\Delta d/d \sim 5 \times 10^{-4}$) D2B two-axis diffractometer. Comparing with Hodges' sample[13], the bond distance of Fe(1)-O(3) are longer in our sample and the bond angles (O(1)-Fe(1)-O(3)) are smaller. Thus, Fe(1) is more closer to

Compound	Bond distances (Å)	Valence assignment	Relative abundance
$SrFeO_3$ (Ref. 28)	6×1.926	Fe^{4+}	1
$Sr_8Fe_8O_{23}$ (Ref. 28)	Fe1 : 4×1.851, 1×1.926	Fe^{4+}	
	Fe2 : 2×1.931, 2×1.952, 2×2.036	$Fe^{3.5+}$	1:2:1
	Fe3 : 4×1.912, 2×1.925	Fe^{4+}	
$Sr_4Fe_4O_{11}$ (Ref. 28)	Fe1 : 4×1.855, 1×1.90	Fe^{4+}	1:1
	Fe2 : 4×2.044, 2×1.937	Fe^{3+}	
$Sr_2Fe_2O_5$ (Ref. 34)	Fe1 : 2×1.87, 2×2.091, 2×2.180	Fe^{3+}	1:1
	Fe2 : 2×1.916, 1×1.819, 1×1.980	Fe^{3+}	

Figure 5.13.: This figure is directly reproduced from Ref[15]. The distances of Fe-O for the various members of the $Sr_nFe_nO_{3n-1}$ series of ferrates. Ref.28 in the table is Ref.[13] and Ref.34 in the table is Ref.[74]

the basal plane of the pyramidal . Moreover, the basal plane of the octahedral in our sample has shortened diagonal length(Fe(2)-O(3)).

When the temperature is decreasing, the apical oxygen (O(2)) goes a bit closer to the Fe(2) in the octahedral site, similar to Schmidt' report[14]. The Fe(2)-O(2) bonds, running along b axis, form a zigzag chain with Fe(2)-O(2)-Fe(2) = 168.29(3)° at 300K and 167.51(3)° at 10K. These angles decrease as the temperature decreasing in contrary to what is reported by Schmidt[14]. We haven't observed the increase of the bond distance Fe(1)-O(1) from 200K which is reported in Schmidt's paper[14]. In our case, the distance of Fe(1)-O(1) stays around 1.9Å and the angle O(1)-Fe(1)-O(3) stays around 96.8°. Considering the wavelength of the neutron diffraction in Schmidt's paper equals to 2.447Å which is better for the magnetic structure analysis instead of nuclear structure, we have used λ=1.594216Å that can definitely give better resolution of the nuclear structure analysis. Meanwhile, the oxygen content also influence the bond distance and angles but maybe the difference is too tiny ($SrFeO_{2.750}$ in our case and $SrFeO_{2.753}$ in Schmidt's paper) for neutron powder diffraction to distinguish.

The bond distances are one important perspective for the charge ordering debate. The main arguments are as follows[17]: the average distance of Fe(2)O6 octahedron (2.01Å) is more comparable with Fe^{3+} oxides ($LaFeO_3$ d_{Fe-O}=2.01Å[75] and $SrLaFeO_4$[76]) than with Fe^{4+} oxides ($SrFeO_3$ d_{Fe-O}=1.93 Å[13] and Sr_2FeO_4 d_{Fe-O}=1.94 Å[56]). The compressed octahedron is not uncommon and can be found in $SrLaFeO_4$[76] and $Sr_2Fe_2O_5$[74]. Moreover, the expected Jahn-Teller effect of Fe^{4+} is more favorable for elongation of octahedron other than compressed octahedron, as the case in nearly isolated Fe^{4+} O_6 units in K_2NiF_4. Thirdly, FeO_5 pyramidal in $Sr_3Fe_2O_6$ (pure Fe^{3+}) has d_{Fe-O}=1.97 Å much longer than FeO_5 pyramidal in $Sr_4Fe_4O_{11}$ (d_{Fe-O}=1.86 Å). And the same bond distance d_{Fe-O}=1.86 Å FeO_5 pyramidal units also exist in the other oxygen deficiency intermediate phase of $Sr_8Fe_8O_{23}$. Hence, the Fe^{4+} should sit in FeO_5 pyramidal units and Fe^{3+} in FeO_6 octahedral units.

Single crystal neutron diffraction has been measured on $Sr_4Fe_4O_{11}$ (twined single crystal *ACK247*) at 120K with wavelength λ= 1.178Å (in collaboration with Yvo Drees)in Trics at

| Dis/Angles	10K	150K	300K	Ref[14]	Ref[13] at room temperature
Fe(2)-O(2)	1.9325(7)*2	1.9346(7)*2	1.9360(7)*2	close to 1.93	1.937(1)*2
Fe(2)-O(3)	2.028(4)*4	2.020(5)*4	2.029(5)*4	close to 2.03 constant	2.044(2)*4
Fe(1)-O(1)	1.896(5)	1.892(5)	1.900(5)	close to 1.86 till 200K	1.90(1)
Fe(1)-O(3)	1.860(4)*4	1.870(5)*4	1.867(5)*4	close to 1.86	1.855(2)*4
O(1)-Fe(1)-O(3)	96.8(2)*4	96.9(3)	96.7(3)	97.4(4)(200K) 97.0(3)(293K)	97.0(3)*4
O(3)-Fe(1)-O(3)	89.6(3)*2 88.8(3)*2 166.4(4)*2	89.5(4)*2 88.8(4)*2 166.3(5)*2	89.6(3)*2 88.8(3)*2 166.4(4)*2	–	90.1(2)*2 88.2(2)*2 166.0(5)*2
O(2)-Fe(2)-O(3)	91.1(2) 88.9(2)	90.9(2) 89.1(3)	91.3(3) 88.7(3)	close to 90 constant	91.2(1) 88.8(1)
O(3)-Fe(2)-O(3)	89.5(3)*2 90.5(3)*2	89.5(3)*2 90.5(4)*2	89.3(4)*2 90.7(4)*2	close to 90 constant	90.0(2)*4
Fe(2)-O(2)-Fe(2)	167.51(3)	167.12(3)	168.29(3)	168.4(9)(1.5K) 167.4(7)(293K)	–
Fe(1)-O(1)-Fe(1)	180.0(4)	180.0(4)	180.0(4)	–	–

Table 5.7.: Interatomic bond distance (in Å) between the oxygen and iron atoms at three different temperatures in Cmmm space group in $Sr_4Fe_4O_{11}$. The Fe1 in pyramidal site and Fe2 in octahedral site as shown in Fig 5.12. The values are compared with Ref[14] and Ref[13]

PSI in Villigen, Switzerland. Comparing with the powder neutron diffraction, the advantage of the single crystal diffraction is that the intensity of a very large amount of reflections in reciprocal space can be measured precisely by rocking scan (ω-scans or ϕ-scans). Therefore, the single crystal diffraction is more accurate to determine the atomic position and (thermal) displacement parameter. Since the crystal is twinned along a and c directions, the b axis has to be fixed for mounting the crystal. The room temperature ω-scans has been performed at Orion in PSI in order to find the b-axis. The wavelength is λ=2.2141Å. Rocking scans of two single reflections at 2θ=70° are illustrated in Fig. 5.14. It is clearly shown that for each scan, only the expected number of reflections exist in an ω-range of more than 180°. This indicates that no other crystallites exist in this single crystal, proving the high quality of the single crystal. The oxygen stoichiometry has been determined by titration and magnetization measurement in accordance with the powder samples. When the temperature cooled down to 120K, some nuclear or magnetic peaks split, making the indexation of the single crystal much more complicated.

The magnetic structure refinement is still in progress. However, we can already see that it is extremely difficult to distinguish between the two different magnetic structures proposed by *Schmidt et al.* ($Cm'm'm'$ and $Cmm'm'$). In order to determine at least the crystal structure and to solve the question of charge ordering we have removed the low-angle magnetic reflections and refined the crystal structure. In our structural refinement, the two different magnetic structures, proposed by Schmidt et al., have been refined together with the crystal structure in order to
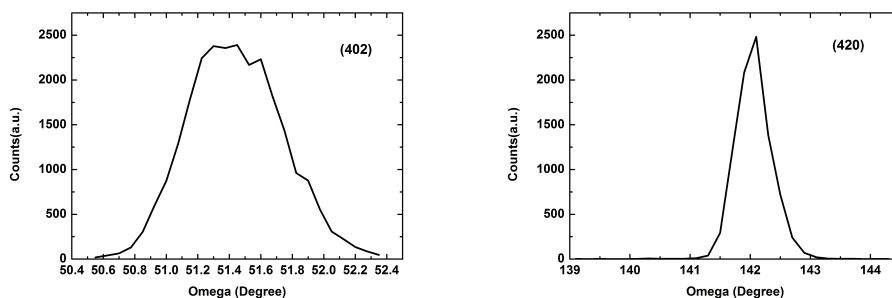
Figure 5.14.: Rocking scans (ω-scans) of single reflections

exclude systematic errors. Both refinements, the magnetic space group $Cm'm'm'$ (refinement #1) and $Cmm'm'$ (refinement #2), give very similar results as shown in Table 5.8, Table 5.9, Table 5.10 and Table 5.11.

Our bond valence sum (BVS) analysis based on the crystal structure refinement show that - independent on the use of magnetic structures $Cm'm'm'$ or $Cmm'm'$ - both results give a charge ordered structure with roughly 3.0+ oxidation state at the Fe2-site and roughly 3.8+ oxidation state at the Fe1 site. This analysis of the bond valence sums gives a very clear difference for

Sr1	ai	x	y	z	Uiso($\mathring{A}^2$)		
1	0.125000	0.500000	0.000000	0.500000	0.004091		
su	0.000000	0.000000	0.000000	0.000000	0.000343		
Sr2	ai	x	y	z	Uiso($\mathring{A}^2$)		
1	0.125000	0.000000	0.000000	0.500000	0.004091		
su	0.000000	0.000000	0.000000	0.000000	0.000000		
Sr3	ai	x	y	z	Uiso($\mathring{A}^2$)		
1	0.250000	0.259146	0.000000	0.000000	0.004091		
su	0.000000	0.000135	0.000000	0.000000	0.000000		
Fe1	ai	x	y	z	Uiso($\mathring{A}^2$)		
1	0.237475	0.500000	0.245594	0.000000	0.001026		
su	0.002753	0.000000	0.000118	0.000000	0.000000		
Fe1	Mx0	My0	Mz0				
1	0.000000	2.716191	0.000000				
su	0.000000	0.012313	0.000000				
Fe2	ai	x	y	z	Uiso($\mathring{A}^2$)		
1	0.240916	0.250000	0.250000	0.500000	0.001026		
su	0.002847	0.000000	0.000000	0.000000	0.000246		
O1	ai	x	y	z	Uiso($\mathring{A}^2$)		
1	0.131711	0.500000	0.000000	0.000000	0.001996		
su	0.001928	0.000000	0.000000	0.000000	0.000359		
O2	ai	x	y	z	Uiso($\mathring{A}^2$)		
1	0.256119	0.270396	0.000000	0.500000	0.001996		
su	0.003617	0.000175	0.000000	0.000000	0.000000		
O3	ai	x	y	z	Uiso($\mathring{A}^2$)		
1	0.947394	0.381175	0.278024	0.235245	0.001996		
su	0.010574	0.000112	0.000163	0.000174	0.000000		
Robs	Rwobs	Rall	Rwall	nobs	nall	np	nall/np
5.46	4.51	5.46	4.51	1568	1568	22	71.27

Table 5.8.: Results of refinement # 1 with SG $Cm'm'm'$.

Fe1-O1	1.8911(9)
Fe1-O3	1.8395(11)
Fe1-O3	1.8395(11)
Fe1-O3	1.8395(11)
Fe1-O3	1.8395(11)
Fe2-O2	1.9378(2)
Fe2-O2	1.9378(2)
Fe2-O3	2.0428(11)
Fe2-O3	2.0428(11)
Fe2-O3	2.0428(11)
Fe2-O3	2.0428(11)
BVS of Fe1	3.786(5)
BVS of Fe2	3.024(3)

Table 5.9.: Bond lengths and bond valence sums obtained from refinement # 1 .

Sr1	ai	x	y	z	Uiso(Å^2)
2	0.125000	0.500000	0.000000	0.500000	0.004193
su	0.000000	0.000000	0.000000	0.000000	0.000332
Sr2	ai	x	y	z	Uiso(Å^2)
2	0.125000	0.000000	0.000000	0.500000	0.004193
su	0.000000	0.000000	0.000000	0.000000	0.000000
Sr3	ai	x	y	z	Uiso(Å^2)
2	0.250000	0.259125	0.000000	0.000000	0.004193
su	0.000000	0.000136	0.000000	0.000000	0.000000
Fe1	ai	x	y	z	Uiso(Å^2)
2	0.237725	0.500000	0.245604	0.000000	0.000957
su	0.002742	0.000000	0.000117	0.000000	0.000000
Fe2	ai	x	y	z	Uiso(Å^2)
2	0.238845	0.250000	0.250000	0.500000	0.000957
su	0.002623	0.000000	0.000000	0.000000	0.000242
Fe2	Mx0	My0	Mz0		
2	0.000000	2.783140	0.000000		
su	0.000000	0.011842	0.000000		
O1	ai	x	y	z	Uiso(Å^2)
2	0.130921	0.500000	0.000000	0.000000	0.002007
su	0.001905	0.000000	0.000000	0.000000	0.000357
O2	ai	x	y	z	Uiso(Å^2)
2	0.255731	0.270304	0.000000	0.500000	0.002007
su	0.003603	0.000175	0.000000	0.000000	0.000000
O3	ai	x	y	z	Uiso(Å^2)
2	0.944812	0.381146	0.278015	0.235234	0.002007
su	0.010411	0.000112	0.000163	0.000173	0.000000

Robs	Rwobs	Rall	Rwall	nobs	nall	np	nall/np
5.41	4.50	5.41	4.50	1568	1568	22	71.27

Table 5.10.: Results of refinement # 2 with SG $Cmm'm'$.

Fe1-O1	1.8912(9)
Fe1-O3	1.8396(11)
Fe1-O3	1.8396(11)
Fe1-O3	1.8396(11)
Fe1-O3	1.8396(11)
Fe2-O2	1.9377(2)
Fe2-O2	1.9377(2)
Fe2-O3	2.0426(11)
Fe2-O3	2.0426(11)
Fe2-O3	2.0426(11)
Fe2-O3	2.0426(11)
BVS of Fe1	3.772(5)
BVS of Fe2	3.018(3)

Table 5.11.: Bond lengths and bond valence sums obtained from refinement # 2 .

both iron sites and indicates that the Fe^{4+} ions occupy the pyramidal Fe1-sites and the Fe^{3+} ions are located at the octahedral Fe2-sites. The calculation of the BVS was based on the Fe^{3+} BVS parameters for both sites. If the parameters for Fe^{4+} ions would have been used for the Fe1 site, this difference in the BVS would be even larger.

5.4.3. Magnetic structure and its spin ordering

The powder neutron diffraction for the magnetic structure has been performed at D20 with wavelength λ = 2.417921Å. The sample was placed in a standard helium cryostat and the measurements carried out over the temperature range 1.5K - 293K. Initial structure model Cmmm has been used for indexing the neutron powder diffraction pattern as proposed by J.P.Hodges [13]. The irreducible representations were produced by BasiReps software in Fullprof suite with the atomic positions of the magnetic ions (Fe) and propagation vector k =(0,0,0). The list of symmetry operators for all the irreducible representations are in Table 5.12. Each one of them has been taken as the magnetic phase and added as a secondary phase for the structure refinement.

Symmetry operators								
V	1	2 0,0,z	2 0,y,0	2 x,0,0	-1 0,0,0	m x,y,0	m x,0,z	m 0,y,z
$\Gamma(1)$	1	1	1	1	1	1	1	1
$\Gamma(2)$	1	1	1	1	-1	-1	-1	-1
$\Gamma(3)$	1	1	-1	-1	1	1	-1	-1
$\Gamma(4)$	1	1	-1	-1	-1	-1	1	1
$\Gamma(5)$	1	-1	1	-1	1	-1	1	-1
$\Gamma(6)$	1	-1	1	-1	-1	1	-1	1
$\Gamma(7)$	1	-1	-1	1	1	-1	-1	1
$\Gamma(8)$	1	-1	-1	1	-1	1	1	-1

Table 5.12.: The list of symmetry operators of all the irreducible representations for $Sr_4Fe_4O_{11}$

Based on the symmetry operators and its time reversal properties in the magnetic space group,

not all the irreducible representations are permitted on both iron sites. For Fe1 with atomic position $(1/2, y, 0)$, the magnetic moment belongs to six irreducible representations ($\Gamma_2, \Gamma_3, \Gamma_4, \Gamma_5, \Gamma_7$ and Γ_8). For Fe2 with atomic position $(1/4, 1/4, 1/2)$, the magnetic moment belongs to four irreducible representations ($\Gamma_1, \Gamma_3, \Gamma_5$ and Γ_7). Notice that Γ_3, Γ_5 and Γ_7 are allowed on both iron sites. Excellent fit between the observed diffraction data and calculated profile is obtained for Γ_2 and Γ_7. The diffraction patterns are listed in Fig 5.15. The agreement factors of the refinement for irreducible representation Γ_2 are R_{Bragg}=2.89 and magnetic R factor 9.78%. The magnetic moment on Fe(1) is 3.40(3) μ_B on the inversion center. While for Γ_7, the agreement factors are R_{Bragg}=2.86 and magnetic R factor 9.25%. The magnetic moment on Fe(2) is 3.40(3) μ_B. The value of the refined magnetic moments for these two models are equal within the experimental error. Despite the irreducible representative Γ_7 is allowed on both iron sites from the symmetry point of view, a reasonable refinement can be reached only if the value of Fe(1) is fixed to zero. The models of the two magnetic space group, corresponding to the two irreducible representatives, have been plotted in Fig 5.16. Compared with the previous results of the low temperature neutron powder diffraction[14], we have got lower magnetic moment 3.40(3) μ_B (the reported saturation value below 70K was 3.55(5) μ_B) and another magnetic space group with irreducible representation Γ_7 instead of Γ_3 in the literature. Similar to the Schmidt's paper[14], we are not able to distinguish between the two possible magnetic structures because the Fe(1) and Fe(2) have the same topology in the structure and it is very difficult to say whether the magnetic moment is located at the Fe(1) site or at the Fe(2) site.
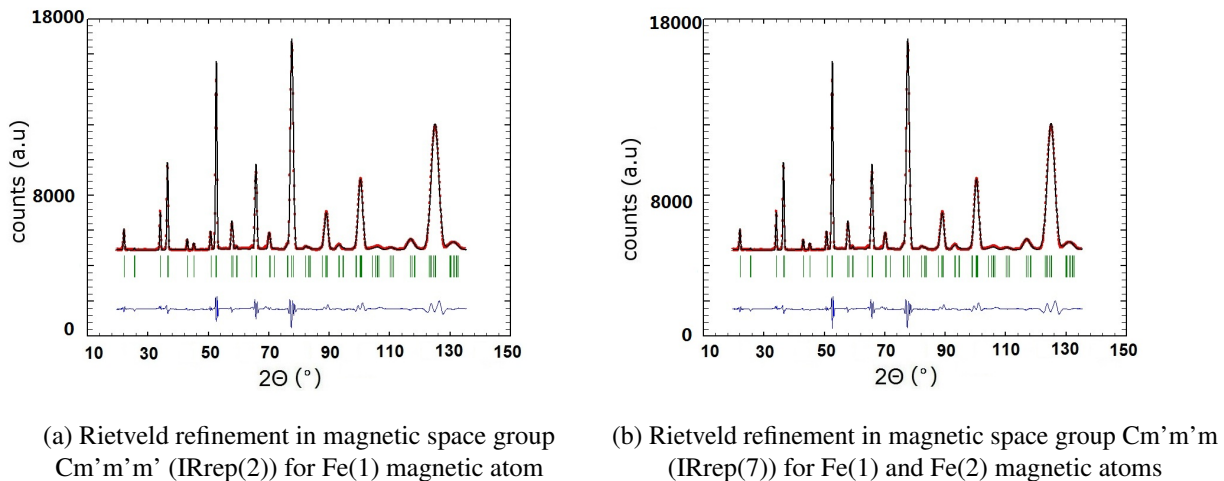

(a) Rietveld refinement in magnetic space group Cm'm'm' (IRrep(2)) for Fe(1) magnetic atom

(b) Rietveld refinement in magnetic space group Cm'm'm (IRrep(7)) for Fe(1) and Fe(2) magnetic atoms

Figure 5.15.: Powder neutron diffraction pattern measured at 1.5K(D20 diffractometer) of $Sr_4Fe_4O_{11}$; Red circles: measured data I_{obs}; Green bars: peak positions of the nuclear/magnetic peaks; Black lines: Rietveld fit (I_{calc}); Blue lines: I_{obs}-I_{calc}

5.4.4. Cell parameters anomaly

Synchrotron radiation powder X-ray diffraction measurements have been performed in order to study the lattice parameter and the symmetry change versus temperature. The X-ray beam in the synchrotron has a small divergence, thus it gives much better resolution even at higher

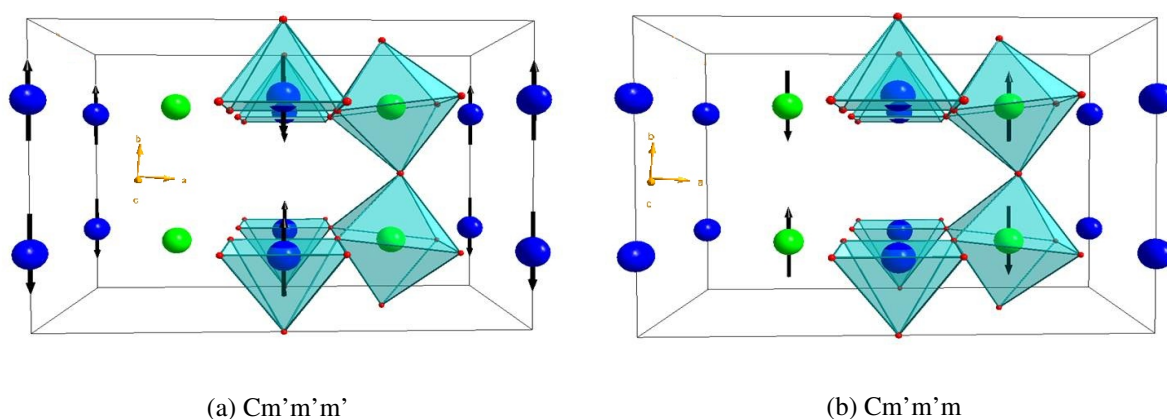(a) Cm'm'm'   (b) Cm'm'm

Figure 5.16.: The models of two magnetic space group after Rietveld refinement from the neutron powder diffraction (D20 data) at 1.5K. The blue circles are Fe(1) atoms in pyramidal site; the green circles are Fe(2) atoms in octahedral site.
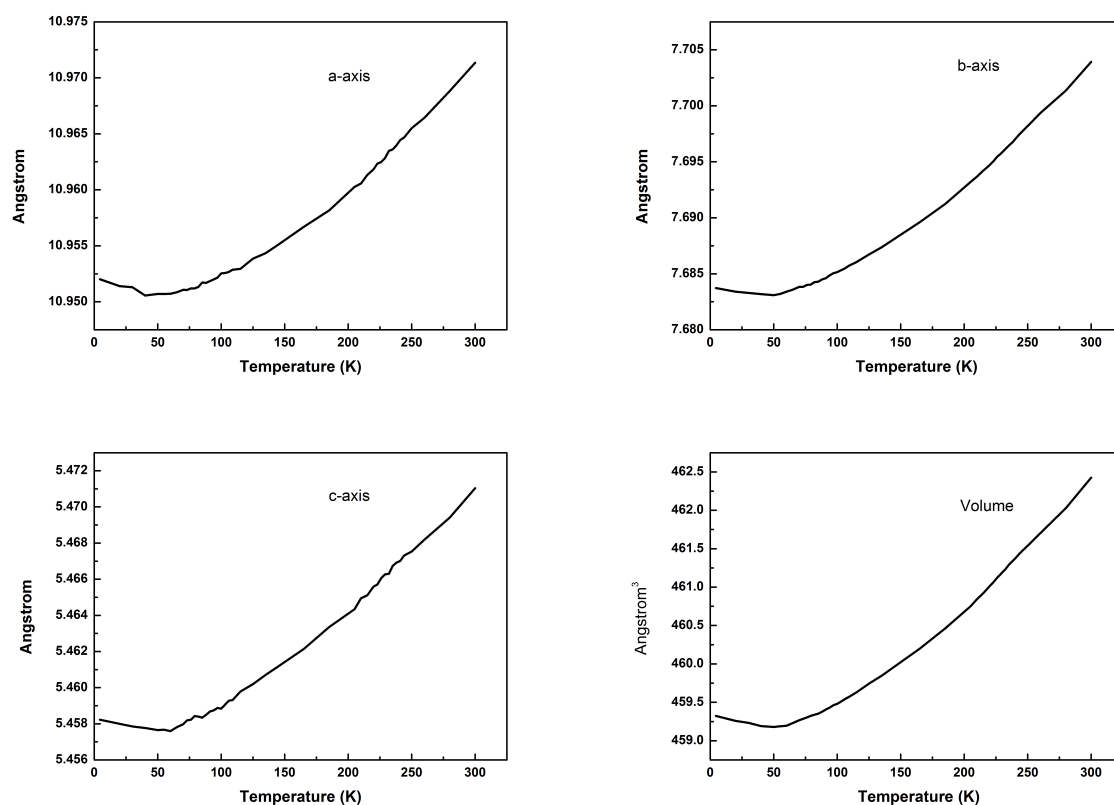

Figure 5.17.: Lattice parameter and volume change versus temperature of $Sr_4Fe_4O_{11}$

incident energy (small wavelength). Our synchrotron X-ray powder diffraction measurement has been performed in PSI at X04SA beamline. We have used wavelength λ= 0.82656Å and the sample is sealed in a silica capillary tube with an inner diameter of 0.3 mm. The NIST SRM 640C Silicon has been employed as a standard calibration in order to get a proper zero shift, Sycos and Sysin as input parameters for the refinement. The cryostat is used for cooling

down the temperature. We have measured 45 different temperatures from 4.5K to 300K on the polycrystalline $Sr_4Fe_4O_{11}$. Based on Rietveld refinement of Fullprof suite, we have get lattice parameters and volume change versus temperature, plotted in Fig 5.17. A clear change at 55K for all the lattice parameters is observed, which is in accordance with the previous reported magnetization measurements where a spin glass transition temperature at 50K was predicted[71]. But the negative thermal expansion, occurring at low temperature, is somehow strange. We have also fitted the width of several specific peaks, shown in Fig 5.18 . And similar changes occurred around 50K. This negative thermal expansion is observed in compound Sr_2FeCoO_6 as well[77], which is also perovskite.
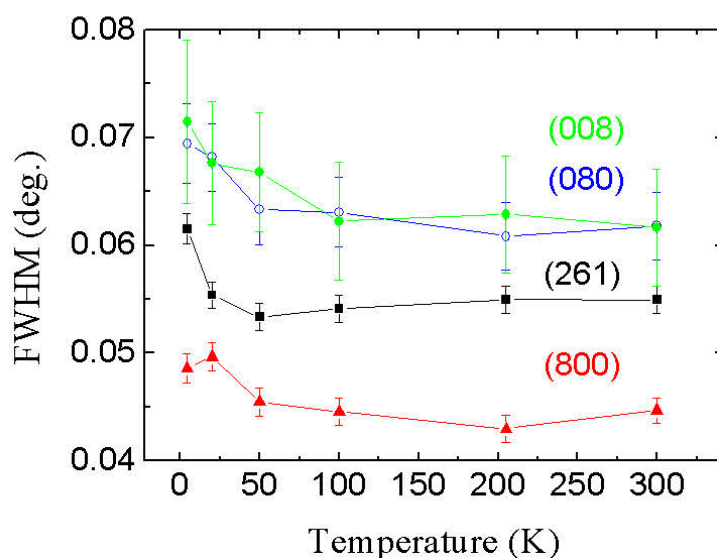

Figure 5.18.: The peak width of several specific peaks versus temperature

5.5. Conclusion

The powder and single crystals have been synthesized for $Sr_4Fe_4O_{11}$. The oxygen stoichiometry has been determined by titration. A detailed Rietveld analysis on two batches of powder samples with tiny difference in oxygen content reveal the high sensitivity of the crystallographic structure to the oxygen stoichiometry. Temperature-dependent neutron powder diffraction data for the crystallographic structure analysis have been presented together with precise bond-length and angles of Fe-O in the two crystallographic sites. The bond valence sum calculation based on these single crystal neutron diffraction data clearly showed that the Fe^{4+} is in the pyramidal site and Fe^{3+} is in the octahedral site. Temperature-dependent synchrotron X-ray diffraction on the powder samples exhibit a new transition temperature around 50 K where a negative thermal expansion arising.

Chapter 6.

Magnetic and transport properties of $Sr_4Fe_4O_{11}$

6.1. Seebeck coefficient, magnetism, resistivity and specific heat of $Sr_4Fe_4O_{11}$

Strontium ferrates $SrFeO_{3-x}$ are considered as good candidates for high-temperature oxygen-permeable membranes and oxygen sensor electrodes owing to the fact that they exhibit high oxygen-ionic and electronic conductivity. For the high temperature region ionic conductivity (oxygen mobility) plays a major role in the mechanism of the conductivity, while at low temperature electron conductivity is expected to dominating[78]. In this thesis for the compound $Sr_4Fe_4O_{11}$ with specific oxygen stoichiometry, we will only focus on the low temperature region, in which the electron conductivity suppose to play the major role.

6.1.1. Seebeck coefficient

The Seebeck coefficient is the effect used in thermocouples, and measures the potential difference generated across a sample in response to a temperature gradient. It provides complementary information to resistivity measurements. In high temperature limit, the thermopower is said to measure the entropy per carrier [79] which can be considered as the first derivative of the electron density of states close to Fermi energy. In the system with large many-body interactions, for the high temperature limit, Heikes formula is used for the thermopower:

$$S \longrightarrow (k/e)[ln(c/(1-c)) + A]$$

[80] , where e is the absolute value of electron charge, k is the Boltzmann constant and $ln(c/(1-c))$, for mixed valence compounds, is the relative amount of different oxidation states. And the measure of configuration entropy is related with the band structure ($\propto T/T_f$, T_f is the Fermi temperature), the distribution of charge carriers ($\propto \ln\frac{1-c}{c}$) and the ratio of the number of the orbital and spin degenerated states (c). As it is measuring the thermal resistivity, it is relatively insensitive to the presence of electrically resistive grain boundaries.

E.K.Hemery and co-workers have investigated the thermoelectric power in $SrFeO_{3-x}$ (x=0.05, 0.135, 0.19, 0.21, 0.22)[78]. They found that the TEP at 300K increases systematically with decreasing oxygen content that corresponds to an average electron doping. And there is a big drop around 70K in the TEP (thermoelectric power) versus temperature plot. This drop is related to charge ordering in the $Sr_8Fe_8O_{23}$ fraction of the sample and demonstrates a change in the nature of the charge carriers. Consistently, around the same temperature, they also observe that the resistivity has increased by one order of magnitude. This makes them conclude that the large drop in the TEP is a consequence of Verwey-like charge ordering.
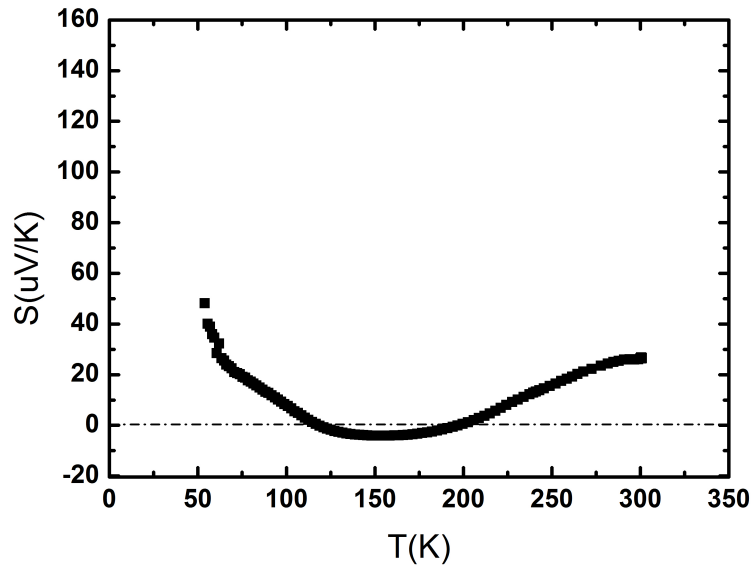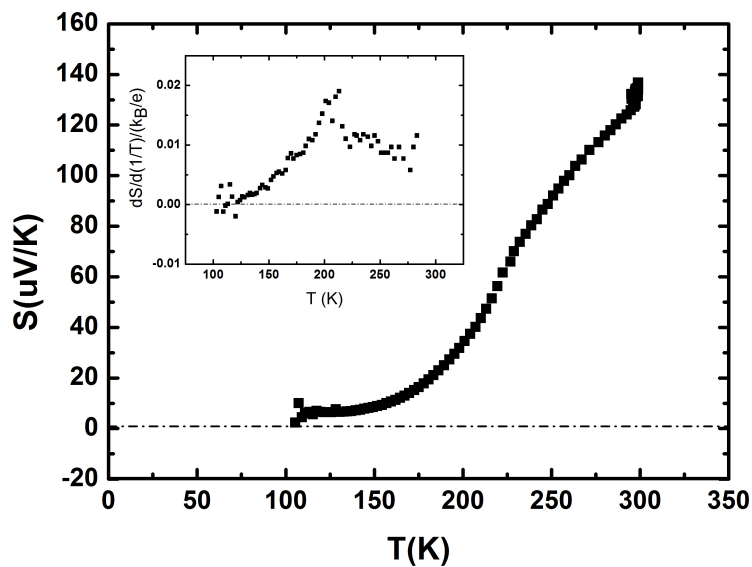
(a) Pellet annealed for one week at 617°C

(b) Pellet annealed for two weeks at 617°C

Figure 6.1.: comparison of two batches of samples annealing with different length of time

In this thesis we have reinvestigated the Seebeck coefficient of the compound $Sr_4Fe_4O_{11}$ that have been prepared previously in Section 5.1. In Figure 6.1, the Seebeck coefficient versus temperature of two batches of samples are shown. As already discussed in Chapter **??**, the difference of these two batches is that they have been annealed with different time, one annealed for one week and the other one annealed for two weeks (marked in the figure). This leads to the different structures of these samples, one week annealed sample has tiny $Sr_8Fe_8O_{23}$ phase

while two week annealed sample only shows $Sr_4Fe_4O_{11}$ phase from X-ray diffraction pattern. The Seebeck coefficients of these two batches, however, display very different behavior versus temperature. Above 100K , both samples show increasing Seebeck coefficient with increasing temperature. However, clear changes around 100K are observed for the two batches. Notice that for the two week annealed sample, its resistivity is too high below 100K that it exceeds the measurable range of the machine. Compared with the previous reported work from E.K.Hemery et.al[78] which show the magnitude of the drop of the Seebeck coefficient around 70K decrease with oxygen deficiency increasing, our Seebeck coefficient don't indicate any drop around 70K for both batches. As this drop for the Seebeck coefficient disappears for the highest oxygen deficient sample $SrFeO_{2.78}$ in Reference[78], this means our oxygen deficiencies are lower than 2.78 . According to the Reference[78], this drop is the representative of the reminiscent of $Sr_8Fe_8O_{23}$ phase, we can conclude that in our two samples there is negligible $Sr_8Fe_8O_{23}$ phase exist in the errors of the Seebeck coefficient experiment. This is also in terms with our XRD results which show only in the one week annealing time sample a tiny amount of $Sr_8Fe_8O_{23}$. In the inset of Fig 6.1b, we show the derivative of the Seebeck coefficient. By applying Heikes formula, $\frac{dS/d(1/T)}{k_B/e}$ are used instead of Seebeck coefficient versus temperature, two kinks are observed, one is around 235K which corresponds to the antiferromagnetic transition, another one is around 100K. This second transition occurs at the temperature close to the new magnetic transition temperature in our μSR measurement, where a second magnetic transition are observed besides the Néel transition (T_N=235K) .

6.1.2. Resistivity and magnetization

P.Adler et al[15] have investigated the resistivity and magnetization of single crystals $SrFeO_x$ with different oxygen compositions . In the high oxidation samples (x=3.00$\sim$2.85), the onset of helical order at 130K is visible, meaning the existence of cubic phase. Another kink around 60K in both the susceptibility and the resistivity curves in the phase of $SrFeO_3$ is possibly a spin reorientation in the helical phase[81]. The anomalies at 75K ($SrFeO_{2.95}$) or 70K ($SrFeO_{2.85}$) are
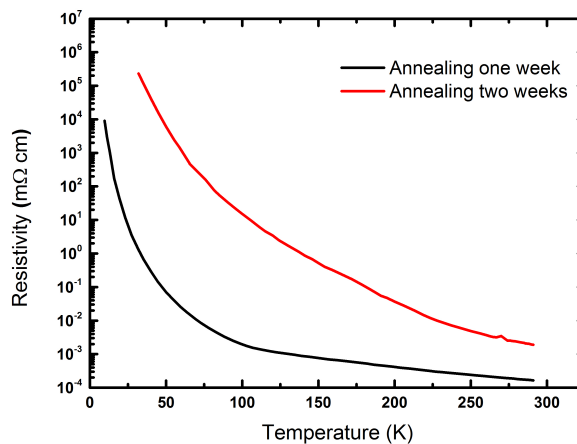

Figure 6.2.: Resistivities of the two sample batches with different annealing time

a signature of the onset of antiferromagnetic order in the tetragonal phase ($SrFeO_{2.875}$), which follows from a decrease of the susceptibility upon cooling. For $SrFeO_{2.77}$, a composition close to $Sr_4Fe_4O_{11}$, anomalies near 230K and 50K are discernible in the susceptibility curve. The first transition temperature 230K reflects the antiferromagnetic ordering of Fe^{3+} sites in $Sr_4Fe_4O_{11}$, whereas a upturn below 50K is assumed to be associated with the Fe^{4+} sites which remain magnetically disordered[15].
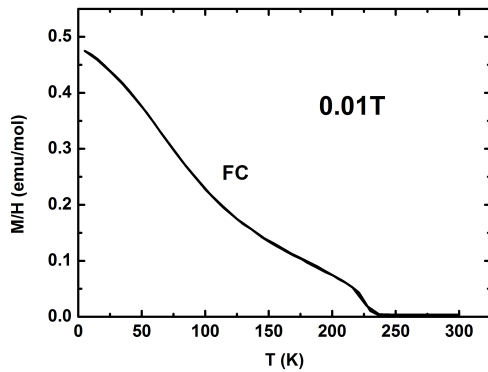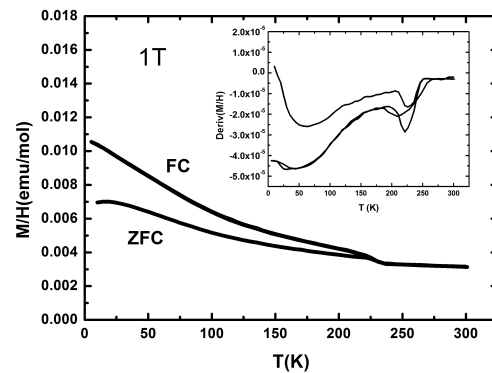

(a) Magnetic susceptibility of one week annealed sample $SrFeO_{2.753\pm0.005}$ at B=0.01T field cooling
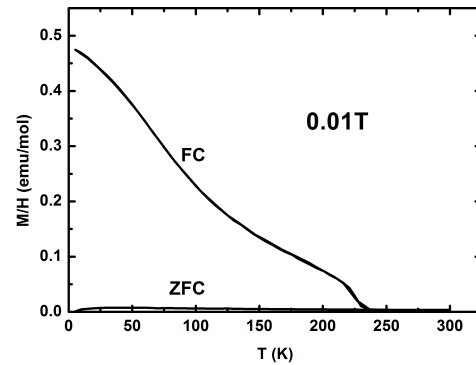
(b) Magnetic susceptibility of two weeks annealed sample $SrFeO_{2.750\pm0.005}$ at B=0.01T field cooling and zero field cooling
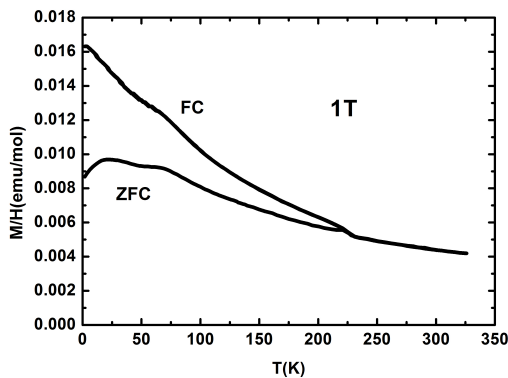
(c) Magnetic susceptibility of one week annealed sample $SrFeO_{2.753\pm0.005}$ at B=1T field cooling and zero field cooling

(d) Magnetic susceptibility of two weeks annealed sample $SrFeO_{2.750\pm0.005}$ at B=1T field cooling and zero field cooling, inside plot is the derivative of the magnetization curve

Figure 6.3.: Magnetic susceptibility under different magnetic field for the two sample batches

In this thesis we have reinvestigated the resistivity of $Sr_4Fe_4O_{11}$ at low temperature without magnetic field, see Fig 6.2. Compared with the published single crystal data, the slope of the curve is similar to the closest oxygen stoichiometry $SrFeO_{2.77}$. However, our two polycrystalline samples show different resistivity value due to their different annealing time. In accordance with the published single crystal data that the resistivity increase with the increasing oxygen deficiency, the sample which is annealed for two weeks has a higher resistivity than the sample only annealed for one week. This indicate the long annealed sample have higher oxygen deficiency than the
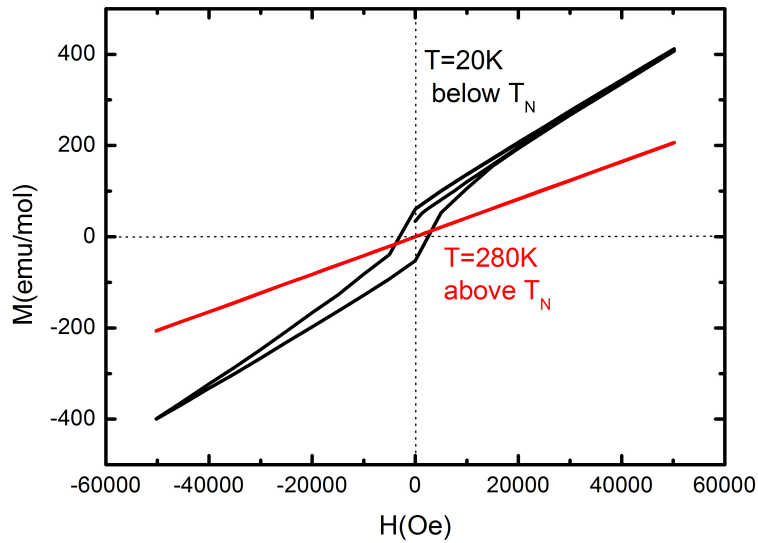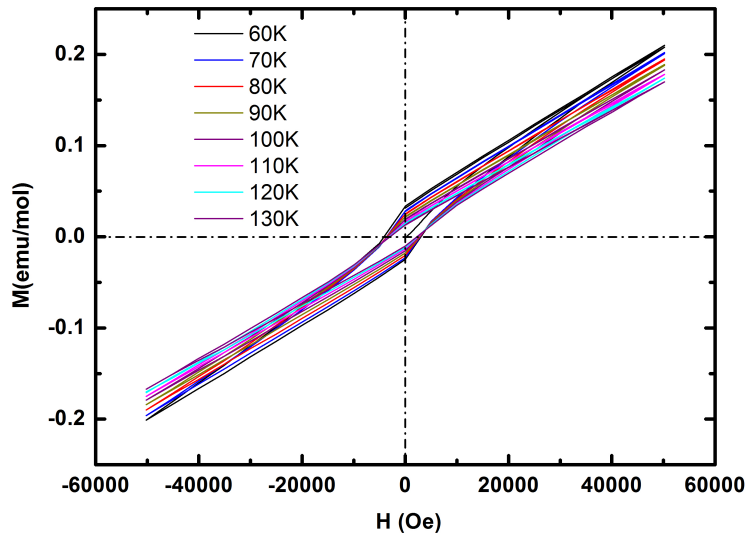
Figure 6.4.: Magnetization versus field for two weeks annealed sample $SrFeO_{2.750\pm0.005}$ at 20K and 280K

short annealed sample. This result is in line with our X-ray diffraction data, which show that the short annealed sample has a tiny amount of $SrFeO_{2.875}$.

The magnetization of the two batches of samples have been carefully studied in this PhD work. As shown in Fig 6.3, under 100Oe magnetic field(Field Cooling Mode), the two batches show very similar magnetization curves. But when applying a higher magnetic field (1T in this case), there is another kink appearing around 70K in the one week annealing sample, which corresponds to the known transition temperature of the tetragonal phase $SrFeO_{2.875}$. This result is not surprising as we indeed observe the tiny amount of secondary phase $SrFeO_{2.875}$ in the powder X-ray diffraction data and is also in line with our Seebeck coefficient and resistivity measurements. The derivative of the magnetization curve in Figure 6.3d shows that there are only two anomalies around 230K and 50K. The 230K anomaly is the well known antiferromagnetic transition as reported previously in Ref [15], while the anomaly at 50K is not a clearly defined transition temperature. In comparison with reference[14], the magnetization curves (Zero Field Cooling Mode) displayed in Fig 6.3b is not typical for an antiferromagnetic system which is characterized by a downturn of the curve below the Néel transition temperature instead of the straight or even upturn curve . Furthermore, a pronounced divergence between magnetic susceptibility curves measured under field cooling and zero-field cooling conditions below 230K points to a system with competing interaction as suggested by previous work [82] .

In order to get a closer look to the anomaly magnetic behavior, the magnetization versus field curves have been measured above and below the Néel transition temperature. In case of an ideal antiferromagnet, one would expect a linear M(H) behavior. In Fig 6.4, however, a weak ferromagnetic signal appears to be superimposed to the antiferromagnetic behavior, which in the paramagnetic region the magnetization curve stays a straight line. Possible origins for the ferromagnetic signal maybe spin canting or spurious ferromagnetic clusters in the antiferromagnetic material. Curie-Weiss law can not be applied in the paramagnetic region for

(a) Magnetization versus field for two weeks annealed sample $SrFeO_{2.750\pm0.005}$ at different temperature
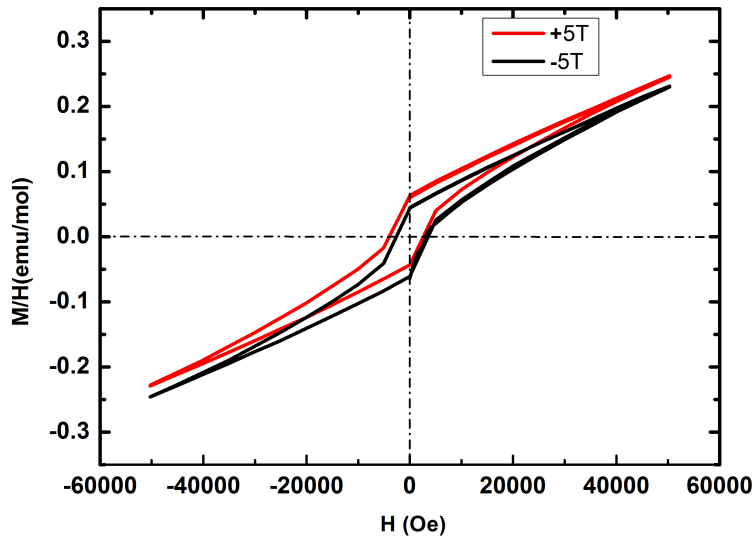
(b) Magnetization versus field for two weeks annealed sample $SrFeO_{2.750\pm0.005}$ at 10K after cooling in an applied magnetic field of +5 or -5T.

Figure 6.5.: Magnetization versus field for two weeks annealed sample $SrFeO_{2.750\pm0.005}$

both samples under 100Oe, because of the measured temperature range above the Néel transition temperature is too small to assume an accurate fit of Curie-Weiss law.

Additional measurements of the magnetization versus field curves have been done from 60K to 130K (Zero Field Cooling Mode) in order to give supplementary information for the μSR measurement where a new magnetic transition occurs around 90K and will be presented later

in this chapter. In Fig 6.5a, the magnetization curves versus magnetic field are measured in every 10K from 60K to 130K. All curves show very similar behavior with weak ferromagnetic signal superimposed to antiferromagnetic behavior, no clear change observable in this region. Comparing with the work Ref [83], if cooling the sample under 5T and -5T magnetic field at 10K (see Fig 6.5b), respectively, we can observe the divergence of the magnetization loops , but the coercive fields are quite different from Reference[83] . The reason may be due to different oxygen stoichiometry since the published work only estimated the oxygen content by mass difference which will give more error than in our case.

6.1.3. Specific heat

The specific heat measurement is, in general, used as a powerful tool for studying phase transitions. To our knowledge, there is no report of specific heat measurement on $Sr_4Fe_4O_{11}$. In this thesis we have investigated the specific heat at low temperature in zero magnetic field, shown in Fig 6.6. We can see clearly the known antiferromagnetic transition around 230K while no other transition temperature exist. The specific heat of a sample depends on the number of degrees of freedom that is available for the sample to store thermal energy, and it usually contains lattice, electron and magnetic degrees of freedom. Our result indicates that the lower temperature anomalies, being observed in the other experiments, are not due to a well-defined magnetic or structural phase transition but may rather correspond to processes in the frustrated magnetic structure which are not observed in the specific heat measurement.
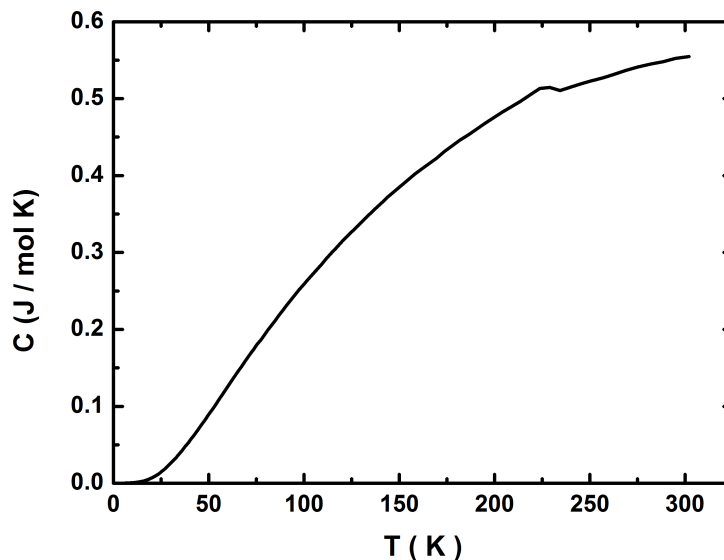

Figure 6.6.: Specific heat measurement versus temperature of the two weeks annealing sample

6.2. Mössbauer spectra for $Sr_4Fe_4O_{11}$

M.Takano has investigated the electronic state of $SrFeO_x(2.5{\leq}x{\leq}3)$ with Mössbauer spectroscopy on three samples with different oxygen stoichiometry[11]. For the compound $SrFeO_{2.73}$, the spectra at T=300K, which are above the ordering temperature , show quadrupole splitting only, with no magnetic splitting. This quadrupole splitting arises from a static electric field gradient (EFG) from the surrounding ions of iron. When the temperature cools down to T=4K, a magnetic hyperfine field B_{hf} appears. Referring to Table 6.7, there are four components in the spectra of $SrFeO_{2.73}$. The isomer shifts of components 1 and 2 correspond to Fe^{+4} while the isomer shifts of components 3 and 4 are characteristic of Fe^{+3}. The magnetic hyperfine splitting observed for two of the sites (Fe^{3+}) confirms that $Sr_4Fe_4O_{11}$ is magnetically ordered at 4K. In the absence of an external magnetic field, it is impossible to discriminate between ferro- and antiferromagnetic order from the Mössbauer data. The magnitude of B_{hf} increases as the temperature decreases(detailed study can be found in the PhD thesis of Moya [84]). This behavior of B_{hf} reflects the temperature dependence of the magnetization of the material. It appears in the Mössbauer spectra of $Sr_4Fe_4O_{11}$ as broadening of the outest two lines in the sextet.

The negative isomer shift of component 1 was explained as low spin d^4 Fe^{4+} which has a $^3T_{1g}$ ground state with a J=0 state lying lowest[11]. And the large quadrupole splitting of component 3 in comparison with component 4, even though both of them are arising from high spin Fe^{3+}, was attributed to the five-coordinated site[11].

MÖSSBAUER DATA FOR PHASES $n\infty$, $n8$, AND $n4$ OF THE $SrFeO_{3-1/n}$ SYSTEM

		300 K				4 K				
$3-1/n$	Component	IS/mm/sec	ΔE/mm/sec	%	Valence	IS/mm/sec	ΔE/mm/sec	Hi/T	Valence	%
2.97	1	0.06	—	94	Fe^{4+}(HS)	0.2	—	33	Fe^{4+}	95
($n\infty$)	2	0.32	—	6	Fe^{3+}	0.4	—	51	Fe^{3+}	5
2.86	1	0.04	—	45	Fe^{4+}(HS)	0.0	—	29	Fe^{4+}	50
($n8$)	2	0.17	0.84	55	$Fe^{3.5+}$	0.4	—	44	Fe^{3+}	30
2.73	1	−0.09	0.34	33	Fe^{4+}(LS)	Very broad absorption				48
	2	0.11	—	9	Fe^{4+}(HS)	centered around ~0 mm s^{-1}				
($n4$)	3	0.37	1.29	53	Fe^{3+}	0.5	−1.29	46	Fe^{3+}	38
	4	0.35	0.58	5	Fe^{3+}	0.4	0.3	47	Fe^{3+}	14

Note. IS, isomer shift vs metallic iron; ΔE, quadrupole splitting= $\frac{1}{2}e^2qQ(1 + \eta^2/3)^{1/2}$; Hi, magnetic hyperfine field; HS, high-spin state; LS, low-spin state.

Figure 6.7.: This figure is reproduced from reference[11]. Mössbauer data of $SrFeO_{2.97}$,$SrFeO_{2.86}$,$SrFeO_{2.73}$ [11]

Later work on $SrFeO_{2.71}$, however, doubted these results[82]. Since an even larger field gradient is observed at the octahedral sites in $Sr_2Fe_2O_5$ with a regular coordination geometry and the low spin Fe^{4+} can't explain the strong field sensitive of the spectra below the critical temperature, T.C.Gibbs proposed the Fe^{3+} in octahedral sites and the high-spin Fe^{4+} in pyramidal sites.

P.Adler et al[15] have recently studied the phase of $SrFeO_{2.69}$, in combination with structure refinement results[13], explained the large quadrupole splitting for the Fe^{3+} site in $Sr_4Fe_4O_{11}$ is due to a strongly distorted octahedral Fe^{3+} site in the structure.

The most important results, are however, that the Fe^{4+} sites remain magnetically disordered. The broadening of the peak at low temperature is believed to result from a supertransferred

hyperfine interaction with neighboring, magnetically ordered Fe^{3+} ions and/or from a small magnetic moment induced by a second-order perturbation[84].

In view of the discrepancies regarding the interpretation of the Mössbauer spectra of $Sr_4Fe_4O_{11}$, in this PhD work, we have reinvestigated the system of $Sr_4Fe_4O_{11}$ by Mössbauer spectroscopy for our two different annealing time samples.

At room temperature, the two batches have similar spectra see Fig 6.8. With the quadrupole distribution mode, three different distributions for the two spectra have been used. The resulting isomer shift and quadrupole shift are quite similar for these two spectra(Table 6.1). Two isomer shift values close to zero can be attributed to Fe^{4+} and the other higher isomer shift is typical for Fe^{3+}. A weak shoulder at the Doppler velocity of 0.4 mms^{-1} is only seen in the Mössbauer spectrum of the one weak annealed sample and can be attributed to the minority tetragonal phase, apparent also in other experiments. If we compare the Mössbauer spectra of room temperature with low temperature data Fig 6.9, we can see that at room temperature, there are only quadrupole doublets, corresponding to the paramagnetic region, while in the magnetically ordered state (the low temperature spectra), the magnetic hyperfine field produces one Fe^{3+} sextet in addition to a Fe^{4+} quadrupole doublet.

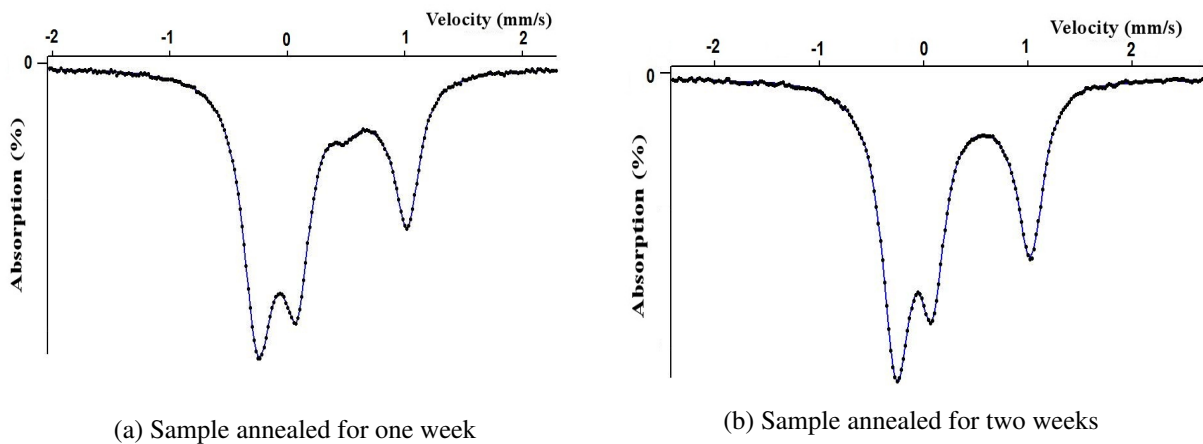(a) Sample annealed for one week

(b) Sample annealed for two weeks

Figure 6.8.: Comparison of the Mössbauer spectra of the two batches of $SrFeO_{2.75}$ at room temperature

DIS	δ(mm/s)	Δ(mm/s)	Γ(mm/s)	%
D1	-0.04	0.26	0.2	31.5
D2	0.37	1.26	0.2	44.6
D3	0.07	0.56	0.2	23.9

DIS	δ(mm/s)	Δ(mm/s)	Γ(mm/s)	%
D1	-0.07	0.35	0.2	24.9
D2	0.36	1.29	0.2	50.7
D3	0.03	0.50	0.2	24.4

Table 6.1.: Distribution analysis of Mössbauer parameters for the two batches of samples. The left panel is for one week annealed sample and the right panel is for two weeks annealed sample. The sites with a distribution of quadrupole splittings have been assumed. δ is the isomer shift, Δ is the quadrupole splitting. Γ is the linewidth. The relative contribution (percentage) of the signals was obtained from the area fractions.

In some of the previous work, for the orthorhombic phase at room temperature, the spectra have been fitted with two doublets, see Table 6.2. In our case, however, a fit with two different sites is not satisfactory. We have fitted our spectra with four different quadrupole distributions,
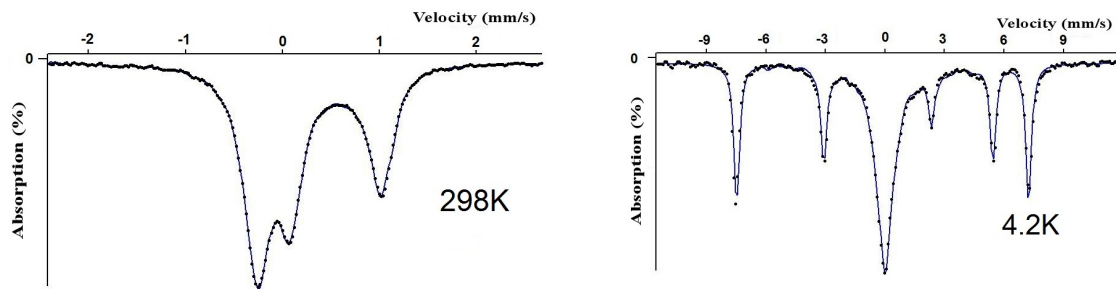
Figure 6.9.: Comparison of low temperature and room temperature Mössbauer spectra of the $SrFeO_{2.75}$ annealed for two weeks

	Isomer shiftδ	Quadrupole splittingΔ
doublet 1	-0.11 mm/s[84] or -0.09 mm/s[15]	0.38 mm/s[84] or 0.32 mm/s[15]
doublet 2	0.41 mm/s[84] or 0.34 mm/s[15]	1.20 mm/s[84] or 1.35 mm/s[15]

Table 6.2.: Examples of two doublet fitting of room temperature Orthorhombic phase

listed in Table 6.3. Comparing with the three distribution fit, another quadrupole splitting is added. Therefore, the asymmetric distribution of the single peak is more clearly observed. It is difficult to judge which fit is better since additional quadrupole distribution figure would be needed which is not available during the thesis writing. However, we found out our parameters are quite different from Takano's work. In essence, the parameters of sites D1 and D3 on one hand and of sites D2 and D4 on the other, are similar and they can assigned to the Fe^{4+} and Fe^{3+} sites in the crystal structure of $Sr_4Fe_4O_{11}$ respectively. But the certain distribution of hyperfine parameters possibly corresponds to residual defects which cannot be completely avoided. These arguments are in line with the previous report where larger difference in the parameters of $SrFeO_{2.73}$ [11] which departs stronger from the ideal stoichiometry.

DIS	Isomer shiftδ(mm/s)	Quadrupole splittingΔ(mm/s)	%
D1	-0.07	0.47	25
D2	0.37	1.39	37
D3	0.04	0.37	23
D4	0.26	1.54	15

Table 6.3.: Four distributions fitting of room temperature Orthorhombic phase of this PhD work

Further support of this view is obtained for the low temperature spectrum of the $Sr_4Fe_4O_{11}$ sample annealed for two weeks (Figure 6.9). The spectrum is most reliably fitted by one sextet corresponding to Fe^{3+} with large B_{hf} (47T) and one Fe^{4+} magnetic component with a small B_{hf} (8T) (Table 6.4). A magnetic component instead of a quadrupole doublet is used in order to account for a certain linebroadening seen in the Fe^{4+} signal at low temperatures, and the reason of the line broadening will be discussed later on. The intensity ratio for the Fe^{3+} and the Fe^{4+} sites is approximately 1:1 which verifies the nearly stoichiometric $Sr_4Fe_4O_{11}$ composition.

The distribution of the peaks in the Fe^{3+} sextet is not symmetrical with respect to the center

DIS	δ(mm/s)	ε(mm/s)	Γ(mm/s)	B_{hf}(T)	%
H1	0.48	-0.65	0.30	47	49
H2	-0.05	0.005	0.35	8	51

Table 6.4.: Distribution analysis of Mössbauer parameters at 4.5K for the two week annealing sample. δ is the isomer shift, ε is the quadrupole interaction in the magnetically ordered phase, Γ is the linewidth, B_{hf}(T) is the magnetic hyperfine field.

of the pattern, which is in agreement with the pronounced quadrupole interaction for the Fe^{3+} component. This is particularly evident from the difference Δv in Doppler velocities between lines 1/2 and 5/6, respectively. Considering that the quadrupole splitting ΔE_Q is still considerably smaller than the hyperfine field B_{hf}, the combined magnetic and quadrupole interaction can be treated within the perturbation approach. The Fe^{3+} spectrum is modeled by a single hyperfine sextet with the hyperfield B_{hf} and the quadrupole interaction parameter ε. Assuming an axially symmetric EFG (asymmetry parameter η=0), ε can be written as(6.1)

$$\varepsilon = \frac{eQV_{zz}}{4}\left(\frac{3\cos^2\theta - 1}{2}\right) \tag{6.1}$$

where θ is the angle between the principle axis of the EFG and the direction of B_{hf}. Assuming that V_{zz} and B_{hf} are parallel (θ=0), one obtains(6.2)

$$|\varepsilon| = \left|\frac{eQV_{zz}}{4}\right| = \frac{1}{2}\Delta E_Q \tag{6.2}$$

where ΔE_Q is the quadrupole splitting observable in the spectra of the paramagnetic phase. This is , however, only valid if there is no structural phase transition, otherwise ΔE_Q can change. In our case, we have ε = -0.65 mm/s at 4K, which leads to ΔE_Q = 1.30 mms^{-1} if $B_{hf}\| V_{zz}$ is assumed. This is in reasonable agreement with the ΔE_Q value of 1.39 mms^{-1} for the main Fe^{3+} component in the room temperature spectrum and suggests that V_{zz} and B_{hf} are indeed essentially parallel. This is also in agreement with magnetic and crystal structure. In Section 5.4 where the detailed bond lengthes and angles are presented, Fe(2) in octahedral site have longer bond length with the four planar oxygens O(3)(2.028(4)*4) than with the two apical oxygens O(2)(1.9325(7)*2). This compressed octahedral site would form a local quasi-tetragonal symmetry, which would have the principle axis of electric field gradient V_{zz} parallel with the antiferromagnetic ordered spin. The B_{hf} value of 47.3T and the isomer value of 0.47 mm/s at 4.2K are typical for Fe^{3+} , as compared with our previous work on Fe^{3+}in different coordination. It has been suggested that the quite small B_{hf} for the Fe^{3+} site reflects the reduced dimensionality of the magnetic exchange network[82].

We would like to emphasize here one important observation. A continuous broadening of the central Fe^{4+} peak below 150K has been observed previously in a more detailed temperature-dependent study of the Mössbauer spectra of $Sr_4Fe_4O_{11}$ [84]. This was also observable from the spectrum of Ref[15], where a single crystal of $SrFeO_{2.69}$ has been measured. It was suggested that the broadening is due to a supertransferred hyperfine field in course of the spin ordering of the Fe^{3+} spins. A small magnetic moment in the Fe^{4+} sites induced by the moments of the Fe^{3+} sublattice may also be the reason for the small ferromagnetic contribution to the magnetic behavior (see above).

6.3. μSR

As it is mentioned in Chapter 2.5, zero field μSR is very sensitive to weak internal fields and it is therefore a powerful tool to study magnetic phase diagrams[40, 85]. For the compound $Sr_4Fe_4O_{11}$, we have already observed a weak ferromagnetic interaction in the antiferromagnetic region in the dc magnetization versus field measurement while nothing can be observed in the ac susceptibility measurement. The μSR measurement gives complementary information about the magnetism of $SrFeO_{2.75}$. Furthermore, the previous study of this system with neutron and magnetization measurement still left many open questions, we would like to use μSR as a new approach to study the magnetism of this system.

Our data were recorded in the temperature range of 2-280K with a dynamical helium flow cryostat at the DOLLY instruments located on πE1 beam lines of the Swiss Muon Source (Paul Scherrer Institute Villigen, Switzerland). The forward and backward positron detectors enclose angles of approximately 0 and π with an initial muon spin polarization P(t=0) antiparallel to the muon momentum. The time-differential μSR data deduced from positron events is expressed as AP(t), where A is the full asymmetry and P(t)is the projection of P(t) onto the axis passing the two positron detectors.

Figure 6.10 shows the muon spin polarization as a function of time for four different characteristic temperatures. Above the Néel transition temperature (230K), the system is paramagnetic and its polarization curve shows a weak relaxation only. This indicates that the system is in the paramagnetic state. The spectrum can be described by a Gaussian Kubo-Toyabe function due to static nuclear moments only. Around $T_N \approx 228$K, an additional exponential depolarization occurs. This suggests commence of the static or slowly fluctuating electronic moments. At lower temperatures (e.g.T= 145K in the Fig 6.10), a well defined spontaneous μ^+ spin precession develops indicating the electronic moments become static on the scale of the muon lifetime and the muon spin precesses in the static local fields. This clearly indicates that the system is long range magnetic order. Surprisingly, below 90K, the μSR spectra change drastically and four superimposed long-lived oscillation frequencies are observed. This complexity of the spectra demonstrate that there are four different magnetically inequivalent μ^+ sites. And the data can be fitted with the usual Cosine functions for commensurate magnetism and a nonmagnetic signal that could account for impurity or other nonmagnetic phases in the sample. We have measure in two different batches of the sample that have been annealed for one week and two weeks separately and their behavior in the zero field μSR spectra is very similar. Owing to the discussion of the comparison of the purity between these two batches in different sections in this thesis, we can exclude the nonmagnetic signal comes from an impurity phase.

In the Fig 6.11,we can see clearly the four different frequencies at low temperature and gradually merged to one frequency at 110K. This means that the four magnetically inequivalent muon sites in an inhomogeneous phase at lower temperatures merged into a single phase at higher temperatures. Three different explanations for this observation are possible: 1. A coexistence of spatially separated magnetic phases. It could be an indication that the homogenous system gradually transforms from one phase to another but retaining the other phase. However, this is not observable from the specific heat measurement. According to theoretical calculations, G-type antiferromagnetic state is the ground state of this system while it coexists with another secondary
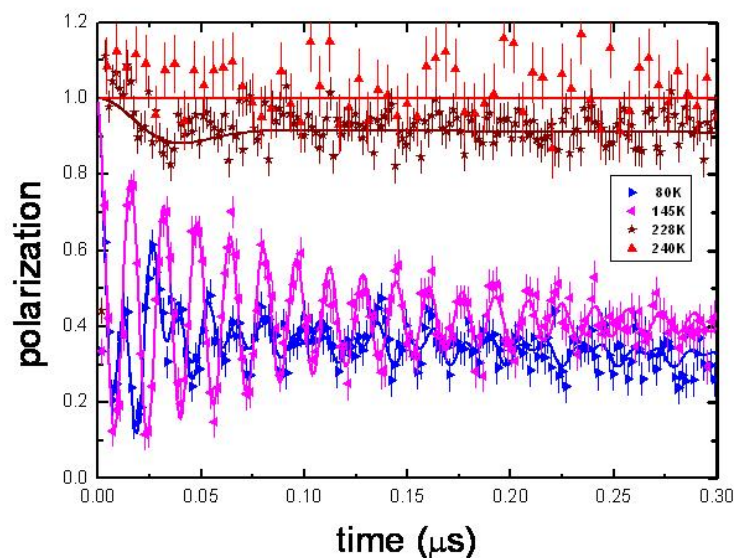
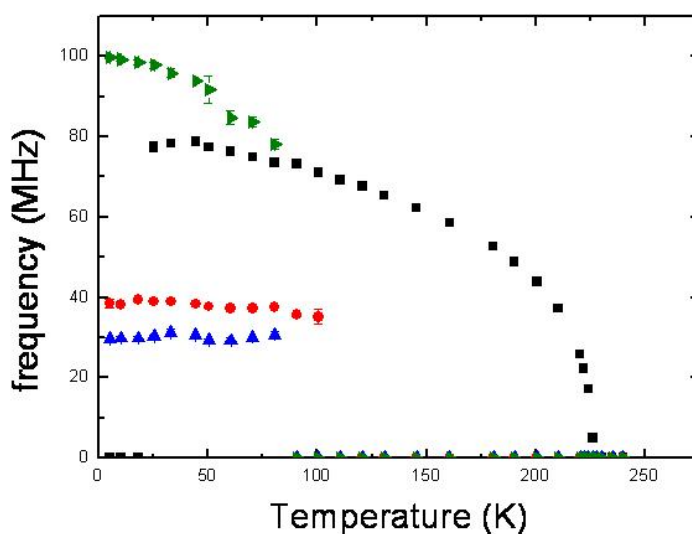Figure 6.10.: Selected ZF-μSR time spectra of $Sr_4Fe_4O_{11}$ at 80K, 145K, 228K and 240K, The data are collected and plotted by Gwendolyne Pascua

Figure 6.11.: Muon-spin precession frequencies as a function of temperature for $Sr_4Fe_4O_{11}$. The data are analyzed and plotted by Gwendolyne Pascua

spin glass-like phase. 2.There is different magnetic structure in the different temperature regimes. A high temperature phase with a commensurate magnetic ordering on the Fe^{3+} sublattice only and low temperature phase where the Fe^{4+} ions also order in a possibly spin-glass like manner. For the Mössbauer spectra at 4.5K, it consists of one Fe^{3+} sextet in addition to an essential paramagnetic Fe^{4+} . As already shown in Table 6.4, a magnetic component instead of a quadrupole doublet is

used for the Fe^{4+} component, which might be frustrated due to the geometry. 3. There might be a crystallographic structural change observed near 90K. We noticed in the PhD thesis of MOYA [84], where they have studied this phase by Mössbauer spectroscopy as a function of temperature. An anomaly in the thermal variation of the paramagnetic fraction in the $Sr_4Fe_4O_{11}$, represented by a doublet in the Mössbauer spectra, are observed in Fig 6.12. There is a clear decrease in the paramagnetic area fraction , or alternatively an increase in the magnetically ordered area fraction by 5% below 100K. This anomaly occurs in the same temperature range where also anomalies in the Seebeck coefficient, μSR and lattice parameter data are seen. A possible origin for the decreased paramagnetic area fraction might be that a minor paramagnetic component, for instance an intermediate valence ($Fe^{+3.5}$) component, undergoes magnetic and charge ordering below 100K. However, there is no convincing evidence for such a fraction from the spectra above 100K. On the other hand, the ratio of the area fractions A of Fe^{4+} and Fe^{3+} sites may be written as:

$$\frac{A(Fe^{4+})}{A(Fe^{3+})} = \frac{f(Fe^{4+}) \cdot \gamma(Fe^{4+})}{f(Fe^{3+}) \cdot \gamma(Fe^{3+})} \tag{6.3}$$

where $\gamma(Fe^{4+})$ and $\gamma(Fe^{3+})$ are the fractions of Fe^{3+} and Fe^{4+} sites, and f(Fe^{4+}) and f(Fe^{3+}) are the Lamb-Mössbauer factors (recoilless free fractions) for the two sites respectively. The area fractions only correspond directly to the fractions of the sites if f(Fe^{4+}) and f(Fe^{3+}) are equal. The Lamb-Mössbauer factors are related to the vibrational properties of the solid. If it is assumed that $\gamma(Fe^{4+})/ \gamma(Fe^{3+}) = 1$ according to the known crystal structure, one obtains f(Fe^{4+}) / f(Fe^{3+}) = 56/(100-56)= 1.27 for T > 100K, and f(Fe^{4+}) / f(Fe^{3+}) = 51/(100-51) = 1.04 for T $\leq$ 50K . The change in the relative Lamb-Mössbauer factors may point to a lattice dynamical origin of the anomalies which is particularly supported by the anomalies in low temperature behavior of the lattice parameters , observed by synchrotron powder diffraction measurement.
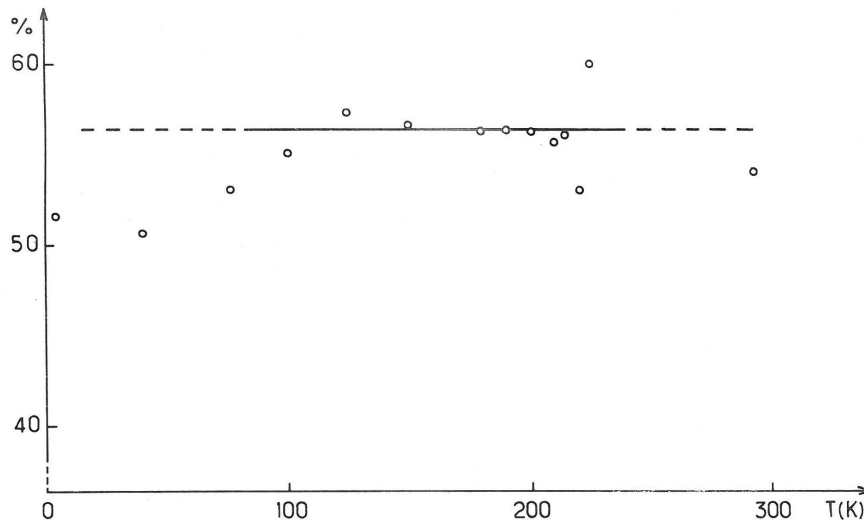

Figure 6.12.: The figure is reproduced from reference[84]. Thermal variation of paramagnetic fraction in the system of $Sr_4Fe_4O_{11}$

In order to further identify one of these assumptions, we analyzed the magnetic volume

fraction change versus temperature. From the Fig 6.13, we observe the total magnetic fraction, which at the edge of Néel transition temperature, only reaches 90% of the sample volume. The magnetic fraction gradually increases with decreasing temperature and reaches 100% only at lowest temperatures. Individual analysis of the amplitude of the different frequencies versus temperature have been plotted and displayed in Fig 6.14 in order to study the magnetic volume fraction evolution versus temperature in detail. We observe that around the Néel transition temperature, approximately 80% volume are statically magnetic ordered on the scale of the muon lifetime while 10% stay in a magnetically disordered state in terms of fast damping. As temperature goes down, magnetically static ordered volume gradually decreasing and the fast damping disordered volume increasing. When temperature across 100K, three new magnetically ordered frequencies appear and take around 35% of the magnetic volume. A detail assignment of the different amplitudes to the various observed frequencies is anyhow difficult and remains unconclusive. However, the new magnetic ordered volume is composed out of commensurate magnetic structures since their polarization curve can all be fitted by Cosine functions. The appearance of the new magnetic fractions occurs at the cost of the high temperature magnetically static ordered phase and the disordered phases. The reason can be seen from Fig 6.14 around 100K the magnetic volume of the new magnetic phases increase abruptly while the magnetic volume of the disordered phases and high temperature static ordered phases decrease. And the sum up of all the magnetic volume fraction is almost constant around 90% of the whole volume.
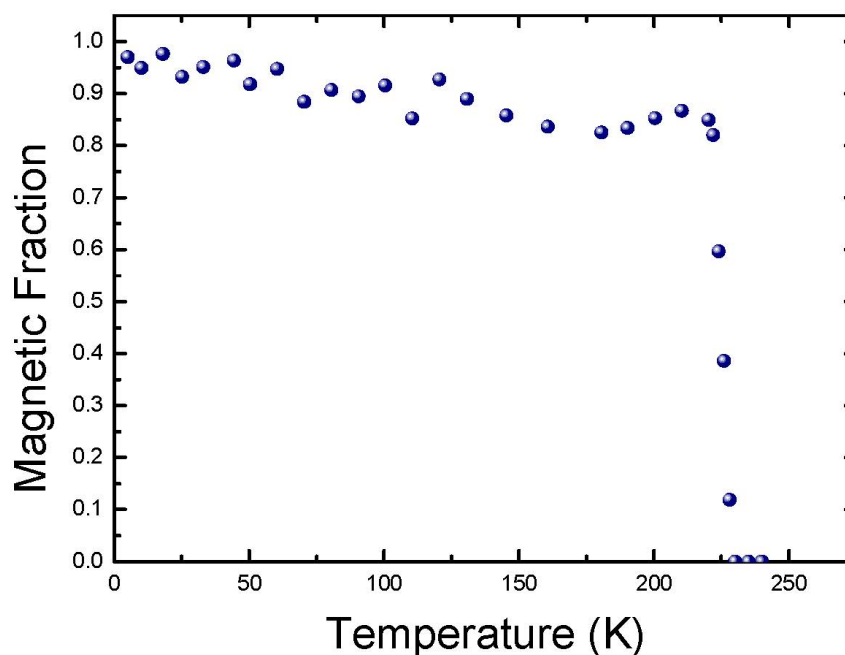

Figure 6.13.: Magnetic fraction sum of all frequencies in the ZF-μSR spectra as a function of temperature for $Sr_4Fe_4O_{11}$. The data are analyzed and plotted by Gwendolyne Pascua

For the description of magnetic interaction that has been expressed in the equation (2.12), it is valid for a single crystal with a single domain and one muon site. In case of polycrystalline magnetic sample, on the average only one third of the muons will sense local magnetic fields
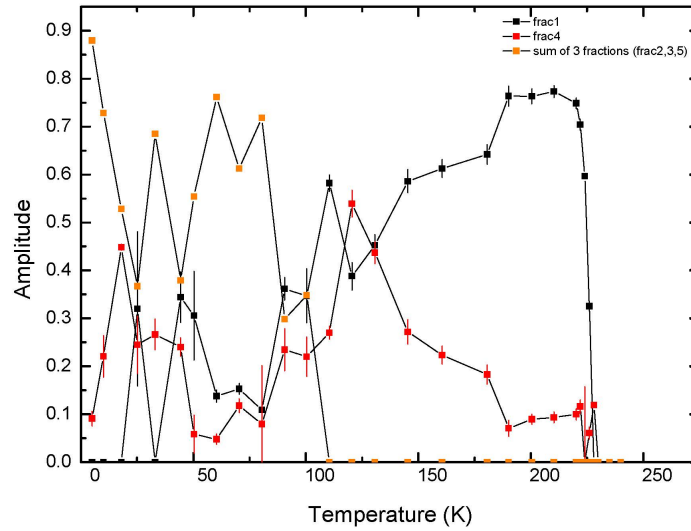
Figure 6.14.: Individual magnetic volume fraction of different frequencies in the ZF-μSR spectra as a function of temperature for $Sr_4Fe_4O_{11}$. The black square of frac 1 corresponds to the frequency appeared around 228K. The red square of frac 4 corresponds to the fast damping. The orange square of the sum of 3 fractions corresponds to the sum up of all frequencies appeared around 100K. The data are analyzed and plotted by Gwendolyne Pascua

parallel to their initial polarization and will not precess while the remaining two thirds of the muons will see local magnetic fields perpendicular to their initial polarization and will precess around them with

$$\omega = \gamma_\mu B$$

. The equation (2.12) becomes (6.4). λ_T is related with the width of the static field distribution at the muon site (the field distribution created by the surrounding ordered moments) and λ_L carry information only about the spin dynamics[86]. Therefore we have fitted the data for the whole temperature regions with the equation (6.4) and plotted the dynamic relaxation in Fig 6.15. We see from this figure that there are two peaks in the whole temperature region. One is at T_N = 228K, the system changes from paramagnetic phase into antiferromagnetic phase.While another peak is around 80K where four new frequencies appeared. This is a typical signature of critical spin fluctuation slowing down as e.g.observed in $Y_2Mo_2O_7$ and $Tb_2Mo_2O_7$[87]. Note that the dynamic relaxation rate λ_L is related to but not directly the magnetic fluctuation rate.

$$P(t) = [\frac{2}{3}e^{-\lambda_T t}\cos(2\pi f t) + \frac{1}{3}e^{-\lambda_L t}] \tag{6.4}$$

6.4. Conclusion

From the Seebeck coefficient, resistivity, and magnetization measurements, and by comparing the results from the two batches of samples with different oxygen stoichiometry, we stress
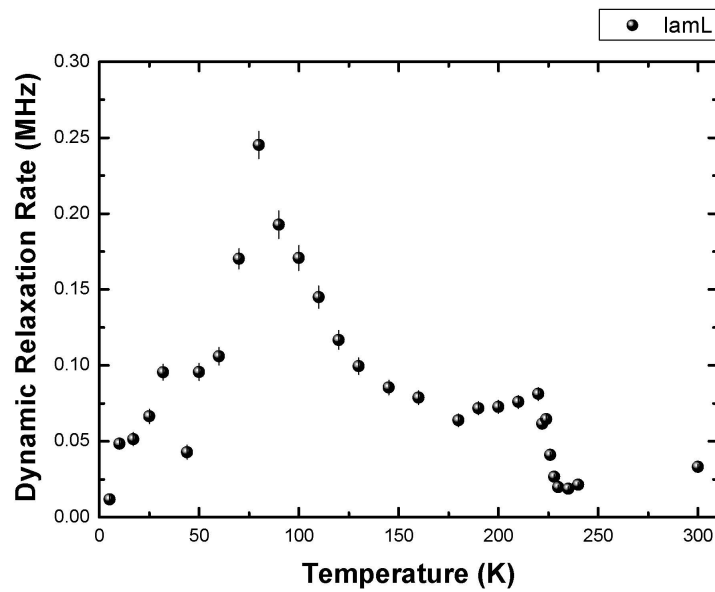
Figure 6.15.: Dynamic relaxation rate versus temperature in the ZF-μSR spectra of $Sr_4Fe_4O_{11}$. The data are analyzed and plotted by Gwendolyne Pascua

the extreme sensitivity of the physical properties to the oxygen stoichiometry in $SrFeO_{3-x}$. Comparing to previous work, we conclude that the sample that has been prepared in this thesis is more close to the ideal $Sr_4Fe_4O_{11}$ phase than any of the reported samples. A new magnetic transition has been found in our sample in μSR measurements (in line with the recent published neutron measurement [72]) around 90 K. Based on the detailed analysis of μSR results and Mössbauer results, one possible explanation for this transition may be found in the spin-lattice coupled dynamics

Chapter 7.

X-ray absorption and Photoemission study of $Sr_4Fe_4O_{11}$

The relationship between the crystal structure and the magnetic and electronic behavior is of great interest to condensed matter scientists. For example, the transition-metal perovskites $LaMnO_3$, $SrFeO_3$, and $CaFeO_3$ have the high spin $d^4(t_{2g}^3 e_g^1)$ configuration with orbital degeneracy. Remarkably, only $LaMnO_3$ shows a cooperative Jahn-Teller distortion of the MnO_6 octahedra, while $SrFeO_3$ keeps a cubic structure down to 4K due to strong covalency between Fe-O bonds; $CaFeO_3$ displays structural transformation together with metal-insulator transition, exhibiting charge disproportionation at low temperature. These interesting behaviors of the transition metal oxides inspire the researchers to put a lot of effort on revealing the mystery of the relationship between the electronic properties and crystal structure.

$Sr_4Fe_4O_{11}$ has two crystallographic distinct Fe sites, which form octahedral chains cross linked by dimers of pyramidal sites. The Fe valence is expected to be mixed Fe^{4+} and Fe^{3+}, in equal amounts. An important starting point to understand the relationship between crystal structure and the electronic and magnetic properties, is to clarify a possible charge order and to assign the valence states to their respective crystallographic sites. Hodges et al.[13] concluded from bond valence sum calculations that the Fe^{4+} sites reside in the pyramidal site and the Fe^{3+} sites in the octahedral sites. Schmidt et al. [44] criticized this assignment and favored the opposite distribution of charge states, Fe^{3+} in the pyramidal site and Fe^{4+} in the octahedral sites. Adler et al. [15, 17], however, by comparing the bond length and Mössbauer spectra, found further support for the scenario of Hodges et al. Vidya et al.[16, 18] investigated the structural, electronic, and magnetic properties of $Sr_4Fe_4O_{11}$ by spin-polarized electronic-structure calculations and concluded that iron atoms with the square pyramidal enviroment have a lower oxidation state. This controversy is still unsolved yet. We have used x-ray absorption and resonant photoelectron spectroscopy to gain insight into the electronic structure. These techniques are charge and symmetry sensitive, and thus a valuable tool to gather further information on the charge states of Fe.

7.1. Preparation of the reference samples

In order to study the influence of coordination and valences to the spectra, different compounds have been prepared as reference samples. There are $SrFeO_3$ with pure Fe^{4+} in octahedral coordination and $LaFeO_3$ with pure Fe^{3+} in octahedral coordination; $Sr_3Fe_2O_6$, having pure Fe^{3+} in pyramidal coordination, is a separate topic in this thesis(see Chapter 3); Here it is used as a reference. $SrFeO_3$ has been prepared under high oxygen pressure. The as-synthesized $Sr_2Fe_2O_5$,which is prepared in Chapter 4, is put into high pressure oxygen furnace under 340atm pure oxygen and sintered at 823K for 72h. The magnetization measurement shows

clearly two transition at 130K and 60K , corresponding to the helical order of cubic phase and spin reorientation in the heical phase respectively. No extra transition exist, proving the good stoichiometry of $SrFeO_3$. The $LaFeO_3$ has been prepared by solid state reaction, starting from La_2O_3 (Alfa Aesar Ref:41644) and Fe_2O_3 (Sterm Chemicals Ref:933803) with purities of 99.9% and 99.99% , respectively. The La_2O_3 is preheated under 950°C overnight to remove the absorbed water, then the mass is weighted directly according to the stoichiometry. The mixture of these two reactants are ground with ethanol for 30 mins and dried in the air under a hood. Then the dried powder is heated up to 1300°C overnight and quenched to room temperature, and then ground again. These processes are repeated several times until the x-ray diffraction pattern shows the purity phase as displayed in Fig. 7.2. A full powder-pattern-profile refinement (le Bail fit through the Fullprof software) has been performed within the Pbnm space group. There are no extra peaks in the diffraction pattern, confirming the purity of the phase. Thompson-Cox-Hastings pseudo-Voigt is used for the peak shape. The refined unit-cell parameters are $a = 5.55465(1)$Å, $b = 5.56657(1)$Å and $c = 7.85512$Å, in good accordance with previously published values [75]. The Mössbauer spectrum of $LaFeO_3$ is shown in Fig. 7.3, there is a single magnetic hyperfine sextet splitting observed for Fe^{3+}, confirming the good stoichiometry of the sample. The parameters from the Mössbauer spectrum evaluation are listed in Table. 7.1.
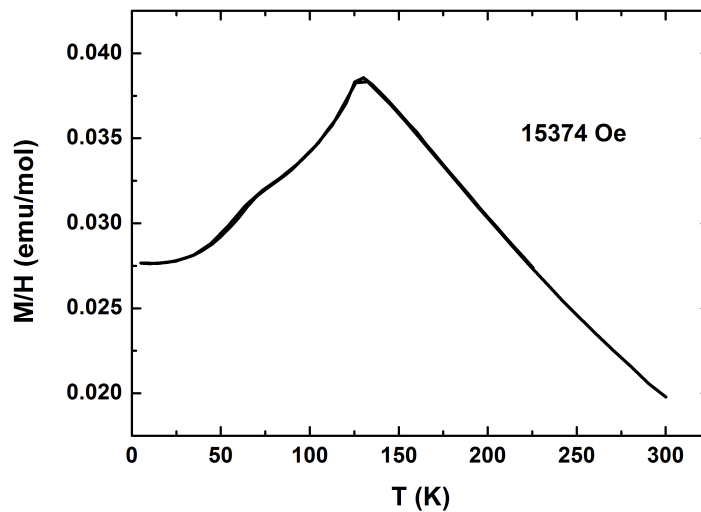

Figure 7.1.: Plot of Field-cooled M/H data at 15374Oe from $SrFeO_3$

Site	δ(mm/s)	Δ(mm/s)	ε(mm/s)	B_{hf}(T)	%
1	0.372	0.280	-0.03	52.3	100

Table 7.1.: Mössbauer analysis parameters for $LaFeO_3$. δ is the isomer shift, Δ is the quadrupole splitting, ε is the quadrupole interaction in the magnetically ordered phase, B_{hf}(T) is the magnetic hyperfine field.
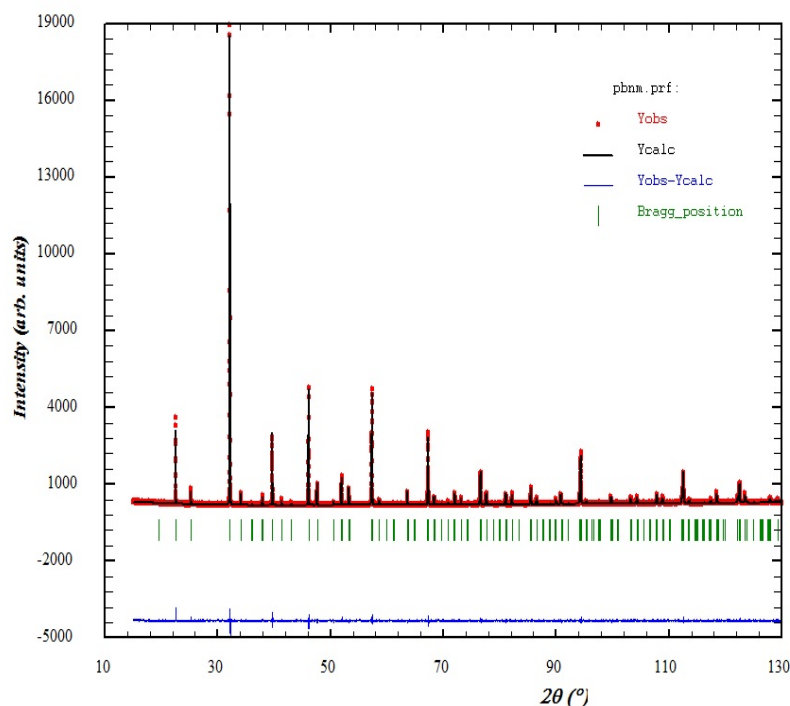
Figure 7.2: X-ray powder diffraction pattern of LaFeO$_3$; Black circles: measured data I$_{obs}$; Green bars: peak positions of the nuclear peaks; Red lines: Calculated fitting (I$_{calc}$); Blue line: the difference between calculated fitting and measured data (I$_{calc}$-I$_{obs}$).
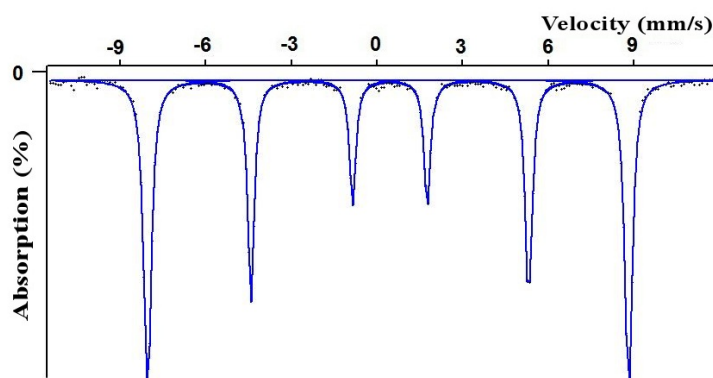

Figure 7.3.: ^{57}Fe Mössbauer spectrum of LaFeO$_3$

7.2. XAS of Fe^{4+} and Fe^{3+} in different coordination

In order to check the valence and the coordination of Sr$_4$Fe$_4$O$_{11}$, we have done x-ray absorption spectroscopy. Fig. 7.4 depicts Fe-$L_{2,3}$ edge XAS spectra of Sr$_3$Fe$_2$O$_6$, Sr$_4$Fe$_4$O$_{11}$, SrFeO$_3$, and LaFeO$_3$. There are two main features in the spectra, namely L_3 in the energy range of 706-714 eV and L_2 in the energy range of 720-726 eV. The spin-orbit coupling of the Fe $2p$ core hole gives rise to the largest splitting in the whole spectra, and the the L_3 and L_2 features are related
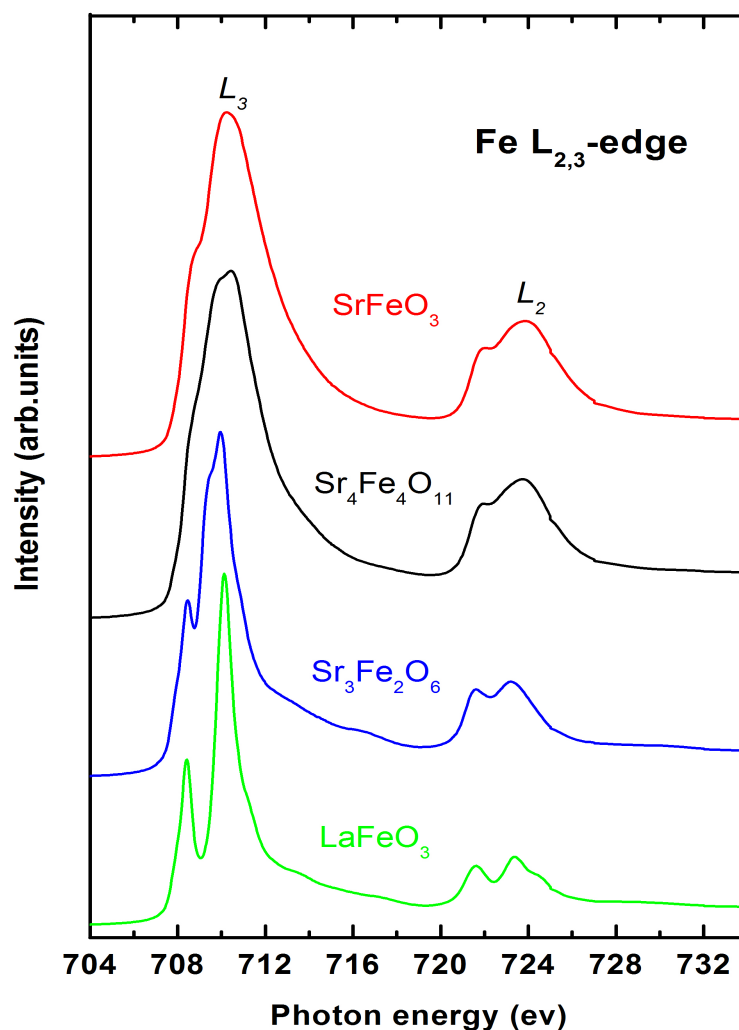
Figure 7.4.: Fe $L_{2,3}$-edge XAS spectra of $Sr_3Fe_2O_6$, $Sr_4Fe_4O_{11}$, $SrFe_{0.5}Co_{0.5}O_3$ and $LaFeO_3$.

to the $2p_{3/2}$ and $2p_{1/2}$ core holes in the final states, respectively. The line shape strongly depends on the multiplet structure given by the Fe $3d$-$3d$ and $2p$-$3d$ Coulomb interactions, as well as by the local crystal fields and the hybridization with the O $2p$ ligands. Unique to soft XAS is that the dipole selection rules are very sensitive in determining which of the $2p^5 3d^{n+1}$ final states can be reached and with what intensity, starting from a particular $2p^6 3d^n$ initial state (n=4 for Fe^{4+} and n=5 for Fe^{3+})[60, 88]. This makes the technique extremely sensitive to the symmetry of the initial state, i.e., valence states, the crystal-field states of the ions. By comparison of the fine structures (the energy positions and the line shape) in the spectra, we are able to distinguish between Fe^{4+} and Fe^{3+} valence state. The main peak position of Fe $L_{2,3}$ edge of Fe^{3+} in $LaFeO_3$ and $Sr_3Fe_2O_6$ are about 0.5 eV lower than the main peak position of Fe^{4+} in $SrFeO_3$. It is

well known that an increase in the valence state of the $3d$ transition metal ion causes a shift of its XAS $L_{2,3}$ spectra toward higher energies[30, 57, 89]. The main feature of Fe-L_3 (706-714 eV) of $Sr_4Fe_4O_{11}$ lie at similar energies as that of polycrystalline $LaFeO_3$ and $Sr_3Fe_2O_6$ as pure Fe^{3+} references and $SrFeO_3$ as pure Fe^{4+} reference. This indicates the mixed valence state of Fe^{3+} and Fe^{4+} in $Sr_4Fe_4O_{11}$. The differences in the line shape and the energy shift between $LaFeO_3$ and $Sr_3Fe_2O_6$ can be attributed to the symmetry of the crystal field. $LaFeO_3$ has an octahedral coordination with a t_{2g}-e_g splitting similar as in Fe_2O_3 [30]. The coordination in $Sr_3Fe_2O_6$ is pyramidal, and in comparison to octahedral coordination, the missing of one of the apical oxygens lowers the energy of the $3d_{z^2-r^2}$ crystal field level in respect to the $d_{x^2-y^2}$ level. The detailed explanation is given by the full-multiplet calculations and the resulting crystal field splitting energy diagram in Chapter 3.

Fig. 7.5 depicts the oxygen K-edge XAS spectra of $Sr_3Fe_2O_6$, $Sr_4Fe_4O_{11}$ and $LaFeO_3$. The oxygen K-edge x-ray absorption spectrum is arising from the excitation process of an electron from the $1s$ shell to the $2p$ shell, creating one core hole in the $1s$ shell. The formally filled $2p$ shells of the O^{2-} ions are hybridized with the $Fe3d$ shell, leaving the $2p$ shells partially empty. Since there is no spin-orbital coupling in the $1s$ shell core hole, the oxygen K-edge XAS can be compared to the character of the conduction band in these compounds. The pre-edge peak features of the oxygen K-edge (526-532 eV), shown in Fig. 7.5, come from the $O2p$-$Fe3d$ hybridization. This main peak position of oxygen K-edge in $LaFeO_3$ is about 1.5 eV higher than the one in $Sr_4Fe_4O_{11}$. This energy shift is in contrast to the energy shift in the Fe $L_{2,3}$ edge [30, 57, 89]. The broad rising features above 532eV corresponds to Sr $4d$ band region for $Sr_3Fe_2O_6$ and $Sr_4Fe_4O_{11}$ or La $5d$ band region for $LaFeO_3$ and for even higher energy the Fe $4sp$ band region appears[90]. The differences in the line shape and the energy shift between $LaFeO_3$ and $Sr_3Fe_2O_6$ can also be attributed to the crystal field symmetry .

7.3. PES of single crystal $Sr_4Fe_4O_{11}$

Photoelectron spectroscopy (PES) is a powerful tool to investigate the electronic structure of solids. We have performed PES for the valence band of $Sr_4Fe_4O_{11}$. The experimental set-up is described in Chapter 2. Two photon energies (100 eV and 600 eV) are chosen as the incident photon energies. The photoionization cross sections are photon energy dependent. The spectral weight of a specific element or orbital changes with the photon energy. The tendency is that higher photon energy have lower cross sections. For transition metal oxides, the cross section of O $2p$ shell decreases faster toward higher photon energies than the cross section for the transition metal $3d$ shell. The transition metal $3d$ shell photoemission becomes relatively more dominant [91, 92]and the optimized cross section range of the transition metal oxides are around 600eV to 700eV. Here the transition metal $3d$ shell are most pronounced compared to O $2p$ shell. The PES detects escaped electrons from the surface and the escape depth of the photo electron is changing as a function of photon energy, which is given by the so-called universal curve. The escape depth of the electrons is determined by electron-electron and electron-phonon collisions. Thus, it is also strongly dependent on the electronic and crystal structure of the system. In the soft x-ray range, one can see that the escape depth in the universal curve is only of the order of a few Å. Hence, we are probing electronic states in the surface region of a sample, and the probing depth
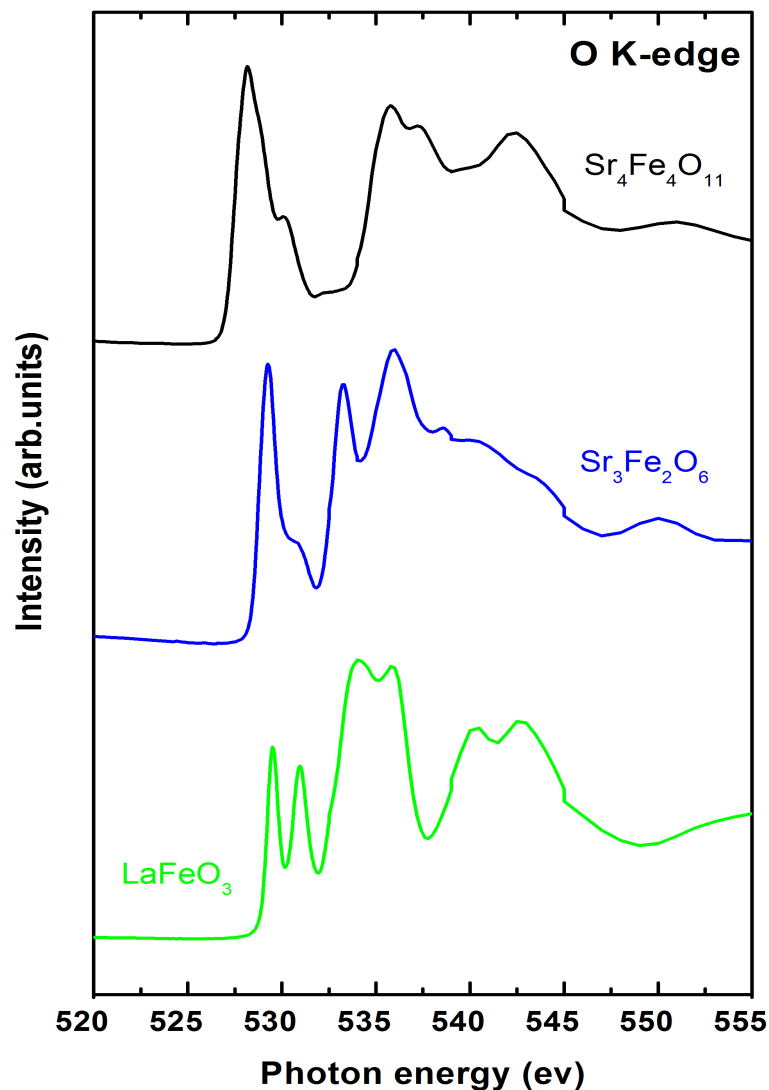
Figure 7.5.: Oxygen K-edge XAS spectra of $Sr_3Fe_2O_6$, $Sr_4Fe_4O_{11}$ and $LaFeO_3$.

increases when changing from 100 eV to 600 eV photons. However, 100 eV photon energy is still used in this thesis because of its higher intensity in the spectra and better resolution in our setup. This has advantage to resolve more detailed information of the spectrum e.g., states near the Fermi energy and the size of the gap from the occupied states to the chemical potential.

The spectra are taken at 260 K with 600 eV and 100 eV photon energy are shown in Figure. 7.6. The PES of polycrystalline Ag is also presented here as a reference for the Fermi energy.

The valence band photoemission spectra are sensitive to the Fe $3d$ and O $2p$ shells, which are close to the Fermi level in the valence band. The structure at 0-7 eV arise from the hybridization of the Fe $3d$-O $2p$ bands. A small satellite located at 7-9eV may come from contamination of the surface [5, 93]. Configuration-interaction cluster calculations [5] found that the main band of
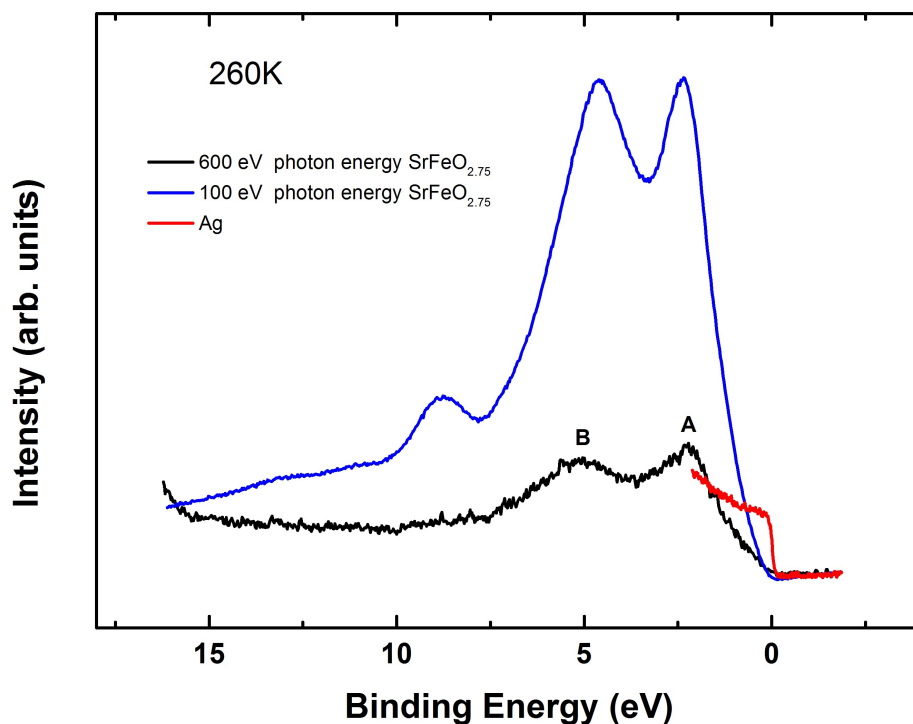
Figure 7.6.: Valence band photoemission spectra of cleaved $Sr_4Fe_4O_{11}$ single crystal with 600eV photon energy (black), with 100eV photon energy (blue) and of Ag (red) for energy calibration taken at 260 K at normal emission.

Fe^{3+} arises from screened $d^5\underline{L}$ final states and the main band of Fe^{4+} is $d^5\underline{L}^2$-like. The shape of the spectra are slowly decreasing, where the binding energy approaches to zero, without a clear Fermi cut-off , indicating the sample is a semi-conductor, but we can't give a precise energy value as a band gap for the occupied states. Comparing the experimental spectrum with the band structure calculation [16] for the density of states of $Sr_4Fe_4O_{11}$ in the ground-state G-AF configuration (Fig. 7.7), we can observe a general agreement. The two main features A and B in the spectra of 600eV incident photon energy, arising from two bands of hybridized Fe$3d$ and O$2p$ [16], are reproduced in the DOS. And the rather small bandgap of 0.13eV that predicted from the calculation are in terms with our experimental observation.

7.4. RESPES of single crystal $Sr_4Fe_4O_{11}$

In order to study in detail the Fe $3d$ contributions to the valence band in $Sr_4Fe_4O_{11}$, we have performed additional valence band resonant photoemission at the Fe $2p$ excitation (L_3 edge). The advantage of resonant photoemission is that we can extract the contribution of the transition metal $3d$ to the valence band by choosing the photon energy to coincide with the transition metal core level absorption e.g., the Fe L_3 edge. The intensity of the photoemission will be enhanced
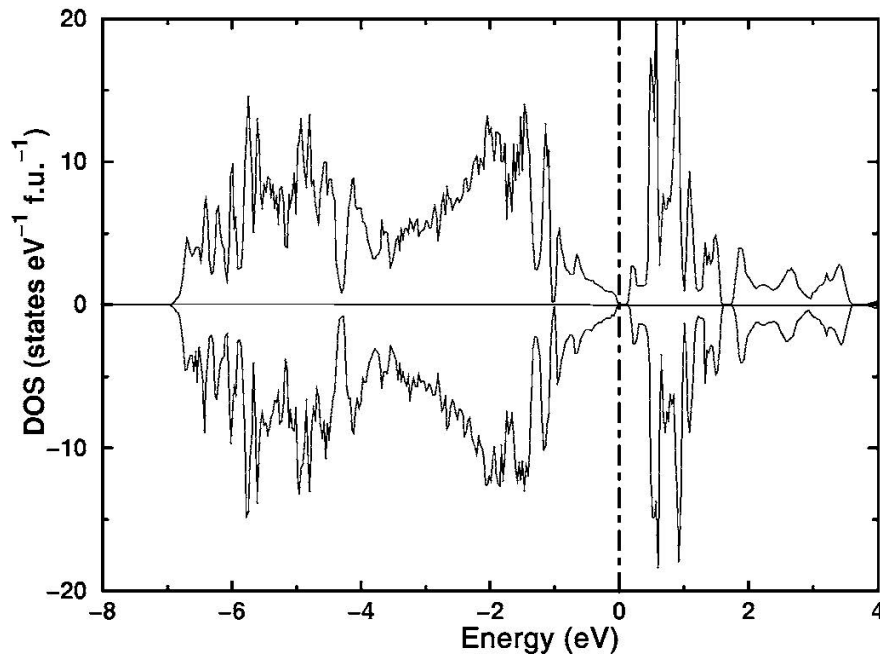
Figure 7.7.: The picture is reproduced from Ref[16].Calulated total density of states (DOS) for $Sr_4Fe_4O_{11}$ in the ground-state G-AF configuration. The Fermi level is set to zero.

when the incident photon energy resonates with a core-electron excitation threshold. As the absorption process is sensitive to the element and charge , the corresponding part of resonant PES spectra will also be charge-sensitive in respect to the incident photon energy. The resulting spectra are shown in Fig. 7.9 and Fig. 7.10. The corresponding resonant photon energies are chosen according to the Fe L_3 edge XAS spectra, shown in Fig. 7.8. The arrows in this figure indicate the photon energies chosen for the resonant measurement. A non-resonant photon energy at 690eV, far below the Fe L_3 edge, is also chosen as a reference. The corresponding photoemission spectrum of this non-resonant photon energy, as incident photon energy, is similar to the valence band PES spectrum described in the previous section, indicating the consistency of the data . Aiming to unravel the Fe^{3+} and Fe^{4+} contribution to the valence band, we have made use of the valence dependence of the resonance energy, as in XAS, chosen the other resonant photon energies specifically. As the spectra of higher valence transition metal appears at higher photon energies [30, 94], we expect the low-energy shoulder of the L_3 white line at 709.2eV is due to predominantly the Fe^{3+} while the higher energy peak at 709.84eV comes from the Fe^{4+} . Besides, we have chosen several photon energies along L_3 edge to follow the changes in the PES spectra.

In resonant PES, often a feature related to the Auger decay is observed. The kinetic energy of Auger electrons is only depending on the type of atom and the chemical environment; Thus, it is independent of the photon energy. We have plot the PES as a function of kinetic energy Fig. 7.9. A black straight line indicates a feature with constant kinetic energy, independent of the incident photon energy, which is assumed to be an Auger line ($\approx$ 697.3 eV). The valence band Resonant PES as a function of binding energy is given in Fig. 7.10. The intensity of the features close to
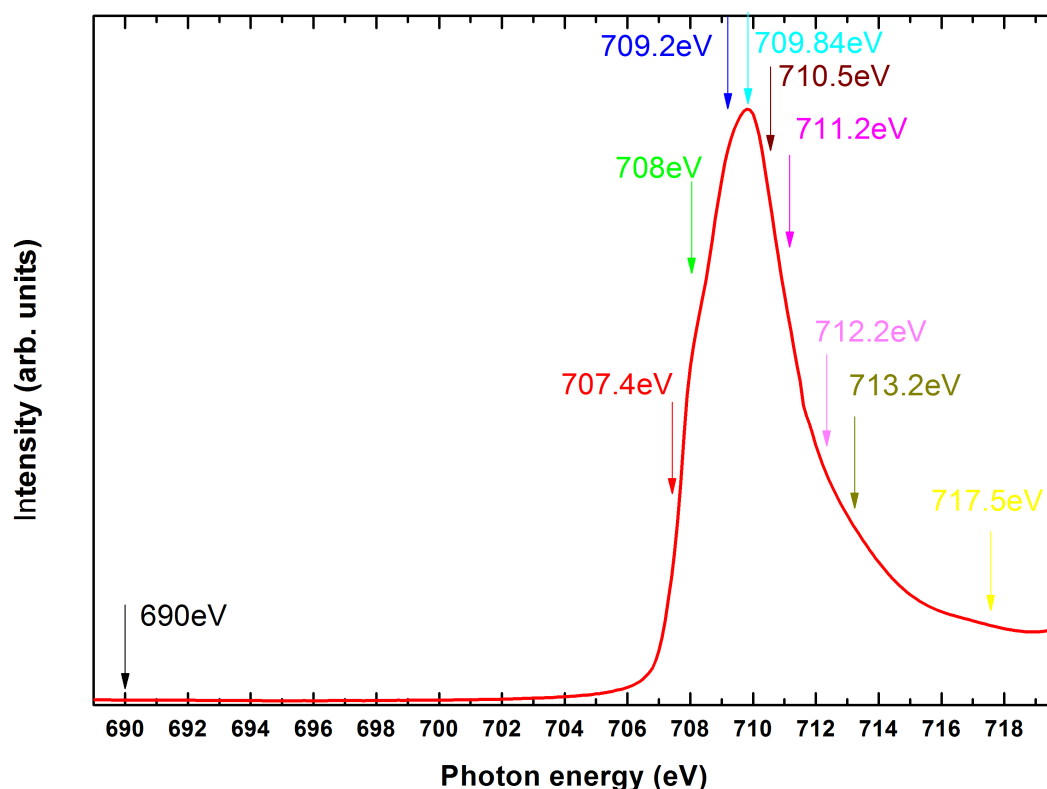
Figure 7.8.: Fe L_3 edge of $Sr_4Fe_4O_{11}$ single crystal, the arrows indicate the photon energy being used in RePES.

the Fermi level are changing strongly with different resonant photon energies. This indicates that Fe $3d$-related features are indeed located close to the Fermi edge. A pit appears next to the prepeak below the Fermi energy around 4 eV (illustrated by a black arrow at the bottom of the figure). It does not change with the resonant photon energy and could be attributed to the features of the O $2p$ band. Comparing the differences of these resonant photoemission spectra, we notice that when resonant energy change from 709.2 eV (Fe^{3+} dominating) to 709.8 eV (Fe^{4+} dominating), the spectra also show clear changes. This can be attributed to the Fe^{3+} contribution to the spectra has decreased and the Fe^{4+} contribution has increased. More clearly observation can be seen when the incident photon energy is at 710.5eV. The blue arrows and black arrows in Figure. 7.10 indicate the contribution of the spectra to which we assign predominantly Fe^{3+} and Fe^{4+} character, respectively.

7.5. Conclusion

The electronic structure of $Sr_4Fe_4O_{11}$ has been investigated with x-ray absorption spectroscopy and photoelectron spectroscopy. In comparison with the reference samples ($Sr_3Fe_2O_6$ for Fe^{3+} in pyramidal coordination, $SrFeO_3$ for Fe^{4+} in octahedra coordination, $LaFeO_3$ for Fe^{3+} in octahedral coordination), the Fe-$L_{2,3}$ edge of $Sr_4Fe_4O_{11}$ sample have the features belonging to

Figure 7.9.: Valence band ReSPES of cleaved $Sr_4Fe_4O_{11}$ single crystal at Fe L_3 resonance as a function of kinetic energy, T=260K. The black straight line indicate Auger decay

Fe^{3+} and Fe^{4+}, and their ratio can be confirmed to be 1:1. Concerning the charge order, however, the present data are not sufficient. In a linear dichroism experiment on the Fe-$L_{2,3}$ edge on the single crystal of $Sr_4Fe_4O_{11}$, probably the site symmetry of Fe^{3+} and Fe^{4+} could be distinguished. Such an experiment is planned as future work. In the Fe $L_{2,3}$ edge spectra, Photoelectron spectra show the compound is a semiconductor. Resonant photoelectron spectroscopy unravels the contributions of Fe^{3+} and Fe^{4+} to the valence band of the single crystal $Sr_4Fe_4O_{11}$ close to the Fermi energy.
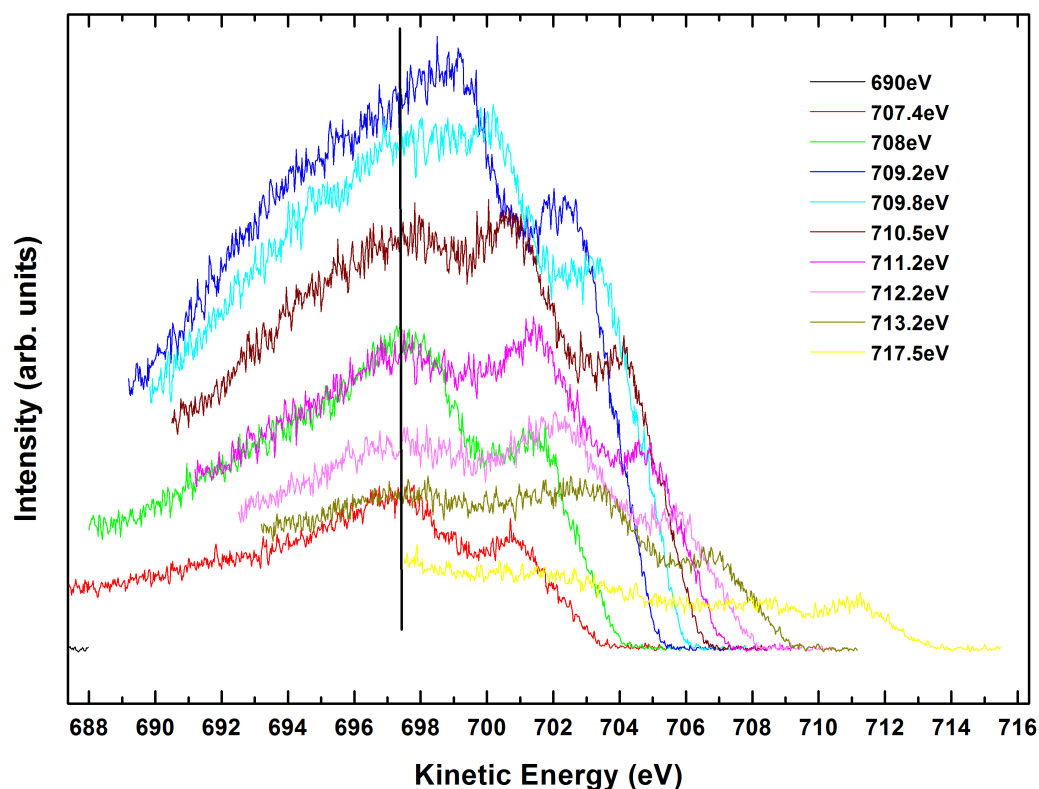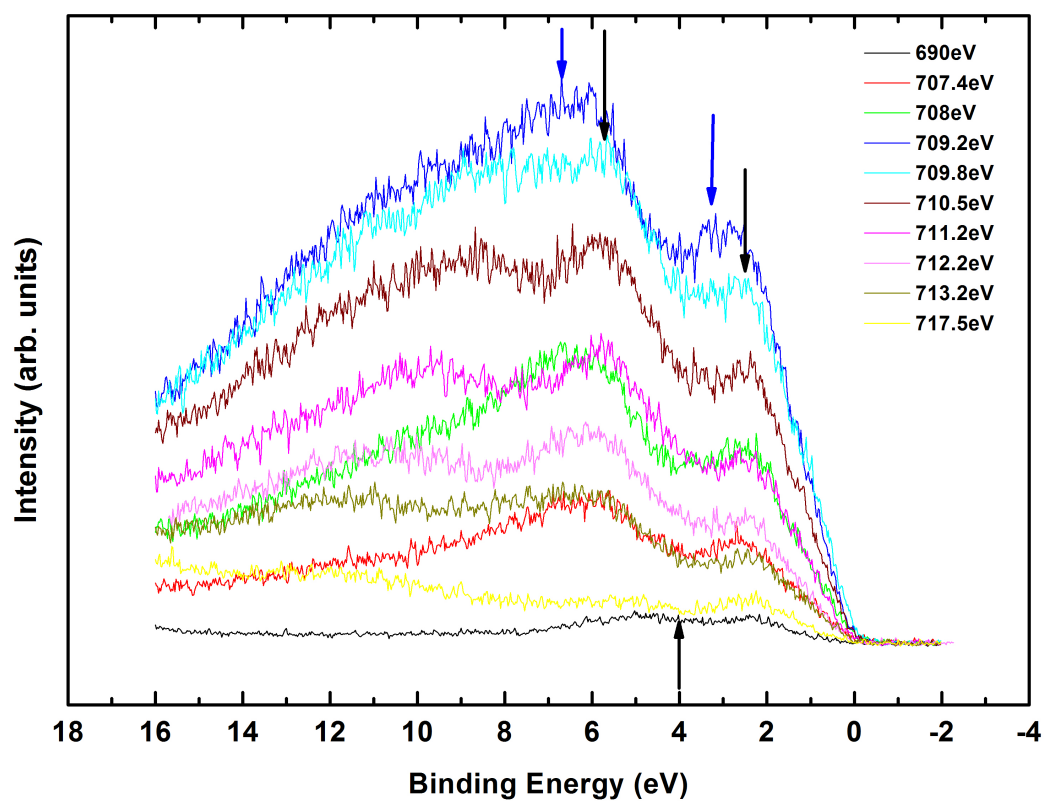
Figure 7.10.: Valence band ReSPES of cleaved $Sr_4Fe_4O_{11}$ single crystal at Fe L_3 resonance as a function of binding energy, T=260K. The blue arrows indicated the Fe^{3+} contribution and the black arrows indicated the Fe^{4+} contribution.

Chapter 8.

Synthesis, characterization and electronic structure of SrFeO$_2$

8.1. Synthesis of SrFeO$_2$

The starting materials for preparing SrFeO$_2$ are SrFeO$_{3-x}$ and CaH$_2$ with 99.9% purity from Sigma-Aldrich Ref.558257. The synthesis of SrFeO$_{3-x}$ was described in details in Section 5.1. The synthetic route is based on the published work[19]. SrFeO$_{3-x}$ (x≈0.18)(0.45g) and approximately two-molar excess of CaH$_2$ (0.2g) are mixed and ground in an argon glove box, pressed into pellet and sealed in an evacuated quartz tube with pressure around 5×10^{-4} bar. The sealed tube is then put into a furnace at 575K for 72 hours and quench into air. The residual CaH$_2$ and the CaO byproducts are removed from the final powder by washing them out with 0.1M NH$_4$Cl in methanol solution.

8.2. Nuclear structure of SrFeO$_2$

The reported crystal structure of SrFeO$_2$ is tetragonal (P/4mmm space group) with unit cell parameters a=3.99107(3)Å and c=3.47481(5)Å[19], see Figure 8.1. The Fe^{2+} is coordinated by four oxygens in a square-planar site, which is isostructural with "infinite layer" SrCuO$_2$. And the spin structure is the (π, π, π) antiferromagnetic order with Néel temperature T$_N$= 473K[19]. Despite of the existence of Fe^{2+}, the compound SrFeO$_2$ is reported to be stable and the structure can persist at least up to 960K[6].

The as-synthesized sample has been checked by powder X-ray diffraction on a HUBER G670 imaging plate Guinier camera with Co K(α1) radiation (λ = 1.78919 Å, 2θ interval of 3.5° - 100.5°). The data has been refined with Fullprof-suite software. Initial structure model P4/mmm has been used for indexing the powder diffraction pattern. During the refinement the Pseudo-Voigt function is used for the peak shape. The background is refined with a linear interpolation of N selected points. An excellent fit between the observed diffraction data and calculated profile is obtained and listed in Fig 8.2. The lattice constant a= b= 3.9900(0)Å, c=3.47598(3)Å in accordance with the previous reported values. And there is no impurity phase within the detectable range of the diffractometer.

8.3. Mössbauer spectra of SrFeO$_2$

The Mössbauer spectra are shown in Fig 8.3, and the fitting parameters are listed in Table 8.1. The spectra are composed of a majority magnetic component with a sextet and a second non magnetically ordered component described by a quadrupole doublet. The isomer shift and the
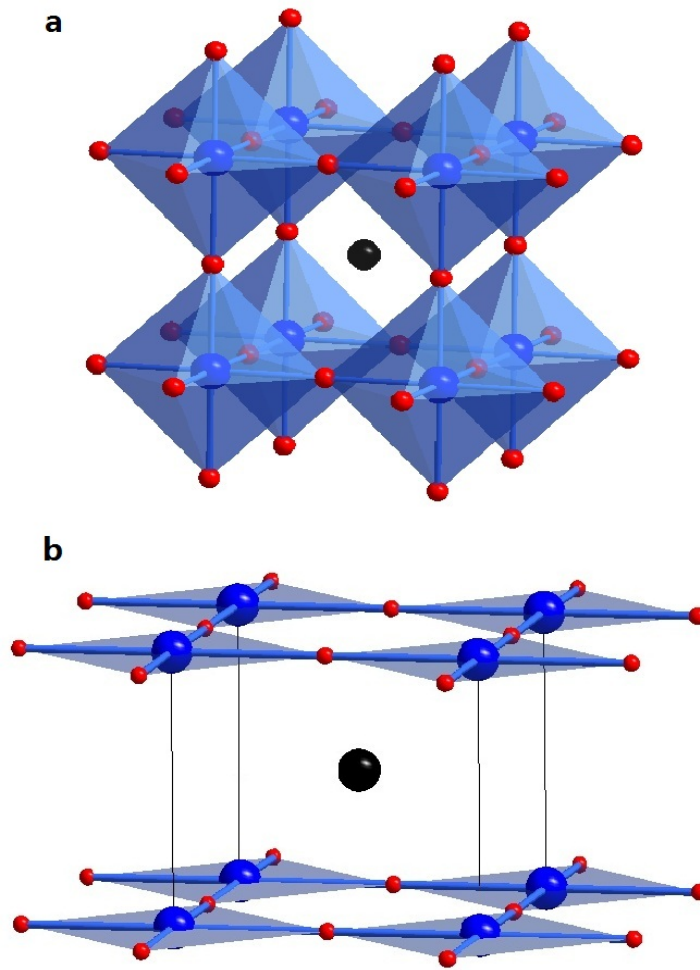
Figure 8.1.: Structural transformation via a topotactic route[19]. a. The cubic perovskite SrFeO$_3$. b. The infinite-layer compound SrFeO$_2$. Iron, strontium and oxygen atoms are represented as blue, black and red spheres, respectively.

magnetic hyperfine field (B$_{hf}$) from our measurement are close to the previous work[19]. In the sextet the line separation S2 of the last two lines is different from the separation S1 of the first two lines (Figure 8.3). This evidences the presence of combined magnetic and quadrupole interaction, as expected for a tetragonal crystal structure. In this structure the EFG is axially symmetric. As Δ E$_Q \ll$ B$_{hf}$ ($\sim$ 1 mms^{-1} vs $\sim$ 12 mms^{-1}), one can describe the quadrupole interaction by a parameter : $\varepsilon = \frac{eQV_{zz}}{4}\left(\frac{3\cos^2\theta-1}{2}\right)$, where V_{zz} is the principal component of the EFG and θ is the angle between the principle axis of the EFG and the direction of B$_{hf}$. For SrFeO$_2$, it is observed in the previous work that the principle axis of the EFG is parallel to the c-axis and perpendicular to the direction of B$_{hf}$[19]. Thus the quadrupole interaction parameter can be expressed as :

$$\mid \varepsilon \mid = \mid \frac{eQV_{zz}}{4} \times (-1/2) \mid = \frac{1}{4}\Delta E_Q = \frac{1}{4}\mid(S_2 - S_1)\mid$$
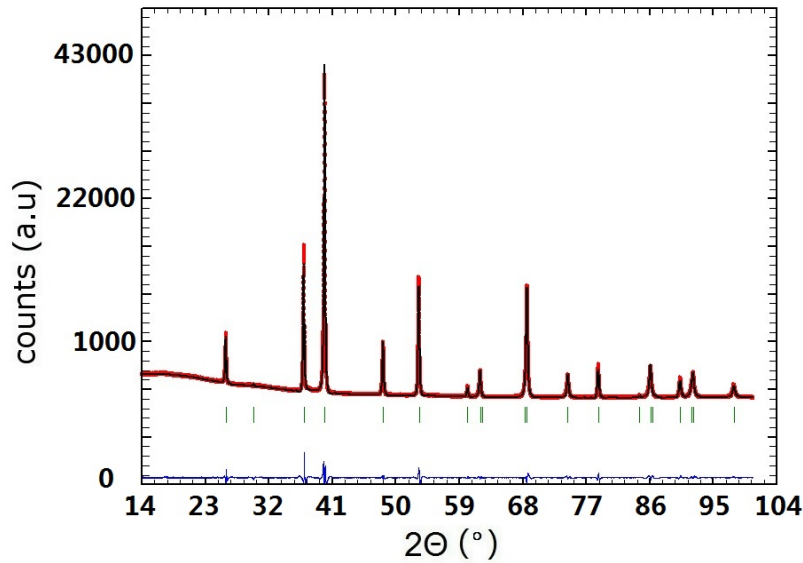
Figure 8.2.: The Le bail refinement of X-ray diffraction of the SrFeO$_2$. Black circles: measured data I$_{obs}$; Green bars: peak positions of the nuclear peaks; Red lines: Calculated fitting (I$_{calc}$). R$_P$= 1.70, R$_{WP}$ = 3.05, Chi2=3.59

here ΔE$_Q$ is the quadrupole splitting corresponding to the spectra of the paramagnetic phase. The observed quadrupole splitting of SrFeO$_2$ in the paramagnetic phase is 1.085 mms^{-1} at 473K[19], which is quite similar to ΔE$_Q$ at room temperature. The present value of ε = - 0.3mms^{-1} corresponds to ΔE$_Q$ = $|4\varepsilon|$ = 1.2mms^{-1}, which is in reasonable agreement with ΔE$_Q$ = 1.16mms^{-1} from Ref[19]. It is obvious that ε and therefore V$_{zz}$ is negative as S$_2$ < S$_1$.

When we heat the sample up to 400K under 10^{-10} bar vacuum and cool down to room temperature, the Mössbauer spectra of SrFeO$_2$ does not change much. It remains one magnetic component and another non magnetic component. But the quadrupole splitting of the quadrupole doublet has decreased from 0.681 mm/s to 0.3 mm/s. This non magnetic component may come from an impurity phase or from the phenomenon of superparamagnetism. In order to test these possibilities , we perform the low temperature measurement using a cryostat at 4.2K . The non magnetic component has disappeared completely, and the magnetic hyperfine field B$_{hf}$ of the majority component has increased from 39T to 46T which is in good agreement with the previous published work [19] on the magnetic hyperfine field, see Fig 8.6. The magnetic hyperfine field of the majority component increase with decreasing temperature , reflecting the ordered magnetic moments in SrFeO$_2$ increasing with decreasing temperature. For the non-magnetic component in our sample, its quadrupole splitting is very different between room temperature and low temperature. At 4.2K, the non magnetic component disappear and the fraction of magnetic impurity sites (indicated by arrows) appear to be increased . Thus, the tiny non magnetic component probably corresponds to an impurity which has smaller ordering temperature than that of SrFeO$_2$. It might be the not fully reduced SrFeO$_{3-X}$ phase and is not observable within the errors of our X-ray diffraction pattern.
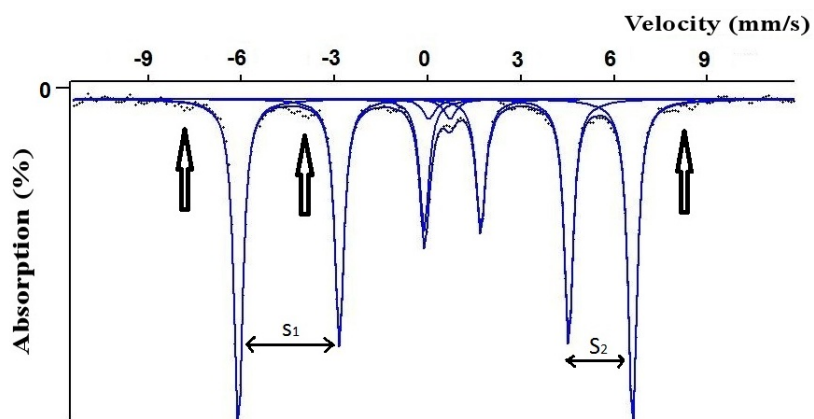
Figure 8.3.: Mössbauer spectra of $SrFeO_2$ at room temperature

Site	IS δ (mm s^{-1})	Δ(mm s^{-1})	ε(mm s^{-1})	B_{hf}(T)	%
1	0.49	1.2	-0.303	39.2	97
2	0.34	0.681	-	-	3

Table 8.1.: Mössbauer parameters of $SrFeO_2$ at room temperature. δ is the isomer shift, Δ is the quadrupole splitting, ε is the quadrupole interaction in the magnetically ordered phase , B_{hf}(T) is the magnetic hyperfine field.
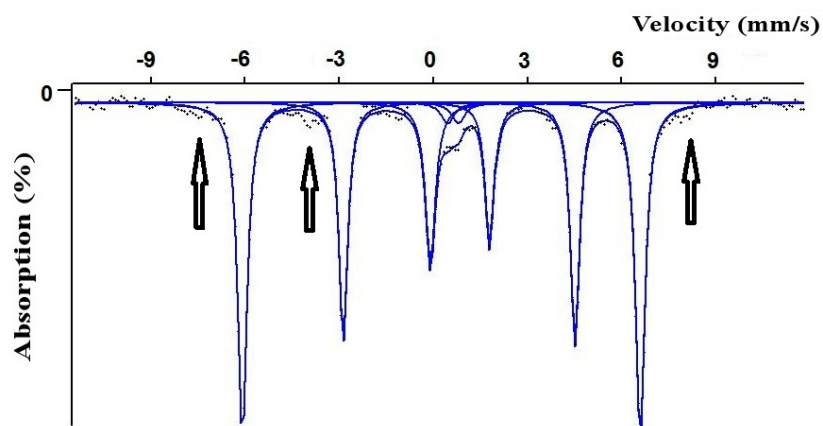
Figure 8.4.: Mössbauer spectra at room temperature of $SrFeO_2$ after heat up to 400K under 10^{-10} bar vacuum

Site	IS δ(mm s^{-1})	Δ(mm s^{-1})	ε(mm s^{-1})	B$_{hf}$(T)	%
1	0.497	-	-0.28	39	96
2	0.5	0.3	-	-	4

Table 8.2.: Mössbauer parameters at room temperature of SrFeO$_2$ after heat up to 400K under 10^{-10} bar vacuum. δ is the isomer shift, Δ is the quadrupole splitting, ε is the quadrupole interaction in the magnetically ordered phase , B$_{hf}$(T) is the magnetic hyperfine field.
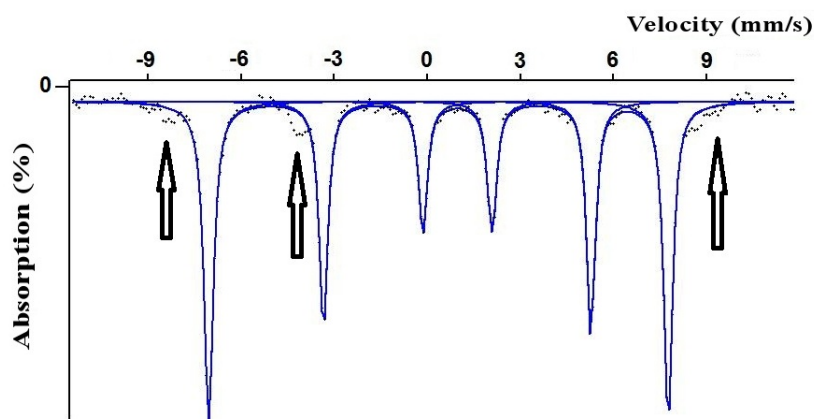

Figure 8.5.: Mössbauer spectra at 4.2K of SrFeO$_2$ after heat up to 400K under 10^{-10} bar vacuum

Site	IS δ (mm s^{-1})	ε(mm s^{-1})	B$_{hf}$(T)
1	0.619	-0.304	46

Table 8.3.: Mössbauer parameters at 4.2K of SrFeO$_2$ after heat up to 400K under 10^{-10} bar vacuum. δ is the isomer shift, ε is the quadrupole interaction in the magnetically ordered phase , B$_{hf}$(T) is the magnetic hyperfine field.

8.4. X-ray absorption study of SrFeO$_2$

The physical properties of SrFeO$_2$ are very interesting. The Néel transition temperature is 473K , which is surprisingly high for a layered, two-dimensional material. This is explained by inelastic neutron-scattering as the out-of-plane direct Fe-Fe exchange is comparable in strength to the in-plane Fe-O-Fe superexchange [95]. Yet, the electronic structure of SrFeO$_2$ is still not clear. According to the crystal field theory, the high spin state of Fe^{2+} with D$_{4h}$ point symmetry should have a ground state of $(d_{xz}, d_{yz})^3$ [19]. However, the DFT calculations suggested that down-spin Fe $3d$ electrons occupy the nondegenerate d_z^2 level, which explains the absence of Jahn-Teller instability [7, 96]. Moreover, the experimental observation of the electronic structure by x-ray absorption and photonemission spectroscopy on thin film and bulk powder sample have got different spectra[97, 98]. On the thin film SrFeO$_2$ sample[97], the O K-edge XAS spectra at around 529-532eV have three peaks, shown in Fig 8.7a, corresponding to the unoccupied O $2p$ states hybridized with Fe $3d$. And they are assigned to Fe $3d_{xy}$, $3d_{xz}+3d_{yz}$, and $3d_{x^2-y^2}$ from lower to higher photon-energies. For the bulk sample[98], shown in Fig 8.7b, the oxygen K-edge
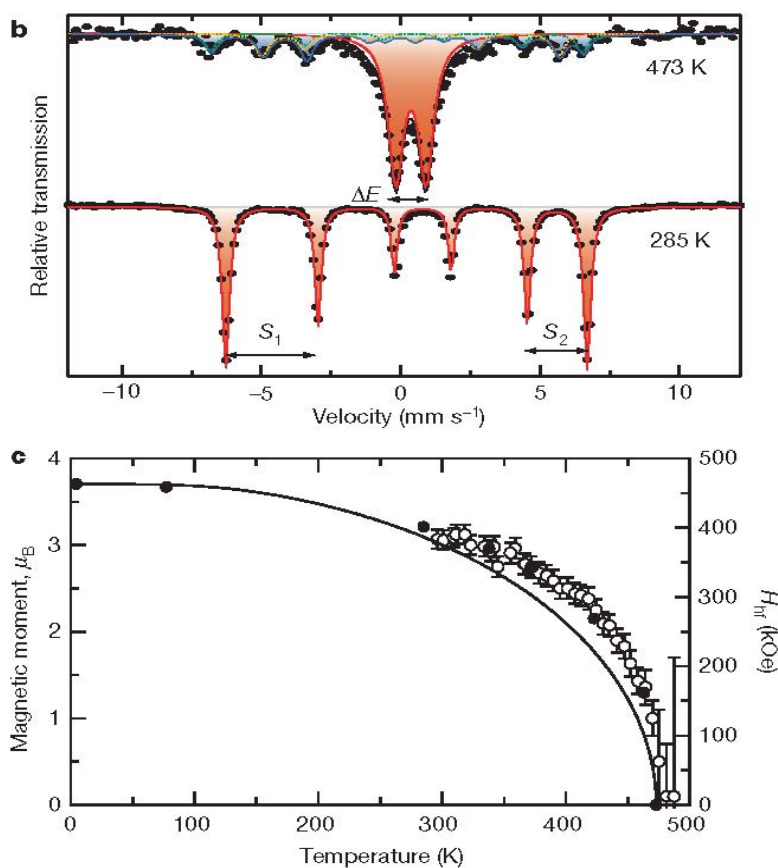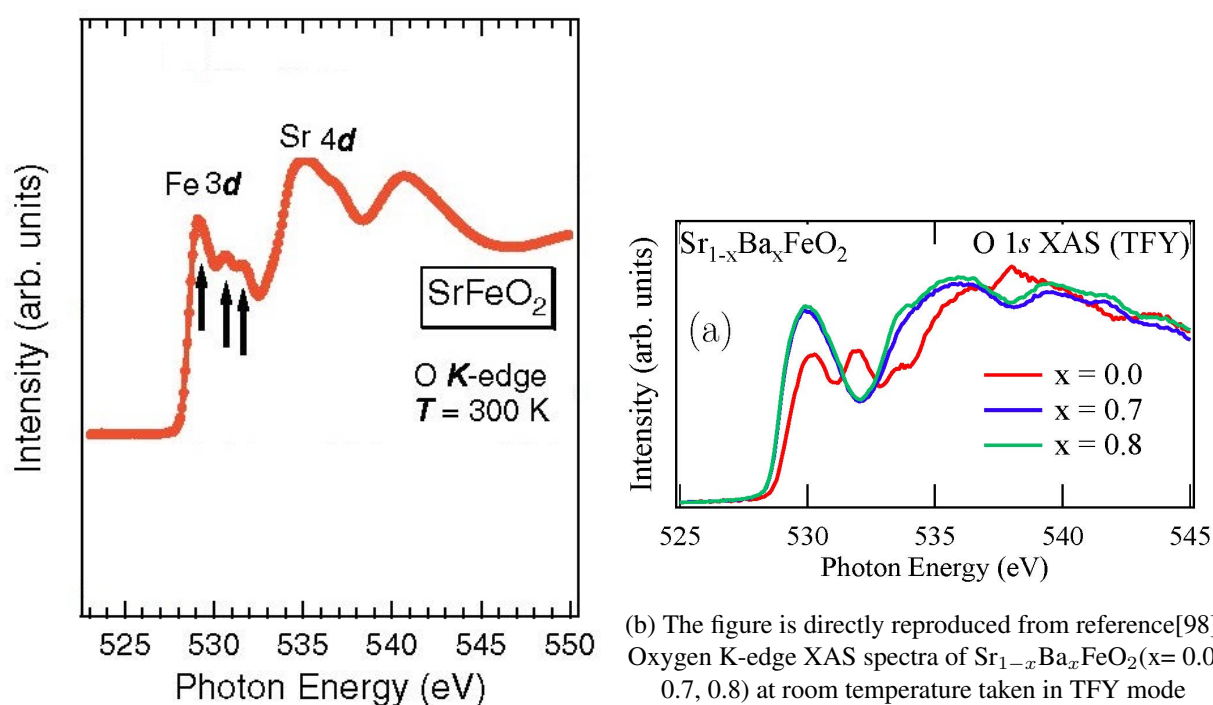
Figure 8.6.: The figure are directly copied from Ref.[19] b. Mössbauer spectra of SrFeO$_2$ at 285K and 473K. The red lines indicate the spectra from SrFeO$_2$, while the blue line at 473K represents the spectrum from a small amount of SrFeO$_{2.5}$. The black line is the total fit. c. Temperature dependence of the magnetic moment and the hyperfine field H$_{hf}$ determined by NPD (open circles) and Mössbauer spectroscopy (solid circles), respectively. The solid curve is the theoretical Brillouin function for S=2. Error bars are s.d. determined by the Rietveld refinement.[19]

XAS spectra of SrFeO$_2$ looks very different from the thin film sample but similar to Fe$_2$O$_3$. The reason is still not clear.

In order to explain the electronic structure of SrFeO$_2$, we have performed x-ray absorption spectroscopy. The Fe $L_{2,3}$ x-ray absorption spectra and its temperature dependent spectra of Fe$L_{2,3}$ edge are shown in Fig 8.8. The whole spectra split into two peaks , namely L_3 in the energy range of 706-714 eV and L_2 in the energy range of 720-726 eV , respectively. This is caused by the spin-orbit coupling of the Fe $2p$ core hole and the two features are related to the $2p_{3/2}$ and $2p_{1/2}$ core holes in the final state. It is well known that for the transition metal oxides, an increase of the valence of the metal ion leads to a shift of the transition metal ions $L_{2,3}$ XAS spectra to higher energies by 1 eV or more [30, 94]. The determination of the valence of a transition metal ion in a compound can be done by comparison with the spectra of a reference compound with well-defined valence. We can see that before changing the temperature, the spectra look quite similar to Fe$_2$O$_3$, indicating the valence of iron is Fe^{3+} instead of Fe^{2+}. This result is in terms with the previous reported bulk sample Fe$L_{2,3}$ edge XAS[98] but in

(b) The figure is directly reproduced from reference[98]. Oxygen K-edge XAS spectra of Sr$_{1-x}$Ba$_x$FeO$_2$(x= 0.0, 0.7, 0.8) at room temperature taken in TFY mode

(a) The figure is directly reproduced from reference[97]. Oxygen K-edge XAS spectra of SrFeO$_2$ thin film at room temperature. Arrows in each spectrum indicate the peak positions in the Fe 3d-derived unoccupied states hybridized with 2p states.

Figure 8.7.: Comparison of literature reported oxygen K-edge XAS measurement on thin film and bulk sample

contrast with the reported bond valence sum calculation of the synchrotron data[19]. When the temperature goes down to 200K , the spectrum doesn't change much. However, when the temperature increases to 400K, the spectrum changes abruptly and the peak, which corresponds to Fe^{2+}, appears as indicated by the arrows in the Figure 8.8. When the temperature cools down again to 300K, the intensities of Fe^{2+} slightly increase but almost keep the same as the spectrum at 400K. It is reported [6] that the compound is stable at 400K and the structure of Fe^{2+} in square planar coordination even exist until 960K, the change of our experimental spectra at 400K is a bit surprising. Owing to the synthetic route of the SrFeO$_2$, the very low sintering temperature makes it impossible to get a strong pellet. Moreover, the washing procedure after the reaction to remove the byproduct may destroy the surface of the grains of the compound. As the XAS techniques are surface sensitive, we suspect the grain boundary may attribute to the change of the XAS spectra of SrFeO$_2$ versus temperature.

In order to verify our suspicion and to get the XAS spectra coming from the real nature of the compound SrFeO$_2$, we have made several improvements of our synthetic route. First of all, to avoid the washing process damaging the surface of the grain, we have skipped this process and measured the pellet contain the byproduct CaO. It is possible to do so because the calcium have different energy range of Fe $L_{2,3}$ edge, and therefore it will not influence the spectrum of iron. Secondly, the harder the pellet is, the smaller the grain boundary it has. We have tried to
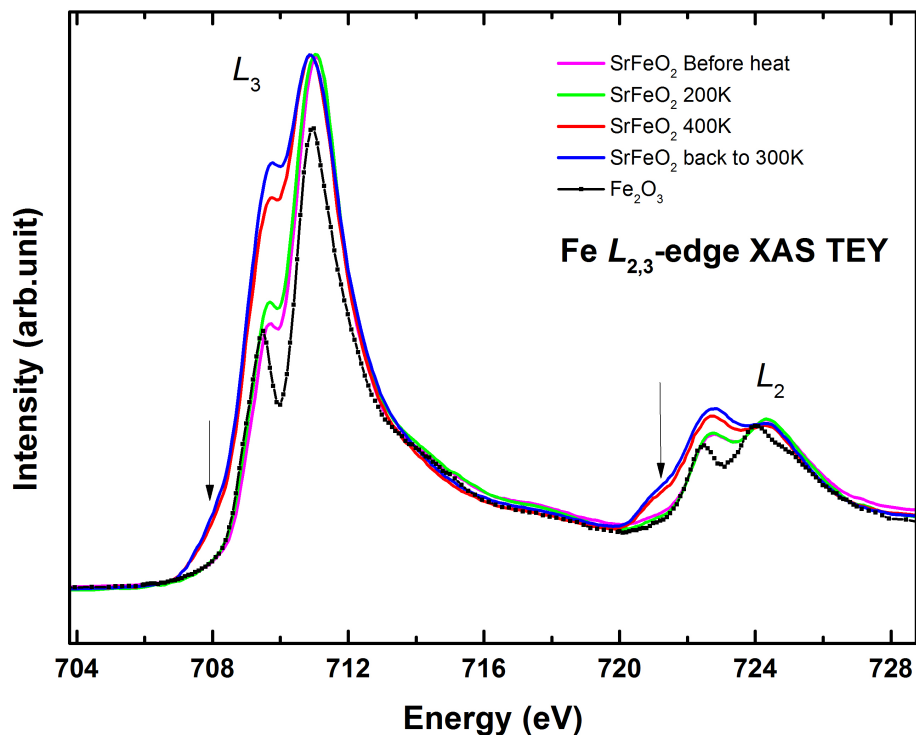
Figure 8.8.: Temperature dependence of Fe L$_{2,3}$ edge XAS spectra of SrFeO$_2$

re-sinter the pellet of SrFeO$_2$ together with CaH$_2$ in a sealed vacuum quartz tube. SrFeO$_2$ has decomposed at the temperature even lower than the reaction temperature. Hence, we pelletize the mixture of the reactant (SrFeO$_{3-x}$ and CaH$_2$) under 1.6Gpa before the chemical reaction and use the as-synthesized pellet which being kept in the highest temperature-reduction temperature. Both ways are aiming to get stronger pellets. Thirdly, we have changed the ratio of the SrFeO$_{3-x}$ and CaH$_2$ (molar ratio is 3:4) so that there is no excess CaH$_2$ left after the reduction. Last but not least, given the fact that the Fe^{2+} may not be really stable under air, we have manipulated the whole process in the argon glove box and the sample is also kept in vacuum arms and transferred into the XAS chamber without exposing into air. Finally we get the spectra listed in Fig 8.9 and Fig 8.10.

We compare our spectra with the literature reported spectra of the bulk sample, marked as SrFeO$_2$ Fujimori's group in red line in the figures. If we measure the sample prepared in the same way as reported [19], the spectra (marked as SrFeO$_2$ washed in black line) look very similar to the reported spectra of the bulk sample, and both are almost overlapping with Fe$_2$O$_3$. But if we measure the sample using our revised procedure (marked as SrFeO$_2$ without washing in blue line), we can see clearly the change of the spectra. For Fe L$_{2,3}$ edge XAS spectra, the main peak of L$_3$ edge moves to lower energy in our spectra(black straight line is for guiding the eyes) and in the meantime new peaks appear in the spectra, indicating by arrows. This

indicates the Fe^{2+} component increasing in the spectra. For the oxygen K-edge XAS spectra, the first peak (529-534 eV), arising from partially empty $2p$ shells of oxygen hybridized with Fe$3d$ shell, change a lot between the so called "SrFeO$_2$ washed" and "SrFeO$_2$ without washing". The small hump at 530.45eV is due to small amount of Fe^{3+} existing in the compound, which has stronger hybridization with oxygen than Fe^{2+}. But the intensity is much smaller than the "SrFeO$_2$ washed" sample. This can be more clearly proved by the steep slope of the sharp peak at 532.95eV (main feature of CaO oxygen K-edge). If the spectrum is just the overlapping between the spectrum of SrFeO$_2$ washed and the spectrum of CaO , there will be a hump on the shoulder of CaO main peak (around 532eV). The oxygen K-edge with total fluorescence yield mode can probe around 100nm deep into the bulk, which is less surface sensitive than the total electron yield. We would expect that the spectra we get from the revised synthetic procedure are more close to the real bulk properties of SrFeO$_2$, and the grain boundary and washing procedure have added the difficulties for probing the real electronic properties of SrFeO$_2$.
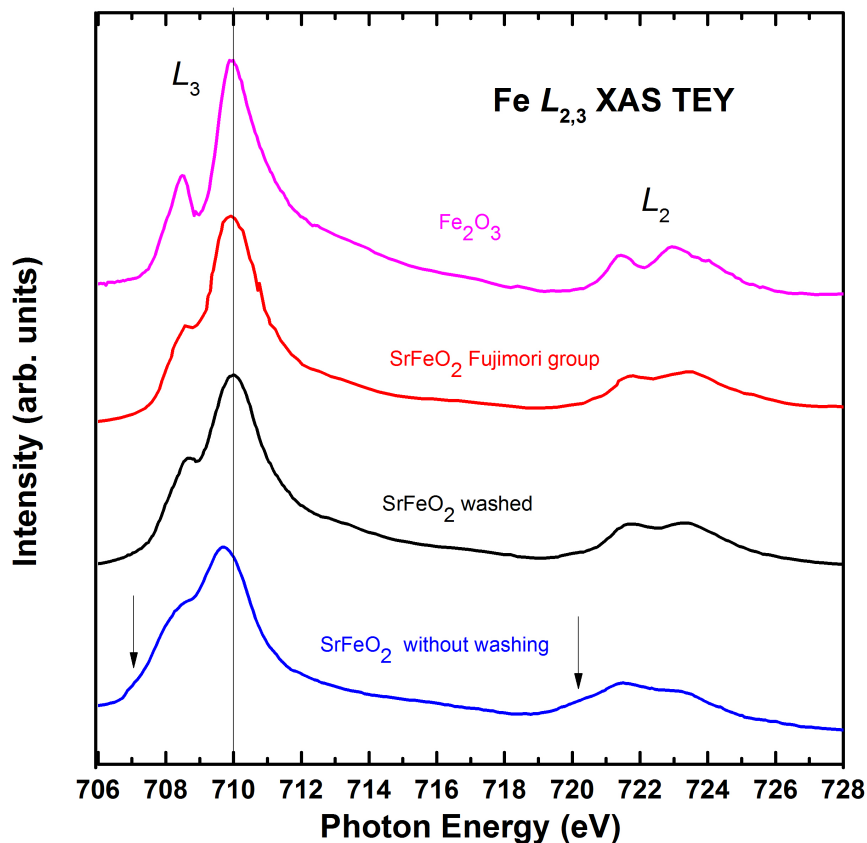

Figure 8.9.: Fe L$_{2,3}$ edge XAS spectra of SrFeO$_2$ from different resources (the detail can be found in the text). black straight line is for guiding the eyes. The arrows represent the peak of Fe^{2+}
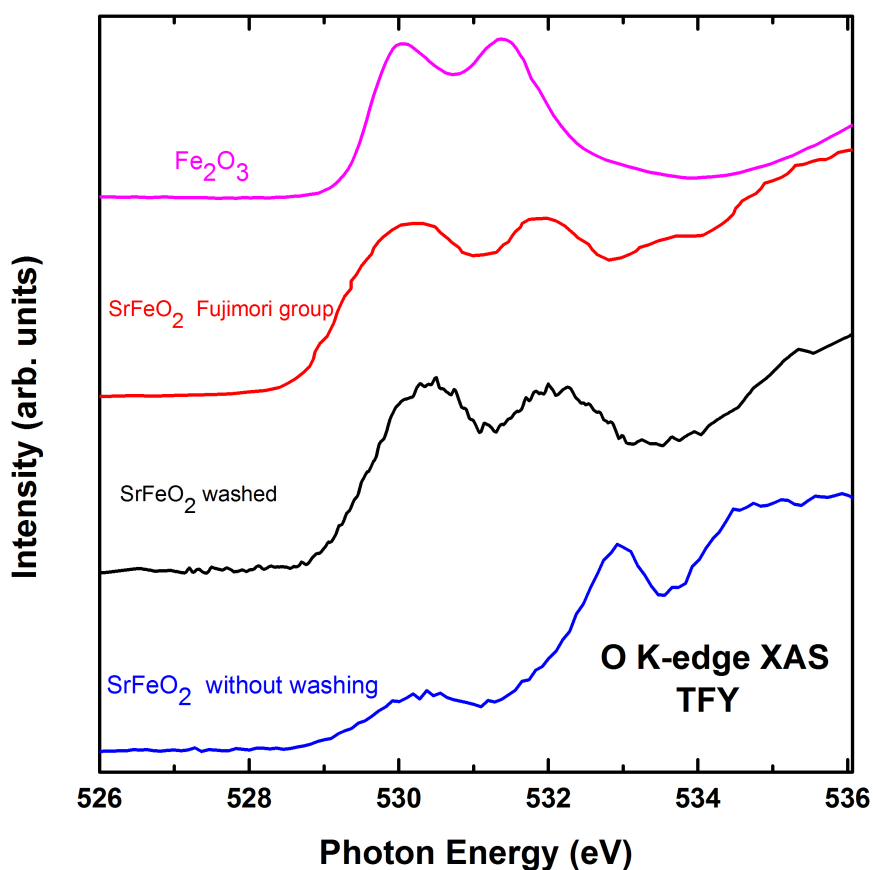
Figure 8.10.: Oxygen K-edge XAS spectra of SrFeO$_2$ from different resources (the detail can be found in the text)

8.5. Conclusion

By removing the apical oxygens from the octahedral sites of Sr$_4$Fe$_4$O$_{11}$ we tune the valence of the iron into 2+ in SrFeO$_2$. SrFeO$_2$ powder samples are prepared with Fe^{2+} in square planar coordination. X-ray diffraction have confirmed the structure and Mössbauer spectra show the sample have 3% impurity. Due to the preparation process can only be done at low temperature, the mechanical strong pellet is extremely difficult to obtain. This hinders the x-ray absorption spectroscopy to investigate the electronic structure of this compound, as the total electron yield mode used for the Fe-$L_{2,3}$ edge is partially surface sensitive. By improving the synthetic route to reduce the grain boundary inside the compound, we obtain the XAS spectra with higher Fe^{2+} content than reported in the literature[98]. The Fe^{3+} content in XAS spectra are likely caused by the washing process during the synthesis.

Chapter 9.

Summary

The relationship between crystallographic, magnetic, and electronic structures have long been of high interest in academic research. Strontium iron oxides have structural, charge, spin, and orbital degrees of freedom, and thus give a lot of complementary information to correlate for the condensed matter scientists. In this thesis, we have carefully prepared various strontium iron oxides as pure phases, especially with a well defined distribution of oxygen vacancies. Their crystallographic structure is characterized, as well as their magnetic and electronic properties. The analysis are mainly based on X-ray diffraction, Mössbauer spectroscopy, and X-ray absorption spectroscopy (XAS) experiments.

Aiming to study the influence of the coordination of Fe cations to the electronic structure, two compounds $Sr_3Fe_2O_6$ and $Sr_2Fe_2O_5$ have been synthesized, both containing pure Fe^{3+}. They are described separately in Chapter 3 and 4. Different synthetic routes have been used in order to obtain the pure $Sr_3Fe_2O_6$ sample. Neutron diffraction for the crystallographic structure analysis gives the precise bond distances of Fe-O in pure pyramidal sites. The magnetic structure refinements show the magnetic moment on the iron site is $3.5\mu_B$ at 10K and they are antiferromagnetically ordered along ab plane. By comparing our data with the previous Mössbauer spectra result, we have further confirmed the purity of our sample. The electronic structure of $Sr_3Fe_2O_6$ has been studied by X-ray absorption spectroscopy. Our experimental spectra of Fe-$L_{2,3}$ is well reproduced by the cluster calculation with a charge-transfer energy Δ=2.5eV, instead of a negative charge transfer energy. With further support from oxygen K-edge XAS spectra, the crystal field splitting energy diagram of this Fe^{3+} in pure pyramidal site is obtained.

Good quality single crystals of $Sr_2Fe_2O_5$ have been prepared and characterized by x-ray diffraction and Mössbauer spectroscopy. Well resolved X-ray absorption spectra have been taken on Fe $L_{2,3}$ edge and oxygen K-edge. Full-multiplet cluster calculations have illustrated the different coordinations of the Fe^{3+} contribution to the spectra.

For the mixed valence compound $Sr_4Fe_4O_{11}$, both powder and single crystals have been synthesized (Chapter 5). The oxygen stoichiometry has been determined by titration. Detailed Rietveld analysis on two batches of powder samples with tiny difference in oxygen content exhibit the high sensitivity of the crystallographic structure to the oxygen stoichiometry. Detailed temperature-dependent neutron powder diffraction data have been presented, leading to the precise determination of bond-lengths and angles of Fe-O in the two crystallographic sites. The bond valence sum calculations based on these single crystal neutron diffraction data clearly show that the Fe^{4+} is in the pyramidal site and Fe^{3+} is in the octahedral site. Temperature-dependent synchrotron X-ray diffraction measurements on the powder samples reveal a new transition around 50 K where a negative thermal expansion arises.

From the Seebeck coefficient, resistivity, and magnetization measurements, we stress the extreme sensitivity of the physical properties to the oxygen stoichiometry in $SrFeO_{3-x}$ by comparing the results obtained on the two batches of samples with different oxygen stoichiometry. Referring the previous work, we conclude that the sample that has been prepared in this thesis is closer to the ideal $Sr_4Fe_4O_{11}$ phase than any of the previously reported samples. A new magnetic transition has been evidenced in our sample in μSR measurements (in line with the recent published neutron measurements [72]) around 90 K. Based on the detailed analysis of μSR and Mössbauer results, one possible explanation for this transition may be found in the spin-lattice coupled dynamics (Chapter 6).

The electronic structure of $Sr_4Fe_4O_{11}$ has been investigated using X-ray absorption and photoelectron spectroscopies. In comparison with the reference samples ($Sr_3Fe_2O_6$ for Fe^{3+} in pyramidal coordination, $SrFeO_3$ for Fe^{4+} in octahedra coordination, $LaFeO_3$ for Fe^{3+} in octahedral coordination), the Fe-$L_{2,3}$ edge and O K-edge spectra confirm the good stoichiometry in our $Sr_4Fe_4O_{11}$ sample. Photoelectron spectra show the compound is a semiconductor. Resonant photoelectron spectroscopy unravels the contributions of Fe^{3+} and Fe^{4+} to the valence band of the single crystal $Sr_4Fe_4O_{11}$ close to the Fermi energy (Chapter 7). A linear dichroism X-ray absorption spectroscopy of the Fe-$L_{2,3}$ edge on the single crystal of $Sr_4Fe_4O_{11}$ are planned in the future, probably the site symmetry of Fe^{3+} and Fe^{4+} could be distinguished in such experiment and the charge ordering in $Sr_4Fe_4O_{11}$ phase might be solved.

By removing the apical oxygens from the octahedral sites of $Sr_4Fe_4O_{11}$ we are able to tune the valence state of the iron into 2+ in $SrFeO_2$ with iron in square planar coordination. $SrFeO_2$ powder samples are prepared. X-ray diffraction have confirmed the correct crystallographic structure and Mössbauer spectra show 97% of the sample is magnetically ordered at room temperature and 3% impurity are non magnetic ordered. Due to the preparation process can only be performed at low temperature, a mechanically strong pellet is extremely difficult to obtain. This hinders the x-ray absorption spectroscopy to investigate the electronic structure of this compound, as the total electron yield mode used for the Fe-$L_{2,3}$ edge is partially surface sensitive. By improving the synthetic route to reduce the grain boundary inside the compound, we are able to obtain the XAS spectra with higher Fe^{2+} content than reported in the literature[98]. The Fe^{3+} content in XAS spectra are likely caused by the washing process during the synthesis.
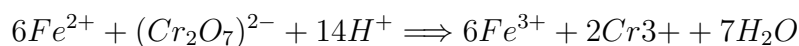
Appendix A.

Titration

In acid solution, the Fe^{2+} ions (in excess) react with Fe^{4+} ions from the sample according to

$$Fe^{2+} + Fe^{4+} \Longrightarrow 2Fe^{3+}$$
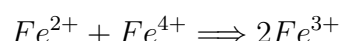
The remaining Fe^{2+} in the solution is titrated by 0.1N $K_2Cr_2O_7$ following the reaction

$$6Fe^{2+} + (Cr_2O_7)^{2-} + 14H^+ \Longrightarrow 6Fe^{3+} + 2Cr3++7H_2O$$

The operation procedures are manipulated as following:

1. Accurately weight iron powder 5.585g (0.1mol) and dissolve in 0.1L concentrated HCl(C=12mol/L).
2. Accurately weight three equal amounts of finely powdered sample ($\sim$100mg each), directly after the reaction , and put them separately into beaker flasks.
3. Add 10ml $FeCl_2$ solution into the beaker flasks.
4. Add 15ml HCl solution with concentration HCl(37%):H_2O = 1:2 in volume portion.
5. Heat (if necessary) the solution over a sand-bath to well dissolve the sample powder (it's better to control the temperature and the time at their lowest possible values)
6. Add 50ml H_2O, then cool the solution in flowing water to room temperature.
7. Add 5ml of 85% H_3PO_4 (to eliminate the yellow color due to the presence of Fe^{3+} , which will otherwise interfere with the observation of the final point);
8. Add 5$\sim$6 drops of the indicator (0.2% or 2g.l^{-1} solution of barium diphenylamine sulfonate);
9. Titrate the solution with 0.1N $K_2Cr_2O_7$ until to the final point as indicated by the sudden occurrence of light violet color;
10. Do a blank test (without the sample powder) under the exactly same conditions.
11. Repeat the procedures 3$\sim$10 for the other aliquots of the sample.

Bibliography

[1] Adler, P. et al. *Collapse of the charge disproportionation and covalency-driven insulator-metal transition in* $Sr_3Fe_2O_7$ *under pressure*. Phys. Rev. B **60**, 4609–4617 (1999).

[2] Lebon, A. et al. Phys. Rev. Lett. **92**, 037202 (2004).

[3] Adler, P. Journal of Solid State Chemistry **130**, 129 – 139 (1997).

[4] Tsujimoto, Y. et al. *Infinite-layer iron oxide with a square-planar coordination*. Nature **450**, 1062–1065 (2007).

[5] Fujimori, A., Saeki, M., Kimizuka, N., Taniguchi, M. and Suga, S. *Photoemission satellites and electronic structure of* Fe_2O_3. Phys. Rev. B **34**, 7318–7328 (1986).

[6] Tassel, C. et al. *Stability of the Infinite Layer Structure with Iron Square Planar Coordination*. Journal of the American Chemical Society **130**, 3764–3765 (2008).

[7] Xiang, H. J., Wei, S.-H. and Whangbo, M.-H. *Origin of the Structural and Magnetic Anomalies of the Layered Compound* $SrFeO_2$: *A Density Functional Investigation*. Phys. Rev. Lett. **100**, 167207 (2008).

[8] Dagotto, E. Science **309**, 257–262 (2005).

[9] Woodward, P. M., Cox, D. E., Moshopoulou, E., Sleight, A. W. and Morimoto, S. *Structural studies of charge disproportionation and magnetic order in* $CaFeO_3$. Phys. Rev. B **62**, 844–855 (2000).

[10] Morimoto, S., Yamanaka, T. and Tanaka, M. Physica B: Condensed Matter 66 – 67 (1997).

[11] Takano, M. et al. *Dependence of the structure and electronic state of SrFeOx on composition and temperature*. Journal of Solid State Chemistry **73**, 140 – 150 (1988).

[12] Demazeau, G. et al. Rev. Chim. Miner. **20**, 155 (1983).

[13] Hodges, J. et al. Journal of Solid State Chemistry **151**, 190 – 209 (2000).

[14] Schmidt, M., Hofmann, M. and Campbell, S. J. *Magnetic structure of strontium ferrite Sr 4 Fe 4 O 11*. Journal of Physics: Condensed Matter **15**, 8691 (2003).

[15] Adler, P. et al. Phys. Rev. B **73**, 094451 (2006).

[16] Vidya, R., Ravindran, P., Fjellvåg, H. and Kjekshus, A. *Spin- and charge-ordering in oxygen-vacancy-ordered mixed-valence* $Sr_4Fe_4O_{11}$. Phys. Rev. B **74**, 054422 (2006).

[17] Adler, P. Phys. Rev. B **77**, 136401 (2008).

[18] Ravindran, P., Vidya, R., Fjellvåg, H. and Kjekshus, A. Phys. Rev. B **77**, 136402 (2008).

[19] Tsujimoto, Y. et al. Nature **450**, 1062–1065 (2007).

[20] Tassel, C. and Kageyama, H. *Square planar coordinate iron oxides*. Chem. Soc. Rev. **41**, 2025–2035 (2012).

[21] Chikamatsu, A. et al. Journal of Electron Spectroscopy and Related Phenomena **184**, 547 – 550 (2012).

[22] Galakhov, V. R. et al. The Journal of Physical Chemistry C **114**, 5154–5159 (2010).

[23] Haruta, M. et al. Journal of Applied Physics **110**, 033708 (2011).

[24] Reehuis, M. et al. Phys. Rev. B **85**, 184109 (2012).

[25] Richard Tilley. *Crystals and crystal structures* (John Wiley and Sons Ltd , West Sussex, England, 2006).

[26] R.E. Dinnebier and S.J.L.Billinge. *Powder Diffraction Theory and Practice* (RSC Publishing, Cambridge, UK, 2008).

[27] Rodriguez-Carvajal, J. *Fullprof suite* (2010).

[28] Haverkort, M. Ph.D. thesis, University of Cologne (2005).

[29] Tjeng, L. H. personal communication (2010).

[30] Burnus, T. et al. *X-ray absorption and x-ray magnetic dichroism study on Ca_3CoRhO_6 and Ca_3FeRhO_6*. Phys. Rev. B **77**, 205111 (2008).

[31] Park, J.-H. Ph.D. thesis, University of Michigan (1994).

[32] Stefan Huefner. *Photoelectron spectroscopy* (Spring-Verlag Berlin Heidelberg New York, 1995).

[33] Gabriel, K. and Vollhardt, D. *Stongly Correlated Materials: Insights from dynamical meanfield theory*. Physics Today **57**, 53–59 (2004).

[34] Zaanen, J., Sawatzky, G. A. and Allen, J. W. *Band gaps and electronic structure of transition-metal compounds*. Phys. Rev. Lett. **55**, 418–421 (1985).

[35] Koethe, T. C. Ph.D. thesis, University of Cologne (2007).

[36] Frank de Groot and Akio Kotani. *Core Level Spectroscopy of Solids* (Taylor and Francis Group, Boca Raton, London, New York, 2008).

[37] Dominic P.E.Dickson, Frank J.Berry. *Moessbauer spectroscopy* (Cambridge University Press, Cambridge, New York, Melbourne, 1986).

[38] Pascua, G. and Luetkens, H. personal communication (2012).

[39] Luetkens, H. Introduction to muon spin rotation and relaxation (Presented in the summer school in Magnetic Phenomena, Zuoz, Switzerland, 2010).

[40] de Réotier, P. D. and Yaouanc, A. *Muon spin rotation and relaxation in magnetic materials*. Journal of Physics: Condensed Matter **9**, 9113 (1997).

[41] Adler, P., Goncharov, A. and Syassen, K. *Strontium ferrates(IV): transition metal oxides at the insulator-metal borderline*. Hyperfine Interactions **95**, 71–84 (1995).

[42] Ruddlesden, S. N. and Popper, P. *New compounds of the K_2NIF_4 type*. Acta Crystallographica **10**, 538–539 (1957).

[43] Komarek, A. C. et al. *Magnetoelastic coupling in $R\mathrm{TiO_3}$ ($R = \mathrm{La, Nd, Sm, Gd, Y}$) investigated with diffraction techniques and thermal expansion measurements*. Phys. Rev. B **75**, 224402 (2007).

[44] Schmidt, M., Hofmann, M. and Campbell, S. J. Journal of Physics:Condensed Matter **15**, 8691 (2003).

[45] Koehler, W. and Wollan, E. Journal of Physics and Chemistry of Solids **2**, 100–106 (1957).

[46] Valldor, M., Raphaël, P. H., Wuttke, J., Zamponi, M. and Schweika, W.

[47] V.M. Zainullina, V. K., M.A. Korotin. Eur. Phys. J. B **49**, 425 (2006).

[48] Kuiper, P., Searle, B. G., Rudolf, P., Tjeng, L. H. and Chen, C. T. Phys. Rev. Lett. **70**, 1549–1552 (1993).

[49] Dann, S., Weller, M. and Currie, D. Journal of Solid State Chemistry **97**, 179 – 185 (1992).

[50] Maljuk, A. et al. Journal of Crystal Growth **273**, 207 – 212 (2004).

[51] Zeng, Z., Greenblatt, M., IV, J. S., Croft, M. and Khalid, S. Journal of Solid State Chemistry **147**, 185 – 198 (1999).

[52] Mori, K. et al. Journal of Physics and Chemistry of Solids **60**, 1443–1446 (1999).

[53] Mori, K. et al. Applied Physics A: Materials Science and Processing **74**, s914–s916 (2002).

[54] MacChesney, J., Williams, H., Sherwood, R. and Potter, J. Materials Research Bulletin **1**, 113 – 122 (1966).

[55] Gallagher, P. K., MacChesney, J. B. and Buchanan, D. N. E. The Journal of Chemical Physics **45**, 2466–2471 (1966).

[56] Dann, S. E., Weller, M. T., Currie, D. B., Thomas, M. F. and Al-Rawwas, A. D. *Structure and magnetic properties of Sr2FeO4 and Sr3Fe2O7 studied by powder neutron diffraction and Mossbauer spectroscopy*. J. Mater. Chem. **3**, 1231–1237 (1993).

[57] Mitra, C. et al. *Direct observation of electron doping in $\mathrm{La_{0.7}Ce_{0.3}MnO_3}$ using x-ray absorption spectroscopy*. Phys. Rev. B **67**, 092404 (2003).

[58] Chang, C. F. et al. *Spin Blockade, Orbital Occupation, and Charge Ordering in* $La_{1.5}Sr_{0.5}CoO_4$. Phys. Rev. Lett. **102**, 116401 (2009).

[59] Hollmann, N. et al. *Orbital occupation and magnetism of tetrahedrally coordinated iron in CaBaFe$_4$O$_7$*. Phys. Rev. B **83**, 180405 (2011).

[60] de Groot, F. *X-ray absorption and dichroism of transition metals and their compounds.* Journal of Electron Spectroscopy and Related Phenomena **67**, 529 – 622 (1994).

[61] Tanaka, A. and Jo, T. *Resonant 3d, 3p and 3s Photoemission in Transition Metal Oxides Predicted at 2p Threshold.* Journal of the Physical Society of Japan **63**, 2788–2807 (1994).

[62] Hu, Z. et al. *Different Look at the Spin State of* Co^{3+} *Ions in a* CoO_5 *Pyramidal Coordination.* Phys. Rev. Lett. **92**, 207402 (2004).

[63] P.K.Gallagher, J.B.MacChesney and D.N.E.Buchananr. The Journal Of Chemical Physics **41**, 2429–2433 (1964).

[64] BERTHIER, T. Ph.D. thesis, University of Rennes 1 and University degli studi di Torino (2007).

[65] C.Greaves, A.J.Jacobson, B.C.Tofield and Fender, B. Acta Crystallogr. B **31**, 641 (1975).

[66] Grenier, J.-C., EA, N., Pouchard, M. and Hagenmuller, P. Journal of Solid State Chemistry **58**, 243–252 (1985).

[67] Galakhov, V. R. et al. *Valence Band Structure and X-ray Spectra of Oxygen-Deficient Ferrites SrFeOx.* The Journal of Physical Chemistry C **114**, 5154–5159 (2010).

[68] W. A. Harrison. *Electronic Structure and the Properties of Solids* (Dover, New York, 1989).

[69] Anthony R. West. *Solid State Chemistry and its Applications* (John Wiley and Sons Ltd., 1990).

[70] M.Schmidt. Journal of Physics and Chemistry of Solids **61**, 1363–1365 (2000).

[71] Williams, G. V. M., Hemery, E. K. and McCann, D. *Magnetic and transport properties of SrFeO$_x$.* Phys. Rev. B **79**, 024412 (2009).

[72] Reehuis, M. et al. Phys. Rev. B **85**, 184109 (2012).

[73] Rodriguez-Carvajal, J. *Introduction to the program FullProf* (2000).

[74] M.Harder and H.Müller-Buschbaum. Z. Anorg. Allg.Chem. **169**, 464 (1980).

[75] Dann, S., Currie, D., Weller, M., Thomas, M. and Al-Rawwas, A. Journal of Solid State Chemistry **109**, 134 – 144 (1994).

[76] Soubeyroux, J., Courbin, P., Fournes, L., Fruchart, D. and Flem, G. L. Journal of Solid State Chemistry **31**, 313 – 320 (1980).

[77] R.Pradheesh et al. Journal of Applied Physics **111**, 053905 (2012).

[78] Hemery, E. K., Williams, G. V. M. and Trodahl, H. J. Phys. Rev. B **75**, 092403 (2007).

[79] Chaikin, P. M. and Beni, G. *Thermopower in the correlated hopping regime*. Phys. Rev. B **13**, 647–651 (1976).

[80] P. A. Cox. *Transition Metal Oxides* (Great Clarendon Street, Oxford ox2 6DP, 1992).

[81] Ishiwata, S. et al. *Versatile helimagnetic phases under magnetic fields in cubic perovskite* $\mathbf{SrFeO_3}$. Phys. Rev. B **84**, 054427 (2011).

[82] Gibb, T. C. J. Mater. Chem. **4**, 1445–1449 (1994).

[83] Williams, G. V. M., Hemery, E. K. and McCann, D. *Magnetic and transport properties of* $SrFeO_x$. Phys. Rev. B **79**, 024412 (2009).

[84] PIZARRO, T. M. Ph.D. thesis, University of Bordeaux 1 (1983).

[85] Luetkens, H. et al. *Microscopic Evidence of Spin State Order and Spin State Phase Separation in Layered Cobaltites* $RBaCo_2O_{5.5}$ *with* $R =$ Y, Tb, Dy, and Ho. Phys. Rev. Lett. **101**, 017601 (2008).

[86] Deac, I. et al. Physica B: Condensed Matter **406**, 2795 – 2800 (2011).

[87] Dunsiger, S. R. et al. *Muon spin relaxation investigation of the spin dynamics of geometrically frustrated antiferromagnets* $Y_2Mo_2O_7$ *and* $Tb_2Mo_2O_7$. Phys. Rev. B **54**, 9019–9022 (1996).

[88] Tanaka, A. and Jo, T. *Resonant 3d, 3p and 3s Photoemission in Transition Metal Oxides Predicted at 2p Threshold*. Journal of the Physical Society of Japan **63**, 2788–2807 (1994).

[89] Taubitz, C. et al. physica status solidi (RRL) – Rapid Research Letters **4**, 338–339 (2010).

[90] Abbate, M. et al. *X-ray absorption of the negative charge-transfer material* $SrFe_{1-x}Co_xO_3$. Phys. Rev. B **65**, 165120 (2002).

[91] Yeh, J. J. and Lindau, I. At. Data Nucl. Data Tables **32**, 1 (1985).

[92] Scofield, J. H. *Theoretical Photoionization Cross Sections from 1 to 1500keV* (1973).

[93] Bocquet, A. E. et al. *Electronic structure of* $SrFe^{4+}O_3$ *and related Fe perovskite oxides*. Phys. Rev. B **45**, 1561–1570 (1992).

[94] Mitra, C. et al. *Direct observation of electron doping in* $La_{0.7}Ce_{0.3}MnO_3$ *using x-ray absorption spectroscopy*. Phys. Rev. B **67**, 092404 (2003).

[95] Tomiyasu, K. et al. *Magnetic Excitations in Infinite-Layer Antiferromagnetic Insulator*. Journal of the Physical Society of Japan **79**, 034707 (2010).

[96] Pruneda, J. M., Íñiguez, J., Canadell, E., Kageyama, H. and Takano, M. *Structural and electronic properties of SrFeO$_2$ from first principles*. Phys. Rev. B **78**, 115101 (2008).

[97] Chikamatsu, A. et al. *Investigation of electronic states of infinite-layer SrFeO2 epitaxial thin films by X-ray photoemission and absorption spectroscopies*. Journal of Electron Spectroscopy and Related Phenomena **184**, 547 – 550 (2012).

[98] Ishigami, K. Master's thesis, University of Tokyo (2010).

Titre : Synthèse, caractérisation et étude des propriétés magnétiques et de la structure électronique d'oxydes de fer et de strontium

Résumé :

Les diverses perovskites de strontium-fer présentent de très fortes corrélations entre la structure cristalline et les phénomènes d'ordre de lacunes d'oxygènes, de charge, de spin et d'orbitales. Dans cette thèse, nous avons réalisé une étude systématique des relations entre les ordres de charges et les ordres de spins selon les différents environnements cristallographiques rencontrés pour les cations Fe^{3+} et Fe^{4+} dans la phase $Sr_4Fe_4O_{11}$, pour le cation Fe^{3+} dans les phases $Sr_3Fe_2O_6$ et $Sr_2Fe_2O_{10}$ et pour le cation Fe^{2+} dans la phase $SrFeO_2$. Les synthèses des phases polycristallines furent réalisées via des voies « solide » ou « sol-gel » en complément de la synthèse de cristaux préparés à l'aide d'un four à image à fusion de zone verticale pour les phases $Sr_4Fe_4O_{11}$ et $Sr_2Fe_2O_{10}$. La qualité cristalline et chimique des oxydes fut contrôlée par diffraction de rayons X sur poudre et spectroscopie Mössbauer alors que l'étude de la structure électronique de chaque phase a été réalisée à l'aide de spectroscopie d'absorption de rayons X. Finalement, les structures magnétiques des phases $Sr_3Fe_2O_6$ et $Sr_4Fe_4O_{11}$ sont aussi présentées.

Mots clés :

• Structure pérovskite • Spectroscopie d'absorption de rayons X   •Spectroscopie Mössbauer

• Diffraction de Neutrons

Title : **Synthesis, characterization and investigation on the magnetic and electronic structure of strontium iron oxides**

Abstract :

The relationship of the crystallographic, magnetic, and electronic structure have long been of high interest in research. Strontium iron oxides have structural, charge, spin, and orbital degrees of freedom, and thus give rich information to study for the condensed matter scientists. In this thesis, we have systematically studied the strontium iron oxides based on the freedom of the iron charge: Fe^{3+} and Fe^{4+} mixed valence compound $SrFeO_{2,75}$, Fe^{3+} compound $Sr_3Fe_2O_6$ and $SrFeO_{2,5}$ with different coordination around Fe^{3+} and Fe^{2+} compound $SrFeO_2$. The synthesis of the polycrystalline compounds are through either solid state reaction or sol-gel method. Single crystals of $SrFeO_{2,75}$ and $SrFeO_{2,5}$ have been prepared by floating zone furnace. The purity of all the compounds is checked by lab x-ray diffraction and Mössbauer spectroscopy. Electronic structures have been studied by x-ray absorption spectroscopy for all these compounds. Special efforts have been used to investigate the magnetic structure of $SrFeO_{2,75}$ and $Sr_3Fe_2O_6$.

Keywords :

• Perovskite Structure • X-Ray absorption spectroscopy   • Mössbauer Spectroscopy

• Neutron Diffraction